Universidade do Minho
School of Engineering

André Fernandes de Sá Resende

Ergowear: Development of a Smart Garment for Postural Monitoring and Biofeedback

June, 2022

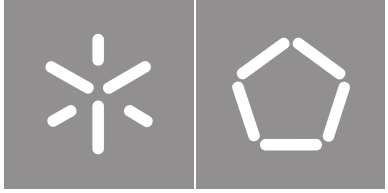

Universidade do Minho
School of Engineering

André Fernandes de Sá Resende

Ergowear: Development of a Smart Garment for Postural Monitoring and Biofeedback

Master Thesis

Master in Medical Electronics

Specialization in Medical Electronics

Work developed under the supervision of:

Professor Doutor Alexandre Manuel Teixeira Barros Ferreira Silva

June, 2022

This document was created with the (pdf/Xe/Lua)LaTeX processor and the NOVAthesis template (v6.9.15) [1].

Acknowledgements

Muito obrigado Professor Alexandre, por todo o tempo disponibilizado, e por toda a orientação e ajuda que me forneceu.

À Professora Cristina, pelo espírito crítico e trabalhador que conseguiu incutir em mim.

À Sara, que teve de me aturar ao longo deste projeto, e apoiar-me nesta jornada! Fez um grande trabalho na minha orientação, e sempre me deu apoio quando mais precisei!

Muito obrigado aos meus pais, por toda a inspiração, disciplina e sabedoria que me conseguiram passar. Sem vocês e o vosso amor, nunca seria capaz de chegar tão longe.

Ao meu irmão, por me aturar e e ser um grande companheiro ao longo de todos este anos. Nunca estarás longe de mim.

À minha avó materna, que sempre me apoiou e cuidou de mim ao longo da minha vida. Estarás sempre comigo, independentemente do que acontecer. Jamais me esquecerei de si.

Aos meus amigos que me acompanharam ao longo desta experiência que foi a minha passagem pela UMinho. Nunca me esquecerei de todos os tempos dedicados ao estudo e todas as noites de lazer que partilharam comigo. Um especial agradecimento ao Rafael, por todo o companheirismo e amizade com que me presentiou ao longo do meu percurso universitário. Ao Benjamim, que desde o secundário esteve sempre comigo, nos melhores e nos piores momentos. Ao Semanas, que já o conheço desde que ele nasceu, sendo para mim família. Ao Carlos, Sol, Chico, Dinis, Helena, Afonso, Paulo, Simão, Alexandre, David, Yasmin, Paralelo e Tiago que criaram laços comigo, que nem o tempo ou a distância irão quebrar.

STATEMENT OF INTEGRITY

I hereby declare having conducted this academic work with integrity. I confirm that I have not used plagiarism or any form of undue use of information or falsification of results along the process leading to its elaboration.

I further declare that I have fully acknowledged the Code of Ethical Conduct of the Universidade do Minho.

_____, _____

(Place) (Date)

_____

(André Fernandes de Sá Resende)

Resumo

Ergowear: Desenvolvimento de um Vestuário Inteligente para Monitorização Postural e Biofeedback

Atualmente, as Lesões Musculoesqueléticas Relacionadas com o Trabalho (LMERT) são consideradas o "problema relacionado com o trabalho mais prevalente"na União Europeia, levando a um custo estimado de cerca de 240 biliões de euros. Em casos mais severos, estes distúrbios podem causar danos vitalícios à saúde do trabalhador, reduzindo a sua qualidade de vida. De facto, LMERTs são consideradas a principal causa da reforma precoce dos trabalhadores. Foi reportado que os segmentos da parte superior do corpo são mais suceptíveis ao desenvolvimento de LMERTs. Para mitigar a prevalência de LMERTs, ergonomistas maioritariamente aplicam métodos de avaliação observacionais, que são altamente dependentes da experiência do analista, e apresentam baixa objetividade e repetibilidade. Desta maneira, esforços têm sido feitos para desenvolver ferramentas de avaliação ergonómica baseadas na instrumentação, para compensar essas limitações. Além disso, com a ascensão do conceito da indústria 5.0, o trabalhador humano volta a ser o foco principal na indústria, juntamente com o robô colaborativo. No entanto, para alcançar uma relação verdadeiramente colaborativa e simbiótica entre o trabalhador e o robô, este último precisa de reconhecer as intenções do trabalhador. Para superar este obstáculo, sistemas de captura de movimento podem ser integrados nesta estrutura, fornecendo dados de movimento ao robô colaborativo.

Esta dissertação visa a melhoria de um sistema de captura de movimento autónomo, da parte superior do corpo, de abordagem inercial que servirá, não apenas para monitorizar a postura do trabalhador, mas também avaliar a ergonomia do usuário e fornecer consciencialização postural ao usuário, por meio de motores de biofeedback. Além disso, o sistema foi já idealizado tendo em mente a sua integração numa estrutura colaborativa humano-robô. Para atingir estes objetivos, foi aplicada uma metodologia de design centrado no utilizador, começando pela análise do Estado da Arte, a avaliação das limitações do sistema anterior, a definição dos requisitos do sistema, o desenvolvimento da peça de vestuário, arquitetura do hardware e arquitetura do software do sistema. Por fim, o sistema foi validado para verificar se estava em conformidade com os requisitos especificados.

O sistema é composto por 9 Unidades de Medição Inercial (UMI), posicionados na parte inferior e superior das costas, cabeça, braços, antebraços e mãos. Também foi integrado um sistema de atuação, para biofeedback postural, composto por 6 motores vibrotáteis, localizados na região lombar e próximo

do pescoço, cotovelos e pulsos. O sistema é alimentado por uma *powerbank* e todos os dados adquiridos são enviados para uma estação de processamento, via WiFi (User Datagram Protocol (UDP)), garantindo autonomia. O sistema tem integrado um filtro de fusão Complementar Extendido e uma sequência de calibração Sensor-para-Segmento estática, de maneira a aumentar a precisão da estimativa dos ângulos das articulações. Além disso, o sistema é capaz de amostrar os dados angulares a 240 Hz, enquanto que o sistema anterior era capaz de amostrar no máximo a 100 Hz, melhorando a resolução da aquisição dos dados.

O sistema foi validado em termos de hardware e usabilidade. Os testes de hardware abordaram a caracterização da autonomia, frequência de amostragem, robustez mecânica e desempenho da comunicação sem fio do sistema, em diversos contextos, e também para verificar se estes estão em conformidade com os requisitos técnicos previamente definidos, que foi o caso. Adicionalmente, as especificações da nova versão do sistema foram comparadas com a anterior, onde se observou uma melhoria direta significativa, como por exemplo, maior frequência de amostragem, menor perda de pacote, menor consumo de corrente, entre outras, e com sistemas comerciais de referência (XSens Link). Testes de usabilidade foram realizados com 9 participantes que realizaram vários movimentos uniarticulares e complexos. Após os testes, os usuários responderam a um questionário baseado na Escala de Usabilidade do Sistema (EUS). O sistema foi bem aceite pelos os usuários, em termos de estética e conforto, em geral, comprovando um elevado nível de vestibilidade.

Palavras-chave: Unidades de Medição Inercial, Sistemas Vestíveis, Monitorização da Postura, Usabilidade do Sistema, Vestibilidade do Sistema, LMERT, *Biofeedback*

Abstract

Ergowear: Development of a Smart Garment for Postural Monitoring and Biofeedback

Nowadays, Work-Related Musculoskeletal Disorders (WRMSDs) are considered the "most prevalent work-related problem" in the European Union (EU), leading to an estimated cost of about 240 billion EUR. In more severe cases, these disorders can cause life-long impairments to the workers' health, reducing their quality of life. In fact, WRMSDs are the main cause for the workers' early retirement. It was reported that the upper body segments of the worker are more susceptible to the development of WRMSDs. To mitigate the prevalence of WRMSD, ergonomists mostly apply observational assessment methods, which are highly dependant on the analyst's expertise, have low objectivity and repeatability. Therefore, efforts have been made to develop instrumented-based ergonomic assessment tools, to compensate for these limitations. Moreover, with the rise of the 5.0 industry concept, the human worker is once again the main focus in the industry, along with the Collaborative Robot (cobot). However, to achieve a truly collaborative relation between the worker and the cobot, the latter needs to know the worker's intentions. To surpass this obstacle, Motion Capture (MoCap) systems can be integrated in this framework, providing motion data to the cobot.

This dissertation aims at the improvement of a stand-alone, upper-body, inertial, MoCap system, that will serve to not only monitor the worker's posture, but also to assess the user's ergonomics and provide posture awareness to the user, through biofeedback motors. Furthermore, it was also designed to integrate a human-robot collaborative framework. To achieve this, a user-centred design methodology was applied, starting with analyzing the State of Art (SOA), assessing the limitations of the previous system, defining the system's requirements, developing the garment, hardware architecture and software architecture of the system. Lastly, the system was validated to ascertain if it is in conformity with the specified requirements.

The developed system is composed of 9 Inertial Measurement Units (IMUs), placed on the lower and upper back, head, upper arms, forearms and hands. An actuation system was also integrated, for postural biofeedback, and it is comprised of 6 vibrotactile motors, located in the lower back, and in close proximity to the neck, elbows and wrists. The system is powered by a powerbank and all of the acquired data is sent to a main station, via WiFi (UDP), granting a standalone characteristic. The system integrates an Extended Complementary Filter (ECF) and a static Sensor-to-Segment (STS) calibration sequence to increase the joint angle estimation accuracy. Furthermore, the system is able to sample the angular data at 240 Hz,

while the previous system was able to sample it at a maximum 100 Hz, improving the resolution of the data acquisition.

The system was validated in terms of hardware and usability. The hardware tests addressed the characterization of the system's autonomy, sampling frequency, mechanical robustness and wireless communication performance in different contexts, and ascertain if they comply with the technical requirements, which was the case. Moreover, the specifications of the new version were compared with the previous one, where a significant direct improvement was observed, such as, higher sampling frequency, lower packet loss, lower current consumption, among others, and with a commercial system of reference (XSens Link). Usability tests were carried out with 9 participants who performed several uni-joint and complex motions. After testing, users answered a questionnaire based on the System Usability Scale (SUS). The system was very well accepted by the participants, regarding aesthetics and overall comfort, proving to have a high level of wearability.

Keywords: Inertial Measurement Units, Wearable Systems, Posture Monitoring, System's Usability, System's Wearability, WRMSD, Biofeedback

Contents

List of Figures

List of Tables

Acronyms

acc accelerometer *(pp. 36–38, 43)*

ANN Artificial Neural Network *(p. 37)*

AP Access Point *(pp. 77, 111)*

ASIC Application-Specific Integrated Circuit *(p. 104)*

BPM Beats per Minute *(p. 46)*

CF Complementary Filter *(pp. xii, 24–26, 28–30, 33, 37, 38, 42)*

cobot Collaborative Robot *(pp. vii, 3, 4)*

DMP Digital Motion Processor *(pp. 33, 37)*

DOF Degree of Freedom *(pp. 13, 14, 27, 31, 32, 36–41)*

ECF Extended Complementary Filter *(pp. vii, xiv, xv, 24, 42, 43, 87, 88, 91, 113, 114)*

EKF Extended Kalman Filter *(pp. 13, 24–26, 28, 29, 33, 36–38, 42, 43)*

EU European Union *(pp. vii, 1)*

EWAS European Assembly Work Sheet *(p. 13)*

FQA Factored Quaternion Algorithm *(pp. 29, 30)*

GDA Gradient-descent Filter *(pp. 24–28, 33, 34, 37, 38, 42, 43, 88)*

gyro gyroscope *(pp. 29, 36–38)*

I2C Inter-Integrated Circuit *(pp. 63–65, 68, 70, 71, 77, 80, 105)*

IMU Inertial Measurement Unit *(pp. vii, xiv, 8, 10, 11, 13, 14, 19–21, 23, 33–38, 40, 42, 54, 63, 77, 82, 84, 85, 87, 89, 92, 93, 95, 96, 105)*

KF Kalman Filter *(pp. 13, 24–29, 33, 36–39, 42, 43)*

LSE Low-Speed External *(p. 84)*

mag magnetometer *(pp. 36–38, 43)*
MIMU Magnetic Inertial Measurement System *(pp. 8, 27, 63, 75, 87)*
MoCap Motion Capture *(pp. vii, xii, 4–6, 8–11, 13, 14, 16, 18, 19, 22, 30, 34, 35, 42, 43, 49, 50, 54, 57, 105, 110, 112, 114)*
MSE Minimum Squared Error *(p. 24)*

NIOSH National Institute for Occupational Safety and Health *(p. 10)*
NNS Nearest Neighbor Search *(p. 37)*
NWU North-West-Up *(p. 91)*

ODR Output Data Rate *(pp. xiii, 84, 85)*

PCB Printed Board Circuit *(pp. xiii, 20, 48, 58, 64, 73, 74, 103, 111, 113)*
PSSUQ Post-Study System Usability Questionnaire *(p. 49)*
PWM Pulse-Width Modulation *(pp. xiii, 69–71)*

QUEST QUaternion ESTimator *(p. 24)*
QUIS Questionnaire for User Interface Satisfaction *(p. 49)*

REBA Rapid Entire Body Assessment *(p. 10)*
RMSE Root-Mean Squared Error *(pp. xv, 13, 30, 31, 33)*
ROM Range of Motion *(pp. 14, 22, 46, 106)*
RPi4 Raspberry Pi 4 *(pp. xv, 47, 48, 71)*
RTC Real-Time Clock *(pp. 79, 80, 84)*
RTT Round-Trip Time *(pp. 97–99)*
RULA Rapid Upper Limb Assessment *(pp. 3, 13, 51)*

SD Standard Deviation *(pp. 31, 32, 38)*
SDI Strap-Down Integration *(pp. xiii, xiv, 48, 77, 80, 82, 83, 93–95, 104, 110, 111)*
SOA State of Art *(pp. vii, 3, 5, 10, 30, 45, 87, 110)*
SPI Serial Peripheral Interface *(pp. 64, 71, 77)*
STS Sensor-to-Segment *(pp. vii, xv, 5, 7, 8, 20–22, 30, 40–42, 110)*

SUMI Software Usability Measurement Inventory *(p. 49)*

SUS System Usability Scale *(pp. viii, 49, 105)*

TRIAD Tri-Axial Attitude Determination *(pp. 24, 26, 27, 36)*

UDP User Datagram Protocol *(pp. vi, vii, 77, 79, 80, 82, 93, 111)*

UKF Unscented Kalman Filter *(pp. 24, 25, 27, 37, 43)*

WHO World Health Organization *(p. 2)*

WRMSD Work-Related Musculoskeletal Disorder *(pp. vii, viii, 1, 2, 4, 110)*

1 Introduction

1.1 Background

1.1.1 Work-Related Musculoskeletal Disorders

Currently, the manufacturing industry plays an important role in the European Union's economy, contributing significantly to its economic growth [2]. Despite that, these industries have a very high physical demand on the workers, leading to the development of WRMSDs.

Musculoskeletal Disorders is a general term that covers all the medical diseases that affect the limbs, spine, and multiple or localised pain syndromes. They are defined has all of the disorders that can cause impairments on the musculoskeletal and connective tissue systems by The Bureau of Labor Statistics of the Department of Labor [3].

WRMSDs are, according the European Risk Observatory, "the most prevalent work-related problem" in the EU[4]. According to several studies made by different institutions [4–6], multiple risk factors were associated with the appearance of these disorders:

- Constrained, fixed or unnatural body poses;
- Repetitive movements;
- Force sustained in critical body areas such as the wrist;
- Routines that do not allow the body to rest;
- Awkward body postures;
- Heavy work loads;
- Lack of recovery time;
- Exposure to low temperatures;
- Prolonged static postures.

WRMSDs affect millions of workers every year, and are acknowledged as a problem with large health and economic impact costs [4, 7]. In 2015, in Finland and France [4], around 79 % and 75 % of the workforce reported WRMSDs, respectively. Due to this problematic, during the last years, a lot more concern is being directed towards this issue, with studies and reports being published by EU-OSHA and the World Health Organization (WHO) [8, 9] bringing attention to it. These disorders account for about 53 % of work-related diseases in the EU-15, and present an economic impact of about 240 billion EUR, or an estimated 2 % of the GDP. Furthermore, they represent about 40-50 % of all the costs associated with occupational health issues [10]. In the UK alone, in 2018, about 30.7 million working days were lost due to these disorders, and 0.5 million WRMSDs cases were reported, resulting in an economical loss of around GBP 5.2 billion, with 3.0 billion borne by the employer [11].

It is important to address that the economic costs cover not only the insurance costs, but also the cost to train new workers, the productivity loss associated with losing experienced workers, and losses in image branding [8, 12]. Moreover, there are other intangible costs that affect the worker, such as increase in financial difficulties, increase in overall stress, emergence of health problems, leading to a reduced quality of life [13].

The anatomical segment more exposed to the prevalence of WRMSDs is the lower back, according to a study performed by EU-OSHA, with agriculture and fishery being the areas with the most self-reported WRMSDs [5, 8, 9]. Following a study performed by the same institution, in Portugal alone, in 2005, around 30.7 % of the workforce reportedly suffered from back disorders [8]. The authors of [14] claimed that disorders on the spine and back are one of the main causes for the workers' early retirement.

The lower back is followed by the neck and upper extremities in terms of exposure to WRMSDs [4, 9]. Lastly, the lower limbs are the anatomical area less exposed to WRMSDs [4, 5]. This points out to the upper body being the area where the human worker is more susceptible to develop these disorders.

To diminish the exposure of the workers to the occurrence of WRMSDs, a high focus on the design of the worker's task and also of the work cell needs to be revised. Among the major risk factors, one of the principal are **awkward postures** during the execution of a work task. These can be defined as deviations from the natural body posture, which leads to "poor blood flow and pressure on tendons and ligaments" according to EU-OSHA [4].

As a means to reduce the economical and health impact related with the prevalence of these disorders, it is necessary to reevaluate and improve the current workplace ergonomics.

1.1.2 Methods for Ergonomic Risk Assessment

To mitigate the prevalence of WRMSDs, several methods and tools were devised and integrated in the workplace. These tools serve to monitor, and consequently correct or prevent the prevalence of awkward postures in the workplace. There are currently three main conventional ergonomic tools that the ergonomists employ: self-reports, observation-based methods, and intstrumented methods [15–18].

Self-reports are comprised of questionnaires and interviews, in which the worker reports their status and conditions. This method, albeit simple, low-cost and effective, has some limitations: it relies on the perception of the worker, which is subjective, and may be flawed. It also depends on the worker's interpretation of the ergonomist's questions [15, 18]. According to a study made by Spielholz et al. [16], they observed that self-reporting was the lesser of the three in terms of precision, with a tendency of over-reporting exposures. For this study the authors performed a comparison between the three listed ergonomic tools

Observational methods are based on the observation of the workers' routines and exposures in the workplace, by means of on-sight observation, or videos. These methods can be further divided into two separate methodologies: posture-based methods and more advanced observational techniques. The former are performed by ergonomists who personally observe the workers' during their routine. The assessment made by the ergonomists is then compared with proper ergonomic sheets, like the Rapid Upper Limb Assessment (RULA) [19] for example, where they can evaluate the posture of the workers they observed. Despite being considered practical, relatively simple, and non-invasisve, it is heavily dependant on analyst's level of expertise, and lacks in terms of exposure variability, repeatability and objectivity, and is more time-consuming [15, 17]. The more advanced observational techniques are based on the video recording of the workers' routine, and applying autonomous software analysis to execute the ergonomic assessment [16]. Although it surpasses the posture-based method in terms of objectivity and repeatability, it still suffers from lack of variability, and other problems associated with video recording such as ambient occlusion.

Instrumented-based methods, or direct methods, approach the assessment of the worker's exposure using sensorial systems, placed on the worker. These systems acquire and evaluate the worker's exposure risk in real-time, without the input of dedicated personnel [15]. This leads to a more objective analysis in comparison with the alternative ergonomic assessment tools, potentially more accurate and time-effective results. Due to the nature of this work, the targeted sensorial system is the inertial-based system which is one of the main focus of several SOA ergonomic assessment tools [15, 20–22].

1.1.2.1 Industry 5.0 and Collaborative Robotics

The Industry 4.0 wave focused on the automation of the manufacturing process, which lead to several positive effects on the manufacturing industry, such as the rise in productivity and the development of cobots [23]. However, with the current growing competitive market and the new fashion of costumer with more specific demands, the industrial complex is following the tendency of connecting the production lines with the costumer's expectations [23]. This leads to the production of mass-customized products, which the full automated processes cannot fully conform. Therefore, an adaptation of the industrial complex's production process is needed, and the use of manual operations is key to its success [24]. Therefore, the combination of the human worker with the cobot needs to be guaranteed to accomplish the new skill-demanding tasks in mass. This is where the concept of Industry 5.0 enters the scene.

Human-Robot Collaboration is one of the focal points regarding the Industry 5.0 concept, referring to the cooperative interaction between the human worker and a collaborative robotic framework [25]. This leads to the combination of the versatility, dexterity and human intelligence of the worker with the effective, physical capacity, repetitive endurance and repeatability of the cobot [23]. This is followed by an increase in the human work's quality and efficiency, as well as a diminishing exposure to WRMSDs risk factors [23, 26]. This technology has the potential of directly intervening in the user's working pattern, by creating a positive shift in the workplace, leading to a diminishing prevalence of WRMSDs. An example of this is the use of robotic manipulators in the workstation, which is being more and more prevalent. However, these only tend to co-exist with the worker, with very limited degrees of real colaboration [27].

To further amplify this collaborative relation, a seamless and dynamic interaction between the worker and the cobot needs to be assured. To surpass this obstacle, the worker's intentions need to be known by the cobot. This could be achieved with the cobot having the capability of monitoring and interpreting the worker's motions and body language [27]. To this end, inertial, MoCap system frameworks can be employed in the manufacturing industry, in which a real-time and steady flow of motion data is acquired from the worker and sent to the cobot [24].

1.1.3 Problem Statement

There is currently a growing interest in reducing the occurrence of WRMSDs, as they have a very substantial health, and economic impact. With all of the reviewed ergonomic assessment tools, it was observed that the instrument-based methods had the most potential in terms of objectivity and repeatability. Although observational methods are still the most commonly employed ergonomic tool in the industry, they heavily depend on the analyst's degree of expertise.

Furthermore, with the growing tendency of mass-customized products, the worker is returning as the focal point in the manufacturing process along with the cobot. This collaborative relation is paramount in the new Industry 5.0 wave. However, to fully allow true collaboration between the worker and the cobot, the communication and understanding between both parts need to be assured. This can be achieved by establishing a constant flow of MoCap data, acquired using MoCap technology, from the worker to the cobot, so the worker's intentions are known and covered by the cobot.

This dissertation aims at improving an inertial, upper-body MoCap system to be applied to reduce the incidence rate of WRMSDs, and that can be included in the industry 5.0 concept. Furthermore, this system was designed so it could be integrated in a collaborative robotics framework, to not only assess the worker's ergonomics, but also to directly improve the user's manufacturing capabilities.

1.1.4 Goals and Research Questions

The end-goal of this thesis is the improvement of a **non-intrusive**, **low-cost**, **objective**, **instrumented**, **MoCap system**, which is to be integrated in a Human-Robot Collaborative framework.

The work for this thesis seeks to answer the following research questions:

- **Question 1**: What are the main requirements that need to be taken into consideration when devising an inertial MoCap system, that can comply with the user's needs, in an industrial setting?
- **Question 2**: How to improve a MoCap smart-garment in terms of usability, and performance, while maintaining its low-cost feature?

To achieve these objectives, the following goals were established:

- **Goal 1:** Perform a critical review of the available literature regarding upper body inertial MoCap systems, focusing on the used Fusion Filters, STS calibrations, Wearable configurations and integrated Hardware, to understand what are the existing solutions.
- **Goal 2:** Assess the limitations of the previous version of the proposed system, and identify the focal points that need to be addressed, in order to improve upon the previous iteration.
- **Goal 3:** Develop the system's garment, in accordance to the defined usability requirements, identifying the best type of garment, textile, and other features.
- **Goal 4:** Develop the system's hardware, identifying the best sensors, processing unit, biofeedback circuit, power supply unit, and WiFi module for the project, to the best of the author's knowledge.
- **Goal 5:** Develop the system's software and firmware, and establishing the WiFi communication setup between the wearable and the main station.
- **Goal 6:** Validate the system in accordance to the specified technical requirements, and in usability terms using an usability-based questionnaire.

1.1.5 Methodology

This work followed a user-centred design approach, based on [28], which addresses the process of a product's iterative design, while considering the opinion of users. It is mainly divided in three main steps, which are illustrated in Fig. 1:

- **Analysis:** Gathering data from the previous version of the system. Determine its limits and flaws, and verify if the system conforms with the predefined requirements. Perform tests with human users to obtain these results. Furthermore, review the SOA around inertial MoCap systems, with a special focus on commercial systems, to help plan the development of the new version. Lastly, define a plan and the requirements that are to be addressed when designing the new iteration.
- **Development:** This phase concerns with the development of the new version in terms of hardware, software and the system's suit. It will be based on the data acquired from the tests performed with the previous iteration.

- **Post-release:** Field testing the prototype to ascertain if the developed system conforms with the predefined requirements, Moreover, perform tests on human users to define the standard of usability of the new system. Furthermore, compare the results obtained with the new version, regarding the previous iteration, to assess the system's improvements. Lastly, define the limits of the new iteration to help improve future versions.

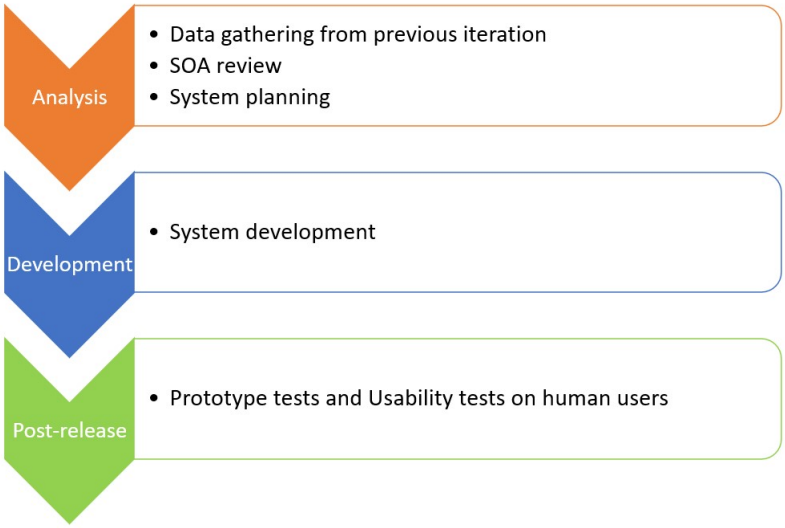

Figure 1: System's design methodology.

1.1.6 Contribution to Knowledge

This dissertation led to the development of a low-cost, inertial, non-intrusive wearable MoCap system, equipped with 6 vibrotactile motors for posture monitorization and biofeedback. Furthermore, this system is to be integrated in a collaborative robotics framework.

1.1.7 Publication

The work developed for this thesis led to the publication of the following article:

- **A. Resende et al. "Ergowear: an ambulatory, non-intrusive, and interoperable system towards a Human-aware Human-robot Collaborative framework"**. In: 2021 IEEE International Conference on Autonomous Robot Systems and Competitions (ICARSC). IEEE, 2021-04, pp. 56–61. isbn: 978-1-6654-3198-9. doi: 10.1109/ICARSC52212.2021.9429796. url: https://ieeexplore. ieee.org/document/9429796/. [29].

1.1.8 Thesis Outline

This dissertation is divided in 6 Chapters:

- Chapter 2 addresses the reviewed literature, with an overview of the existing inertial wearable systems, commercial and academic, with a special focus on their wearable configuration, hardware, sensor fusion algorithms and STS calibration sequences.
- Chapter 3 showcases the design conceptualization of the developed wearable system, describing the usability, functional and technical requirements in which its design was based from. Furthermore, this chapter defines the reported limitations of the previous system.
- Chapter 4 describes the steps regarding the development of the different parts that comprise the system, namely the garment, hardware and software, and the selection process behind each of the followed strategy.
- Chapter 5 addresses the tests performed to validate the system in regard to the defined requirements, starting with the hardware validation, and ending with the usability and biofeedback strategy validation using participants.
- Chapter 6 discloses this dissertation, describing the conclusion of the work performed and the proposed strategies to further improve the system.

2

State-of-the-Art

2.1 Wearable Inertial Systems for Joint Angle Estimation

Wearable, inertial Motion Capture (MoCap) systems for joint angle estimation are currently being developed to be integrated in different aspects of the day-to-day life [30], such as workplace ergonomics [21, 22, 31–37], sports [38, 39], health and rehabilitation [40–43] or human-robot collaboration [44–47].

These systems are based on the use of Inertial Measurement Units (IMUs) that contain inertial sensors, accelerometer and gyroscope. Some of these IMUs are also complemented by a magnetometer (Magnetic Inertial Measurement Systems (MIMUs)). These sensors have significant limitations when used on their own. Therefore, to estimate the orientation of these measurement units, it is common practice to apply filtering algorithms capable of fusing the data from the different sensors to compensate for their limitations, improving the overall accuracy of the system.

Moreover, in these MoCap systems, the IMUs are attached to an anatomical segment, with the assumption that the orientation of the sensor module is aligned with the respective segment it is attached to. However, the positioning of the IMU is not perfect - there is always a misalignment between the frames of both bodies, leading to further inaccuracies. Therefore, some MoCap systems present Sensor-to-Segment (STS) calibration sequences that mitigate the effect of these positioning errors, by estimating and correcting the misalignment between the IMU and the anatomic segment.

2.1.1 Commercial Systems

The versatility around inertial MoCap systems led to the development of several commercial inertial motion capture systems. The most well-known company associated with these products is XSens (XSens Technologies B.V., Enschede, The Netherlands). XSens currently offer two complete motion capture MVN products, the XSens Awinda and the XSens Link [48]. The former is comprised of a skin-fitted shirt, velcro straps and wireless sensor modules that communicate wirelessly to a remote station that is connected to a personal computer. The user wears the shirt, and secures the sensor modules in the velcro straps, specifically, the sensor modules associated with the upper and lower-limbs, and pelvis. These straps

are then placed around and fixed to the respective anatomical segment. The shoulders' and the stern's modules are placed on the velcro straps, that are already sewn onto the shirt. Lastly, the head's sensor module is positioned inside a socket on a headband. The Xsens Link is, in turn, a wired MoCap system, in which the sensor modules are embedded in a full-body, tight-fitted, lycra suit, fixed on velcro patches that are sewn onto the textile. Lycra, being a textile with a very high degree of elasticity, is suitable for when the garment needs to be adaptable to the user's body. Both of these products have their respective and distinct use. The XSens Link is more appropriate for situations where large distances need to be covered, higher frame rates are needed, to capture multiple people or for more intense motions. Furthermore, it has a higher battery life than the Awinda. In turn, the XSens Awinda is more adjusted when capturing regular motions and capturing multiple people with the same equipment, according to XSens. Fig. 2 showcase both the XSens Awinda and the XSens Link.

(a) (b)

Figure 2: Overview of the a) XSens Awinda and the b) XSens Link. In [49]

Other MoCap solutions available in the market, like the Rokoko SmartSuit Pro (Rokoko, Copenhagen, Denmark) [50], which, in terms of wearability, is similar to the XSens Link. Like the latter, it is composed of a full-body, skin-fitted garment with sensors embedded in it. This system, however, uses nylon based fabric as a textile. Furthermore, it also uses velcro to fix the inertial sensor systems to the suit, which is complemented with a fixing strap on the exterior part of the outfit.

The Perception Neuron MoCap line (NOITOM Ltd, Miami, FL, USA) offers three different products of MoCap systems, all of them wireless, at three distinct price ranges [51]. All of them have a familiar setup, using body straps to fix the sensor modules. These systems were developed to be mainly used in gaming and virtual reality situations, medical and sports analysis, and staging performances [52].

Other commercial brands are the: Nansense (NANSENSE Inc., Los Angeles, USA) [53], AiQ Synertial (AiQ Synertial, East Sussex, UK) [54], Shadow Motion (Motion Workshop, Seattle, USA) [55], STT Systems (STT Systems, San Sebástian, Spain) [56], APDM (APDM Wearable Technologies Inc., Portland, USA) [57], and Trivisio (Trivisio Prototyping GmbH, Trier, Germany) [58].

The State of Art (SOA) presents several studies that made use of commercial systems for joint/segment angle/position estimation. Some of these studies focused on the validation of inertial commercial MoCap products, for the estimation and monitoring of the upper limbs in various situations, e. g., to analyze workplace ergonomics. Of these commercial systems, the most used was the Xsens Awinda by a significant margin [59].

I. Poitras et al. [60], concurrently validated the use of the Xsens Awinda system to estimate the shoulder joint angle, against a setup of 9 Vicon MX (Vicon Motion System Ltd., Oxford, UK) cameras, that served as ground truth for isolated shoulder movements and complex lifting tasks. The authors concluded that the Xsens Awinda system was valid to estimate the shoulder joint angle and evaluate shoulder movements.

To monitor ergonomic risks in the workplace in real-time, Giannini et al. applied an XSens MVN suit (17 IMUs) and a Perception Neuron MoCap suit (34 IMUs), combined with an EMG system [21]. The ergonomic risks are assessed from the resulting kinematic and EMG data, by ergonomic risk assessment standards, namely: the National Institute for Occupational Safety and Health (NIOSH), Snook & Ciriello, Rapid Entire Body Assessment (REBA) and the Strain Index. Moreover, the system was also designed in order to perform the segmentation of the user's activities in the workplace. The system was tested in an industrial environment - a cargo ship which has a high prevalence of magnetic disturbances due to the high quantity of metallic objects - with real workers. The XSens system was considered for the study, **as preliminary tests indicated that it was more immune to magnetic disturbances compared to the Perception Neuron suit**. The results obtained in the tests pointed towards the fact that the proposed system was effective in the ergonomic evaluation of the workers, when compared with the evaluation performed by three raters from video captures.

R. Sers et al. [61], studied the use of a Perception Neuron setup, the Perception Neuron 32 - Legacy, to assess its accuracy in estimating the angles of the neck, thorax and shoulder, by comparing its values against a setup using the Vicon MoCap system, composed of 12 cameras. The study's main purpose was to validate the use of this inertial MoCap system to monitor surgeons' ergonomics during surgical tasks. The protocol was composed of 9 isolated, and uni-axial movements. With this study, it was observed that the IMU suit was adequate in measuring the upper body, in isolated movements, during low duration trials - 10 seconds - with the exception of the neck extension, in which the inertial system had a lower level of concurrency during the movement.

Still in the Perception Neuron, X. Robert-Lachaine et al. [62] also tested the efficacy of this MoCap suit. In this case, the validation's purpose was to evaluate the performance of a more low-budget MoCap system, the Perception Neuron, in monitoring the whole-body joint angles during the execution of a task in which the participants moved boxes from one side of a platform to another, for about 32 minutes. To

serve as ground truth, an optical MoCap system - Optotrak (Optotrak, Northern Digital, Waterloo, Canada) was used. It was observed that the Perception Neuron was adequate during the test, demonstrating an error inferior to 5° for most joints. However, as a result of those tests, it was also stipulated that the Perception Neuron had a worse performance when compared with the Xsens.

Menychtas et al. [33] used the Nansense motion capture suit, with 50 IMUs, to create an upper-body model, in order to extract kinematic data from 3 males in a laboratorial environment, and 4 workers in a TV manufacturing industrial environment. The kinematic system was used to extract the user's joint angles, and furthermore, to obtain the joints' torques. The purpose was then to monitor this data during a task, assessing its deviation from the average effort each joint puts into the task, and perform an ergonomic evaluation for each joint individually.

An overview of the analyzed commercial MoCap systems is presented in Table 1. These systems range from 17 to 22 sensors in full body application. Sensor placement is the same for both Xsens system, with 11 of the 17 sensors placed on the upper-body, on the following locations: pelvis center, right and left scapula, head, sternum, right and left upper arm, right and left forearm, and right and left hands. Perception Neuron Pro has a similar sensor placement, also with 11 of the 17 sensors placed on the upper-body. The sensors are placed on the same location as Xsens with the exception of the sensor placed on the sternum, which is placed on the upper-back, next to T4 vertebrae. Rokoko's Smartsuit Pro has 13 of the 19 sensors on the upper body, namely on the right and left side of pelvis, right and left side of middle back (thoracic area), right and left scapula, head, right and left upper arm, wight and left forearm and right and left hand. As for the Nansense BioMed, manufacturer information is not very clear regarding sensor placement.

From Table 1, it is possible to observe that the options made available by XSens have the best reported static and dynamic accuracy, supporting its selection as the "gold standard" when it comes to inertial motion capturing.

Although the XSens products and the Perception Neuron were validated for motion analysis in the described studies, to the best of the author's knowledge, they are not being used in industrial contexts on a daily basis. One possible reason is the high price of their hardware, as showcased in Table. 1, and even costlier user licenses for their movement analysis tools. The Rokoko Smartsuit, for example, presents one of the least costly hardware. Nevertheless, the system has not yet been validated for biomechanical analysis and it is promoted by the company for gaming and movie animations.

In turn, Academia also followed this trend to develop IMU-based wearable technology. These, however, tend to be custom-made and specific for an application. Nevertheless, they were also reviewed.

Table 1: Overview of commercial, inertial Motion Capture systems. Data is discriminated in - Brand, Model, Conectivity, nºof Sensors, Configuration, Dynamic Accuracy, Static Accuracy, Battery Autonomy, Calibration, Hardware Price. P (Pitch), R (Roll), Y (Yaw). Adapted from [63].

Brand	Model	Connectivity	nº of Sensors	Configuration	Dynamic Accuracy	Static Accuracy	Battery autonomy	Calibration Sequence	Hardware Price
Xsens	Awinda	Wireless	17	Velco straps	P/R/Y 1°	P/R 0.2° | Y 0.5°	6 h	N-pose (or T.pose) + Walking sequence	8180 $
Xsens	Link	Wired	17	Lycra suit / Velcro	P/R/Y 1°	P/R 0.2° | Y 0.5°	8-10 h	N-pose (or T.pose) + Walking sequence	9225 $
Rokoko	Smartsuit Pro	Wired	19	Textile Suit / Velcro	P/R/Y 1.5°	-	External Powerbank	N-pose	2495 $
Nansense	Indie	Wired / Wireless	15	Body suit / Foam padding	P/R 0.7° | Y 1.4°	P/R 0.5° | Y 1.0°	14 h	I-pose + other interactions	>6299 $
Nansense	Pro	Wired / Wireless	18		P/R 0.7° | Y 1.4°	P/R 0.5° | Y 1.0°	12 h		
Nansense	Biomed	Wired / Wireless	22		P/R 0.7° | Y 1.4°	P/R 0.5° | Y 1.0°	10 h		
Perception Neuron	3	Wireless	17	Body Straps	P/R 1° | Y 2°	P/R 0.5° | Y 1.5°	6 h	Upper-body: A-pose + T-pose	2399 $
Perception Neuron	Studio	Wireless	17	Body suit + Body Straps	-	P/R 1° | Y 2° *	5.5 h	N-pose + T-pose + S-pose	5999 $
AiQ Synertial	Synertial CS-2200	Wired or Wireless	18	Full body suit	-	P/R 1° | Y 2° *	2+ h	-	10650 $
Shadow Motion	Shadow	Wired	17	Shirt + body straps	P/R/Y 2°	P/R/Y 0.5°	8 h	T-pose	3999 $
STT Systems	iSen 3.0	Wireless	1 to 16 (max)	Straps	P/R/Y <2° *	P/R <0.5° | Y <2°	3.5 h	N-pose (can include T-pose)	Contact
APDM	Full Body Package	Wireless	15	Elastic Straps	P/R/Y 2.80°	P/R 1.15° | Y 1.50°	12 - 16 h	-	Contact
Trivisio	Light Motion Suit	Wireless	15	Straps	-	P/R 1° | Y 2° *	3 h	-	Contact

2.1.2 Academic Systems

S. Santos et al. [22] developed an upper-body, fully wireless, inertial motion tracking system capable of capturing the motions of four segments: the torso, the upper arm, the forearm, and the hand. The developed system can capture 8 Degree of Freedoms (DOFs) in total. The purpose of this system was to extract the orientation of the upper-body joints, and with that information, calculate the ergonomic risk of the user, using a Rapid Upper Limb Assessment (RULA)-based classifier. The system was validated against a gold standard ground truth (Vicon).

G. Ligorio et al. [64] developed an inertial motion capture system, using only the data provided by the accelerometers and gyroscopes, without applying the magnetometer. The sensor used was the MPU-9250 (TDK Invensense, San Jose, USA). The system was designed to monitor the joint angles of the right upper limb (shoulder, elbow and wrist).

To address the issue of workplace ergonomics, with a focus on the manufacturing industry, Caputo et al. [20] developed a low-cost, inertial MoCap system, designed for the user's ergonomic posture evaluation. The MoCap system is comprised of 10 sensor modules located on the upper limbs, trunk, pelvis, and lower limbs. Each module is composed of an IMU (MPU-6050), magnetometer (HMC5883L) and a CPU (STM32F103). For the attitude estimation, an Extended Kalman Filter (EKF) was used. The proposed system was then capable of using the attitude data to evaluate the posture of the user, through the European Assembly Work Sheet (EWAS). This system was tested in an industrial environment - automotive assembly line - with 2 real workers, to analyze their working postures during an assembly task.

M. G. L. Monaco et al. [32] designed a procedure which used a combination of an inertial MoCap system and surface electromyography, for biomechanical risk monitoring. This setup's purpose was to analyze the ergonomics in an industrial environment. The inertial MoCap system is an upper body configuration of 2 sensor modules, with 4 IMUs each [65]. The IMUs are positioned on the trunk, arm, and forearm. The system also uses a Raspberry Pi as a processing station, for data recording and preprocessing, and it is powered by a battery. This setup is illustrated in Fig. 3.

This setup was tested to evaluate the posture on real life workers, in an industrial context, in which the task revolved around assembling the central cabinet in a car.

M. I. M. Esfahani et al. [66] developed a low-cost, inertial MoCap system, named Sharif-Human Movement Instrumentation System (SHARIF-HMIS). In terms of hardware, it consisted of 18 custom IMUs, positioned around the whole body. The fusion algorithm used was a Kalman Filter (KF), based on the filter proposed in [67], with an adaptive factor based on the one in [68] while taking into account the magnetic disturbances. The overview of the proposed system is present in Fig. 4. The system was evaluated against an 8-camera Vicon MoCap setup, in estimating the shoulder orientation, with the volunteer performing a combination of 1-axis, 2-axis and 3-axis movements. The tests showed that the system had a maximum error of 4.11° (Root-Mean Squared Error (RMSE)) in the Yaw angle, during scapular movement, and a minimum error of 1.41° (RMSE) in the Roll angle, for a horizontal extension movement.

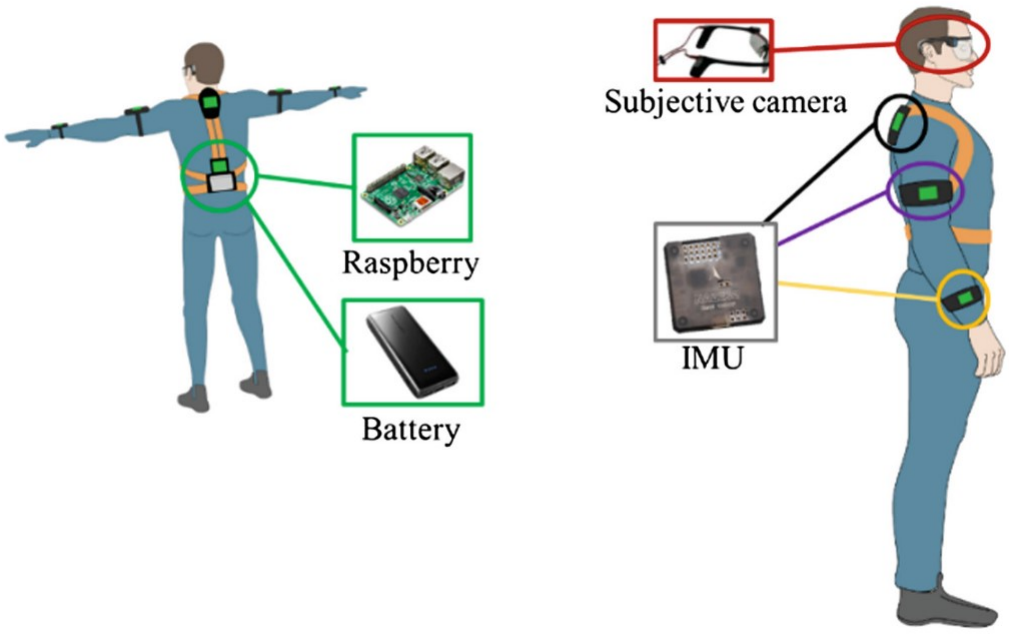

Figure 3: Inertial upper body MoCap configuration. By [32].

Aiming to track the user's arm and control a robot manipulator, Shinternov et al. designed a wearable, inertial motion capture system, with 7 DOFs [45]. with two IMUs and 1 goniometer, proposing an alternative to the 3 IMU-based arm tracking systems.

Pastor et al. also developed an inertial motion capture system to estimate the user's upper limbs' joint angles, for robot teleoperation, with the main difference being the use of 2 flex sensors, in combination with 2 IMUs [69].

Looking to develop a cheaper alternative in regard to the available commercial systems, a fully customized, wired, full-body MoCap system was proposed by Ancans et al. [63]. The wearable configuration and the hardware of the suit was extensively described. In this publication, non-technical concerns such as wearability, washability, protection against humidity, among others, are addressed. The base of the wearable is comprised of a full-body suit, with the sensors attached to it by specialized textile connectors. Furthermore, this system uses copper wires fully integrated into the textile. An overview of the developed MoCap setup is shown in Fig. 5. The system is composed of 18 sensor modules, which contain the BNO055 (Bosch Sensortec GmbH, Reutlingen, Germany) inertial measurement unit, which have an embedded fusion filter an data calibration algorithm. This system was validated in terms of its orientation estimation accuracy, against an optical MoCap system - SMART DX system (BTS Bioengineering Corp., Quincy, MA, USA), for a list of defined movements: squatting, lunging, push-ups and bending. From the results, the authors reported that the proposed MoCap system obtained a static error inferior to 1° and a dynamic error inferior to 2°, for a Range of Motion (ROM) of 90°. The authors estimated that the hardware

Figure 4: System overview by [66].

cost, regarding their 15-sensor configuration, was about 500 €.

2.1.3 Wearable Configuration

For the wearable setups, commercial systems were mostly targeted, due to their higher wearability standard and proven marketability, as these systems need to be comfortable, convenient, and attractive for clients to buy. Furthermore, the wearable aspect is also designed to maximize the performance of the system.

In the Xsens Link, all of the electronics are embedded in a lycra full-body suit, composed of two layers. The electronic modules are fixed on velcro patches, present in the inner layer of the suit. In terms of cabling, the cables pass through textile tunnels, that connect certain keypoints, like the arms' segments with the back segment. The inner layer is accessible through zippers. These zippers are present on both arms, and on the back as well. Fig. 6 demonstrates this setup. In this system, the processor and battery pack are located on the left side and lower side of the lower back, respectively.

Another product that presents a similar setup to the Xsens Link is the Rokoko Smartsuit Pro [50]. It is also composed of a two-layered, full-body suit, with the cables running through a conjunction of zippers and tunnels. The sensor modules are fixed on the inner-layer, through velcro patches. To reinforce this attachment method, velcro straps are used on the outer-layer. An overview of this setup is present in Fig.

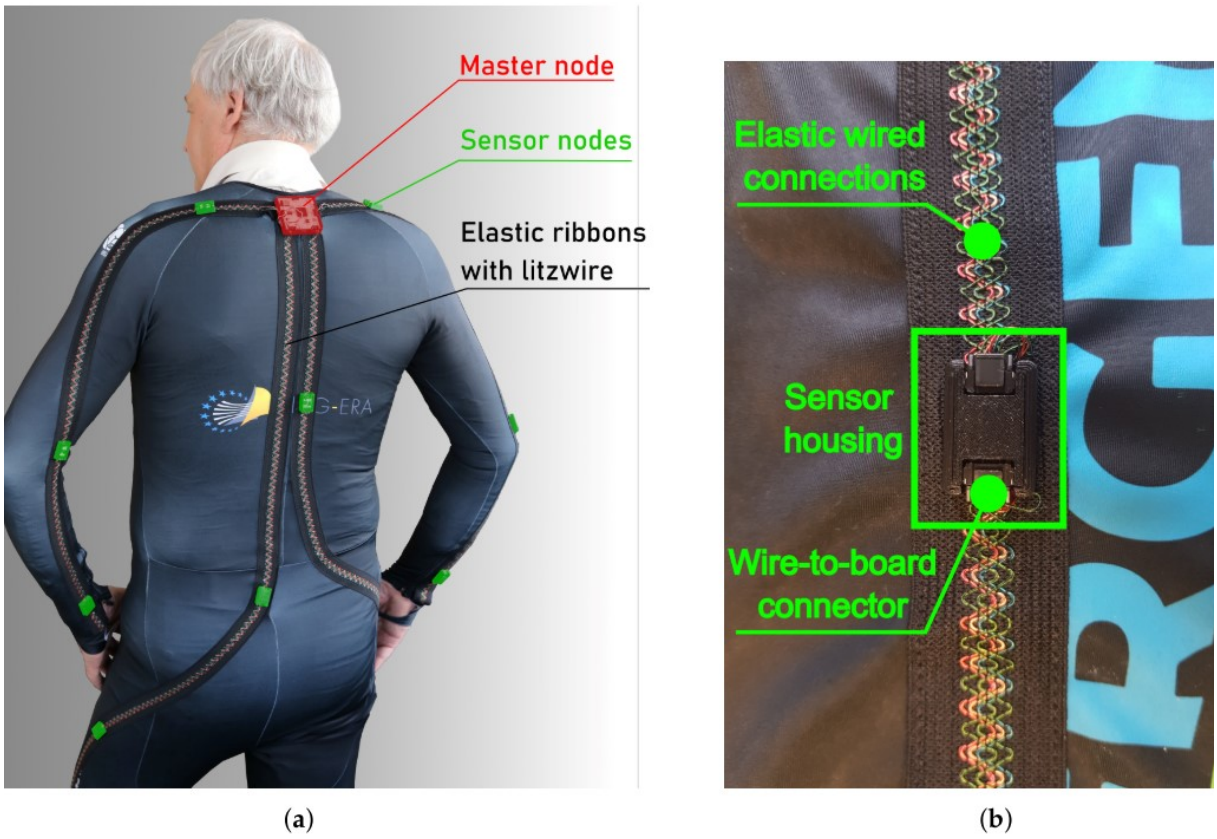

Figure 5: Proposed MoCap system. a) Overview of the setup. b) Zoom-in on the sensor module. Figure from [63].

7.

One of the bigger differences between this system and the Xsens Link is that in the smartsuit, the processor and the battery are positioned along the column, at the lower back and the middle back level, respectively.

2.1.3.1 Sensors' attachments

The attachment of the sensors to the user's body is important to take into consideration when designing an inertial MoCap system, as the way the sensor is attached to the respective segment will not only affect the overall wearability of the system, but will also affect its performance in orientation estimation [70].

In terms of sensor attachments, the most common ones used in commercial MoCap systems are: velcro patches and straps. Nevertheless, more types of sensor attachments were also reported: textile pockets, foam padding, among others.

The Xsens Link, for example, makes use of velcro patches - as previously mentioned - directly fixed onto an elastic inner layer of the bodysuit. An example of this configuration is demonstrated in Fig. 8.

Other alternatives were also reported. The Nansense MoCap suit utilizes foam paddings for the sensor placement [53].

Figure 6: Xsens Link setup with a) displaying the back of the suit and b) displaying the upper eight arm segment.

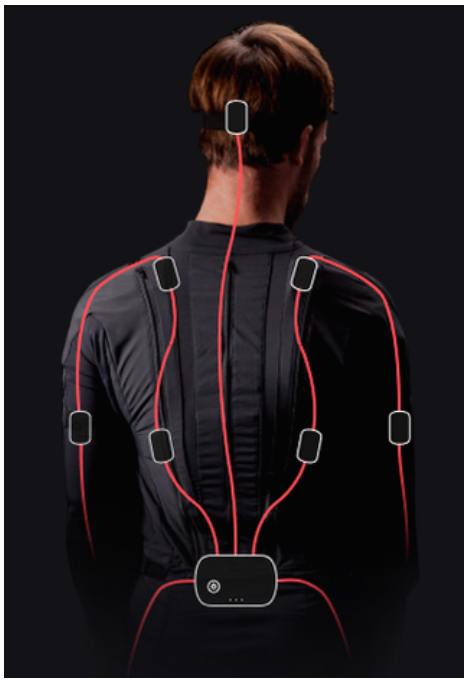

Figure 7: Rokoko Smartsuit Pro setup.

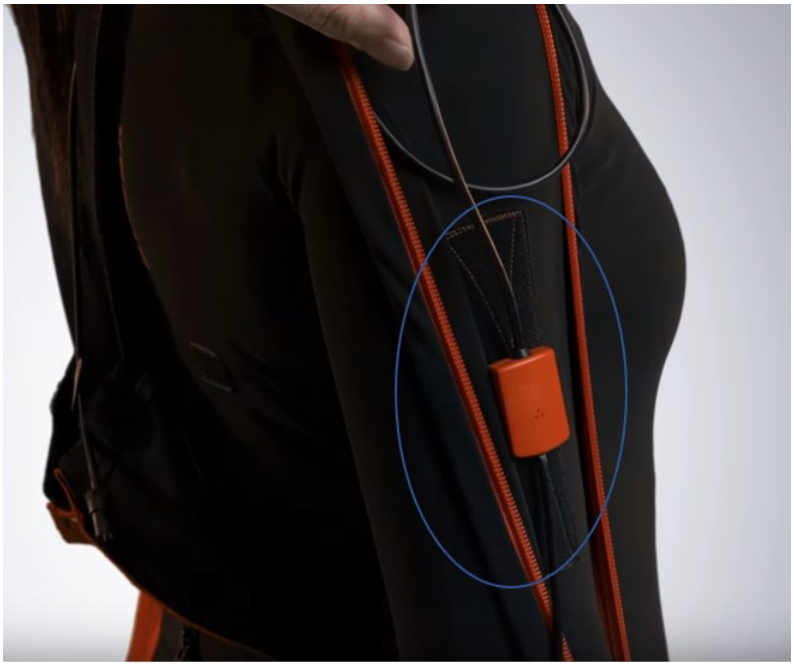

Figure 8: Velcro attachment (surrounded by blue) in the Xsens Link.

For the rest of the sensors, various types of attachments were reported. As stated, the Xsens Link and Rokoko Smartsuit makes use of velcro patches. The latter is complemented with external elastic straps which pressure the top of the sensor modules. In Fig. 9 an example of this type of attachment is shown. Furthermore, a tightening strap used used to fix the sensor on the lower back.

Figure 9: a) Attachments used in the Rokoko Smartsuit Pro, including b) tightening straps.

In the Shadow Motion MoCap system, straps are used to fix the sensor modules onto the arms, while textile pockets fix the modules on the trunk. In Fig. 10 an example of this setup is shown.

Figure 10: Attachments used in the shadow motion MoCap suit. Straps inside the red circle and pocket inside the yellow circle.

In all of the reviewed commercial MoCap systems, elastic headbands were used to fix the IMU on the head, for the setups that measured the head kinematics.

Other types of attachments were also used. For example, Ancans et al. [63] fixed each sensor module by embedding the sensor connector and housing within the textile.

Pomiersky et al. heavily addressed the attachments and fixation system of their inertial MoCap system [70]. During the execution of tasks, where the participants had freedom of movement, they noticed that the sensors were sliding in regard to the segments. The authors used standard body straps, with fasteners so they can be adapted and fitted to the respective segment - similar to those used in the Rokoko Smartsuit Pro. Moreover, they added a layer of neoprene o the straps to avoid them slipping without a lot of tightening.

Barraza Madrigal et al. used a sports armband to fix their measurement unit onto the back of the participants' upper arm [71].

Furthermore, Marin et al. [72] performed a review in their publication, presenting an overview of various different types of sensor attachments for MoCap systems.

2.1.4 Cabling Configuration

Different wired MoCap systems present different types of logistics in regard to cabling. The primary objective in this analysis, was to review the type of connectors, and how the connections were made

between modules.

The most common type of cabling strategies reviewed, each of the bodies' limbs, and the trunk plus head, were regarded as different ramifications, with each ramification being composed of one main cable [63].

In terms of connectors, some systems use connectors embedded in the sensor modules, to establish the connection between the IMU and the wiring. These examples can be seen in the case of the Xsens Link, the Rokoko Smartsuit pro, and the Shadow Motion Suit. Specifically to the Smartsuit Pro, it is known that at the entrance of the sensor housing, a strain relief - due to the lack of a connector - allowing the protection of the cable wiring from external tensions. Besides this, the Printed Board Circuit (PCB) possesses a wire-to-board connector for the cable wiring. This setup can be observed in Fig. 11. The connections, in both of these systems, are done through cable-to-cable connectors, between the respective sensor modules.

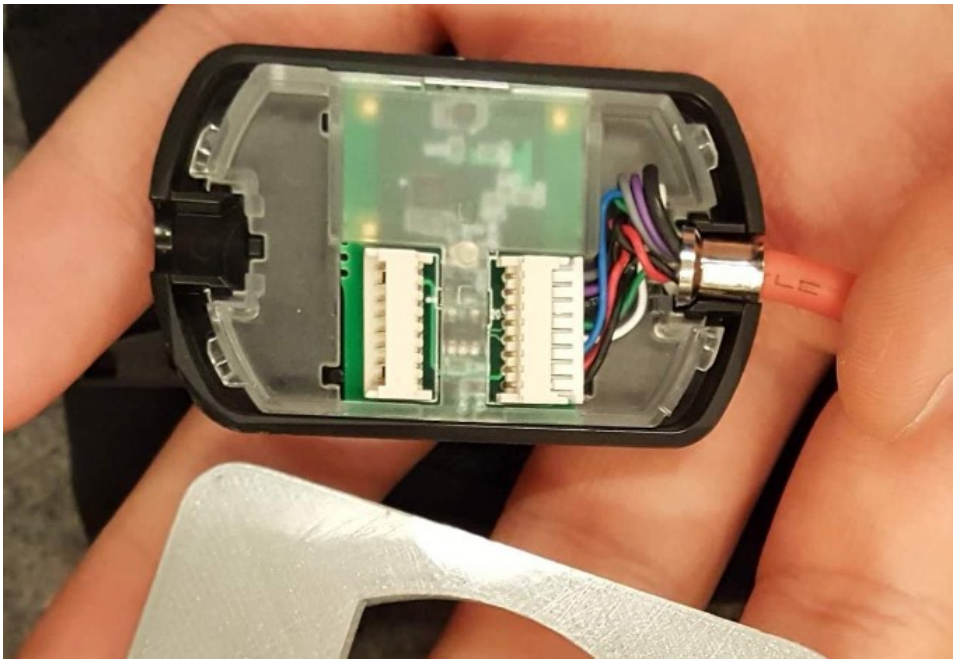

Figure 11: Inside of the sensor housing of the Rokoko Smartsuit Pro.

In other cases, the cables connect directly to the PCBs, with the connector located on the place of the sensor module [63].

2.2 Joint Angle Estimation

This section presents the more common STS methods and fusion filters used to track the user's motion.

To be able to analyze the user's posture, it is first required to determine the 3D angles of the user's joints. That is attainable through the use of the inertial sensors' gyroscope, accelerometer and magnetometers' (if used) measurements, after applying a filter that is capable of fusing these sensors' measurements, with the purpose of obtaining more correct orientation estimates.

To determine the orientation of the IMU, firstly, the rotation between the previous state and the current state needs to be known. That can be obtained by integrating the gyroscope's measurements during the transition between these frames. Over the time, this leads to the accumulation of a bias, which will deviate the measured angular velocity in regard to the real angular velocity. Because of this, the estimate of the angular orientation of the sensor's body will decrease in performance.

To mitigate this effect, the magnetic and accelerometer's measurements can be used to correct the measured angular velocity. The acceleromenter gives information regarding the inclination of the sensor's frame, by comparing its orientation with the gravity's vector direction, assuming that the IMU is static. To complement the accelerometer, in regard to the horizontal direction, we have the magnetometer. This sensor gives the orientation in regard to the magnetic north pole's direction. In other words, through this sensor's readings, it is possible to estimate the IMU's heading. Thus, by combining both of these sensors, we can use the world reference to correct the angular velocity readings. Nonetheless, although both of these sensors can be used to correct the gyroscope's drift, they also have drawbacks. In an ideal condition, the accelerometer will only measure the earth's gravity acceleration, but in most of the times, the IMU will be subjected to external accelerations, primarily due to the user's segments movements [73].

2.2.1 Sensor-to-Segment Calibration

One incremental step for joint angle estimation systems using inertial sensors, is the STS calibration, which revolves around the association between the sensors' coordinate frame with the respective anatomical segment's coordinate frame. This calibration significantly contributes to the overall accuracy of the system [74, 75].

Four main segment-to-sensor calibration strategies were reported according to Pacher et al. [74]: manual calibration, static calibration, functional calibration and anatomical calibration.

Manual calibration is based on the manual alignment of the sensor body orientation with the respective anatomic orientation, in a way that the sensor's coordinate frame overlaps with the segment coordinate frame [74].

Static calibration [64, 76, 77] is comprised of known static postures that the user needs to perform, which are generally simple to execute. In this type of calibration, as the pose is known, the segments' orientations are assumed, and the sensor frame misalignment is calculated in regard to the expected anatomical orientation. In this approach, the global frame of the inertial sensor is estimated using the accelerometer, for the longitudinal axis, and the magnetometer, for the horizontal axis.

Functional calibration corresponds to the execution of uni-axial, uni-joint movements performed by the user [64]. Through these movements, it is possible to estimate, per movement, the orientation of

the frame's axis.

The last one - **anatomical calibration** - corresponds to the detailed identification of the segments' frame, through the study of anatomical landmarks, using the proper instruments or devices, for example, calipers [74, 78, 79]. The inertial sensors' frames are then compared with the respective segments' frames.

Through the information described in Table 1, it is possible to observe that the most reported type of STS calibration sequences, in commercial systems, are based on static postures, namely based on the N-pose and the T-pose. In Fig. 12.

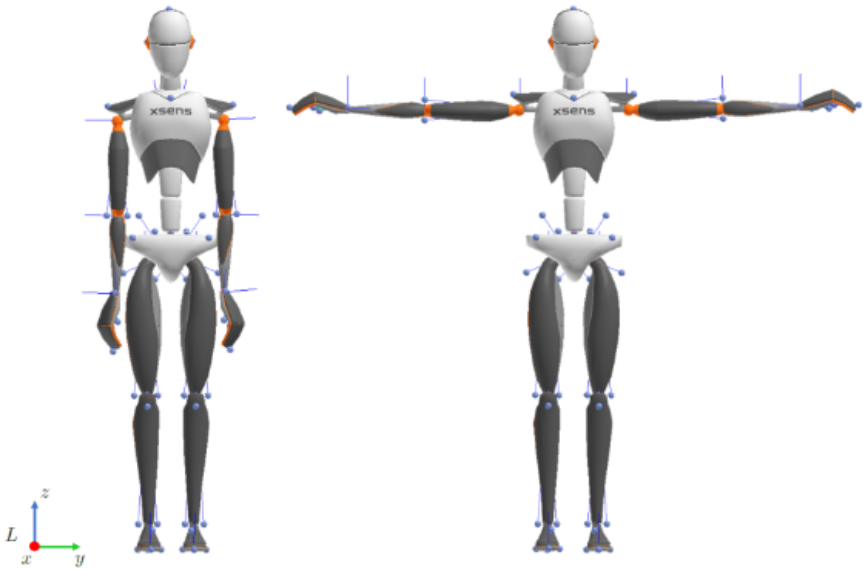

Figure 12: Demonstration of the N-pose (left) and the T-pose (right), by XSens [48].

Bouvier et al. [75] studied the performance of various STS calibration sequences (manual, static and functional), in the orientation estimation of uni-axial ROM of the following joints: wrist, elbow and shoulder. A more complex movement that consisted of multiple joints' motions was also assessed. The study was executed on 10 healthy participants, the inertial MoCap system used was a 4 MTw (Xsens) sensor setup, and the ground truth corresponded to a 10 optoeletronic camera system (Eagle 4, Motion Analysis Corporation, CA, USA). The authors stated that, when used individually, **functional calibration can only define one axis for one joint for each movement, unlike the manual or static sequences that can define the full orientation of the analyzed segments**. So, for this reason, the calibration sequences were selected in two ways: a static or manual calibration, or a combination of static or manual calibration with a functional calibration. The results from the tests showed that the difference in accuracy between the different types of calibration sequences. The authors also believed that the discrepancies may be more associated with the way the tests were executed, more so than the chosen calibration sequences.

In [64], the authors proposed a calibration sequence based on a static pose - N-pose - followed by functional calibration movements. In this last sequence, the user goes from the N-pose to perform a 90° shoulder flexion while keeping the arms extended. During this transition, the gyroscope measurements

are normalized, attaining the medio-lateral direction of the respective segment. One limitation of this combination, according to the authors, is that it showed poor consistency between different users. Therefore, extra computation sequences, based on grid algorithms and cost functions, were added and proposed to mitigate this limitation.

Zabat et al. [77] developed an upper-limb, static calibration method, in which the user performed 21 predefined postures for the upper limb, starting on the neutral pose. The calibration sequence is illustrated in Fig. 13. This method involves the use of 4 IMUs, positioned on: the hand, forearm, upper arm and thorax.

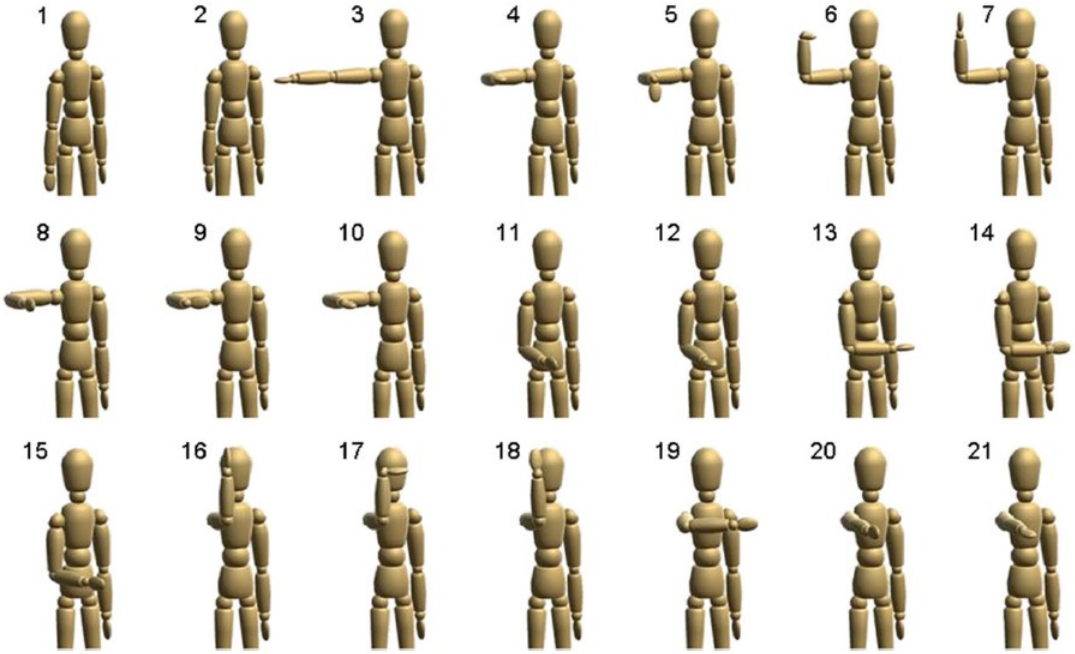

Figure 13: Calibration sequence as defined by Zabat et al. [77].

Each of the postures corresponds to a 0° or 90° deviation for the distal segment, in regard to the proximal segment, with the thorax always remaining static. The first pose, the N-pose, has the objective of performing an initial calibration phase, in which the sensors' coordinate frames are assumed aligned with the respective segment's coordinate frame, except for the thorax segment. For the thorax segment, the vertical axis of both the sensor's coordinate frame and the segment's coordinate frame, are aligned through the world's gravity axis.

The static calibration sequence comprised of three predefined poses - N-pose, T-pose, arms on the front - was proposed in [76], for a full-body inertial motion capture system. Using a window-based, double-threshold segmentation algorithm, the system discards the measurements obtain during the transitional

movements performed by the users, when switching poses. After the segmentation, the orientation estimations are obtained for each posture. Furthermore, the calibration sequence is complemented by an average algorithm with the objective of suppressing shaking during the static phases.

2.2.2 Sensor Fusion Filter

The literature review regarding fusion filtering led to the distinction of two main classes of fusion filters: the KF, and the Complementary Filter (CF).

Three reviews focused on the characterization of fusion filters were studied, namely [80–82]. In the work of Nazarahari et al. [80], a general overview of different types of fusion filters for inertial units. Moreover, it also approaches methodologies for filter gain-tuning, and rejection of disturbances in the measurements. The authors in the publication defined the incremental characteristics for an efficient inertial Fusion Filter, e.g., sensor calibration, gyroscope bias estimation and suppression, accelerometer and magnetometer disturbance mitigation and adaptive gain tuning.

Fan et al. [81] performed a benchmark between a number of selected fusion filter algorithms: Ligorio's Dual Linear KF, with a Tri-Axial Attitude Determination (TRIAD) algorithm [83]; the quaternion-based EKF, with gyroscope bias estimation; the Gradient-descent Filter (GDA) [84]; and the Extended Complementary Filter (ECF) [85]. The ECF filter had two distinct functionalities: one uses the magnetometer (IECF) and the other doesn't (IECF6). The experiments tested the orientation estimation performance of each of these filters in situations with no magnetic disturbances and with magnetic disturbances. A 6 camera Vicon setup was used as ground truth. Moreover, in the same publication, the authors approached several methodologies to mitigate the effect of magnetic disturbance on the orientation estimation, and other methods to mitigate gyroscope bias.

Lastly, in [82], a survey of different upper-limb tracking methodologies was performed. The authors tackled the use of joint constraints, integrated in the fusion algorithm, to improve the accuracy of human motion tracking. Furthermore, a comparison between five fusion algorithms based on the: CF, Linear KF, EKF and Unscented Kalman Filter (UKF) was executed. The authors concluded that the method combining a KF with a QUaternion ESTimator (QUEST) algorithm provided the best results for attitude estimation.

The CF is comprised of a low-pass filter, and a high-pass filter. The low-pass filter serves to filter out the magnetometer and accelerometer measurements, during dynamic states, as these sensors should only be used in static/quasi-static states. In contrast, the high-pass filter's function is to filter out the low-frequency gyroscope measurements, as this sensor should be used to estimate the orientation during dynamic states [80]. CFs are well-regarded as a more computationally efficient alternative, in comparison to the KF [86]. In Fig. 14, the block diagram of a basic CF is displayed.

The KF [87] is one of the main fusion filter groups. It is comprised of a Minimum Squared Error (MSE) algorithm based on the estimation of a combination of variables present in a state vector. The filter works in a combined two-step cycle: a prediction step, and an update step. Both steps are defined by a mathematical model, which can be represented by Eq. 2.1, as stated by [80]:

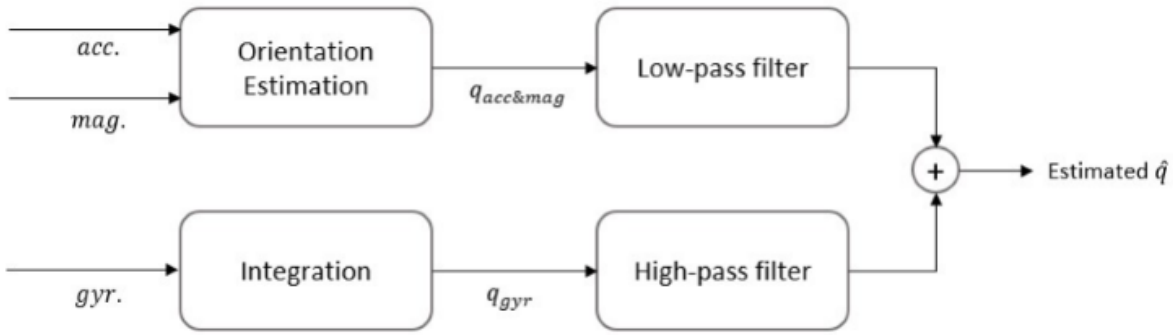

Figure 14: Schematic of a basic CF, from [80].

$$\begin{aligned} x_{t+1} &= f_t\left(x_t, u_t, w_t\right) \\ z_{t+1} &= h_{t+1}\left(x_{t+1}, v_{t+1}\right) \end{aligned} \tag{2.1}$$

With the first equation representing the basis for the prediction model, and the second equation the basis for the measurement model. x_t, u_t and w_t represent the state vector, the control input (most commonly gyroscope measurements for orientation estimation), and the process noise, at time t, while x_{t+1} is the predicted state vector at time $t+1$, and f_t is the state transition function. In turn, v is the measurement noise, z is the measurement vector with h being the measurement equation. The measurement vector is commonly composed by the accelerometer and magnetometer sensor readings, in the context of inertial orientation estimation.

The process noise w and the measurement noise v correspond to the amount of uncertainty related to the prediction and the measurement model, respectively. These factors are defined in a way as to mitigate the inherent sensors' noise.

In the update step, an extrapolation of the current step is done through the combination of the previous step, and the current sensor measurement (in this case gyroscope). A process noise matrix is added in this last step to estimate the gyroscope measurement noise, adding an error factor to the update step.

In both of these classes, several types of filters were reported, e.g.: Linear KF, UKF, EKF, Non-linear Complementary/Mahony Filter (NCF), Madgwick's Gradient Descent Algorithm (GDA) [20, 38, 64, 88, 89].

Although both the accelerometer and magnetometer have specific limitations, it is known that the impact of the magnetic disturbances affecting the magnetometer are much more performance-degrading compared with dynamical motions for the accelerometer [90]. Furthermore, due to the **high prevalence of ferromagnetic materials in an industrial environment, its use may be compromised in these situations.** Due to this susceptible nature of the magnetometer for magnetic disturbances, various authors proposed magnetometer-free fusion filter models, using only the accelerometer and gyroscope readings [64, 91, 92].

2.2.2.1 Kalman Filters

The most analyzed filters belonged to the family of the KFs [93]. Duan et al. [93] for example proposed a quaternion-based KF, complemented by a Second Estimator of the Optimal Quaternion (ESOQ-2) algorithm for body motion assessment. The ESOQ-2 algorithm is an time-efficient attitude estimation algorithm. Its purpose in this filter is to preprocess the magnetometer and accelerometer data, and furthermore, to compensate any external acceleration derived from body motion. Furthermore, the filter is complemented by measured joint angle constraints.

Ligorio et al. [94], proposed a Dual Linear KF (DLKF), in a parallel configuration, that converges on a TRIAD algorithm. One of the KFs is used to fuse the accelerometer data with the gyroscope data in order to estimate vertical orientation, while the other fuses the magnetometer's with the gyroscope's measurements to estimate the horizontal direction. For both of these filters, an attitude quaternion vector is produced, which serve as input for the TRIAD algorithm [95], resulting in the final orientation. The same authors developed, more recently, a magnetometer-free version of the DLKF [64]. The main difference relies on the horizontal direction estimation, which is done solely through the gyroscope's measurements integration. Both of these filters are based on previously proposed model, developed by the same authors, which include a first-order Gauss-Markov stochastic model to compensate for external accelerations that negatively influence the orientation estimation [83].

Lee et al. and Jin et al. also proposed a Dual Linear KF to separate the vertical orientation from the horizontal orientation, effectively decoupling the Yaw from the Roll/Pitch [91, 96]. The filter in [91] however, does not use magnetometer measurements to estimate the orientation in the Yaw. Specifically to this filter, in the Yaw KF, the orientation is not a state variable for estimation. For the state vector, the authors used the cosine and the sine of the Yaw angle to estimate it.

Baldi et al. [92] applied a magnetometer-free version of the filter designated as Multiplicative EKF (MEKF), described by Markley [97], in a software program (Wepose) for the attitude estimation of the upper limbs. This quaternion-based algorithm was designed to be capable of assessing the state of the accelerometer measurements: when the measured acceleration norm is close to 1.0, the algorithm assumes that the measured acceleration corresponds to the gravity acceleration. Another interesting feature regarding this algorithm is that it detects when the sensor is quasi-static, through the variation of the gyroscope data, in a time window. Hence, the correction step is done only if the variability of the accelerometer and gyroscope measurements is close to the one obtained during the static calibration phase, and if the last combination of accelerometer measurements' norm is close to 1. Furthermore, if the sensor is determined to be quasi-static, it is possible to estimate the gyroscope's bias, and remove it. This filter was benchmarked against the GDA and the Non CF (Mahony). It was observed that the proposed filter presented to be more accurate in estimating the sensor's orientation, and was also more robust to drift comparing to the other two. Moreover, the authors reported that the NCF filter "presents a remarkable Yaw drift".

Zhang et al. proposed an adaptive KF for the estimation of joint angles [98], in which the process

noise covariance matrix is the adapting variable. This filter is structurally similar to the DLKF proposed by Ligorio et al., since it is comprised of two parallel KFs, one dedicated for the fusion of the gyroscope with the magnetometer, and another for the gyroscope and accelerometer. The output of both of these filters are served as the input of a TRIAD algorithm, to estimate the sensor's orientation. This filter is complemented by a Gauss-Markov filter to compensate for disturbances in the accelerometer and magnetometer measurements.

To monitor the arms' kinematics, Peppoloni et al. developed a fusion filter model, based on an UKF due to the nonlinearities of the proposed models, that integrates the limbs' biomechanical model which is composed of 7 DOFs: 3 DOFs for the shoulder, 1 DOF for the elbow and 3 for the wrist [99]. In order to improve the accuracy of system, the filter not only estimates the orientation of the joints, but also their acceleration and velocity. The downside is that the higher number of estimated variables will increase the complexity and computational cost of the system.

An adaptive fusion filter approach, for dynamic movements, was proposed by Lee et al. [73]. For the basis of the filter, a Linear KF was used. To mitigate the effect that dynamic movements have on the accelerometer measurements, due to the reading of external accelerations, the authors proposed an accelerometer model that includes the external acceleration readings, filtered using a low pass filter, as the process noise. This low-pass filtering model for the accelerometer data was also proposed in another publication, by Luinge et al. [100].

In order to monitor the user's arm, using MIMUs, Atrsaei et al. utilized an UKF, with an embedded TRIAD algorithm to update the sensors' orientation, using orientation quaternions [88]. This filter was designed so that it could also deal with external accelerations. Since the TRIAD functions with the assumption that the accelerometer is practically only reading the gravity acceleration, to estimate the body's inclination in this case, it is rather susceptible to external accelerations. Therefore, the authors designed a threshold-based model which determines if the arm moving or static. If the first condition is true, then the TRIAD algorithm is not applied, and the orientation estimation relies solely on the gyroscope measurements. Moreover, the developed system applies a relative motion constraint, between the upper arm and the forearm, as an equation for the filter's measurement model, to mitigate the drift.

In turn, Monaco et al. used a KF to estimate the orientation of the trunk, arm and forearm of automotive, industrial workers, for ergonomic purposes [32].

One of the major downsides of the KFs is **the quantity of different parameters, leading to a more complicated and complex parameter-tuning process** [86].

2.2.2.2 Complementary Filters

Madgwick's Gradient Descent Algorithm (GDA) filter, as proposed in [84], is one of the most well-known open-source fusion filter [85]. It is greatly used as a benchmark filter, serving as a basic filter to validate new algorithms [85, 86, 92]. One of the major advantages of this filter is the **use of only one tuning parameter to define the weight of the accelerometer and magnetometer measurements in**

the orientation estimation.

Mahony et al. also developed an, open-source Explicit CF [89], by developing an observer based on the special orthogonal group (SO3). The authors applied the Lyapunov analysis to design the observer error. Moreover, the authors proposed an gyroscope bias estimation model through the integral error in the angular velocities measurements.

Wang et al. utilized the GDA to estimate the lumbar posture in competitive swimming, due to the fact that this filter is computationally lean and accessible to implement [38]. Furthermore, in the publication, the authors benchmarked the GDA against CF and EKF, concluding that the GDA had the best performance in the respective tests.

Young tested the performance of several CFs against the EKF in [101] [102]. The results led to the conclusion that CFs were not only computational less expensive, but could also have better performance when compared with the KF. The authors suggested that one of the reasons for this is that for the KF, the filter assumes the designed process model, and if that process model is imperfect, it will lead to incorrect estimations. CFs do not deal with these assumptions.

2.2.2.3 Dealing with Measurement Interferences

To mitigate the effect of the disturbances affecting the accelerometer/magnetometer on the systems' performances, two methods were reported [73]:

- Threshold-based systems;
- Adaptive-based systems.

Threshold-based approaches are grounded on the definition of a threshold value for the sensor's measurements, e.g., in the accelerometer to determine if the sensor is in a dynamic state, or in a static state. This is done by comparing the norm of the measured vector in regard to the norm determined during a pre-defined stance, during which, in the case of the accelerometer, was assumed to be measuring solely the gravity's acceleration. When the vector norm is above a certain value, in regards to the static norm, the filter will attribute more relevance to the gyroscope measurements and less to the accelerometer's. Another alternative is, for example, to evaluate the dip angle, in case of the magnetometer. If the inclination changes drastically, the system is being the affected by magnetic disturbances [81].

One of the main limitations of this strategy is the fact that the behaviour of the filter, when close to the threshold, is unstable [90]. To surpass this limitation, two thresholds can be used [103]. For example, in [103], a two-threshold, quaternion-based CF was proposed. To adapt the filter to different dynamic conditions, an error between the norm of the measured vector and the gravity acceleration is determined. If the acceleration norm is not significantly high in relation to the gravity acceleration, the accelerometer gain is maxed out. If the external acceleration is higher than the first defined threshold, then the accelerometer gain is decreased as the external acceleration increases, linearly. When the acceleration

reaches the second threshold, the acceleration gain equals to 0. The error thresholds were defined to the values: t1 = 0.1 and t2 = 0.2.

Another example for this type of approach is seen in the technical report by Fairchild [104], which gives a description of the XKF3, the XSens proprietary EKF. This proprietary filter was optimized so it could be embedded in microcontrollers.

Concerning the **model-based systems**, these systems have pre-defined acceleration disturbance and/or magnetic disturbance models, for example, through Gauss-Markov processes [81, 105]. Adaptive-based systems have pre-defined models that allow the filter to readily adapt for external disturbances in the accelerometer and/or the magnetometer. As the measurements diverge from a non-disturbed reference, less weight will be dedicated to the respective sensor measurements.

For the KFs, this can be done through pre-defined acceleration disturbance and/or magnetic disturbance models, for example, through Gauss-Markov processes, in the respective process noise matrice [81, 105]. Sabatini designed an EKF for the 3D orientation estimation of a rigid body, complemented by a gyroscope (gyro) bias model and magnetic variation model [106]. The magnetic field, in this case, was modelled by a first order Gauss-Markov process, with a white Gaussian noise component. More recently, facing the inflexibility of their KF against magnetic hard-iron disturbances, Ligorio and Sabatini [94] designed a Linear KF with the primary purpose of estimating and separating the measured noise from the useful data. Following the approach described in [83] dedicated to discard the external acceleration, the authors modelled the magnetic noise in the filter's state vector. The proposed system uses a first order Gauss-Markov process to model the magnetic disturbance as a state variable. In [98], a factor is used to model the process noise , in both KFs, in order to compensate for undefined magnetometer and accelerometer measurement disturbances, and gyroscope biases. Furthermore, an hypothesis test is used as a threshold, to detect and discard outliers in the measurements. In [107], the authors proposed an architecture of two coupled KFs, for inertial attitude estimation of a rigid body, equipped for long dynamic sessions. One of the filters is dedicated to estimate the attitude of the body. This filter includes a strategy for the detection of external acceleration in the measurements using a threshold classifier. The features used in the classifier are the mean, the variance, and the maximum value of the acceleration measurements throughout a time window. In the case of detected external acceleration, the filter adapts the measurement covariance matrix as a function of the measured acceleration magnitude, reducing the measurement weight in the estimation process. The second KF's purpose is to estimate and compensate the gyroscope bias, using the acceleration measurements.

In CFs, the gain can be adapted accordingly to the degree of disturbance. Tian et al [108] developed a CF with an adaptive gain model to direct less weight to disturbed accelerometer/magnetometer measurements in perturbed situations. The gain model was, according to the authors, also adapted to remove accumulated drift, as a consequence from the gyroscope measurements integration. To estimate the orientation of the human limbs, the authors in [86] proposed an adaptive-gain CF with a Factored Quaternion Algorithm (FQA) module. The FQA block is used to estimate an orientation quaternion when the body is in a quasi-static state, based on the accelerometer and magnetometer measurements. This

quaternion is then fused with the gyroscope measurements in the CF block. A linear function is used to compensate for disturbances in the measured acceleration and magnetic field, by comparing the deviation of the measured values from a defined reference. This function then calculates a coefficient that defines the weight of the orientation quaternion estimated by the FQA.

Nevertheless, despite the strategy used to compensate imperfect measurements, it is necessary to consider that, for example, if the acceleration measurements are rejected or are attributed a low gain during highly dynamic movements, the gyroscope bias will not be effectively corrected, leading to measurement drift [80].

2.3 Keyfindings

The SOA research focused on the analysis of the hardware and wearable configurations that the available MoCap systems use, as well as the software behind the fusion filtering and the STS calibration.

2.3.1 System's Accuracy

In Tables 2 and 3, an overview of the orientation estimation of validated inertial MoCap systems is presented. Table 2 focuses on the reported orientation error of inertial systems, for each upper-body, human joint, and for each isolated movement. In Table 3, the error is displayed in terms of the Euler angles: Roll, Pitch and Yaw.

For Table 2, it was observed that the performance of the evaluated inertial MoCap systems range between less than 2° of RMSE, to 39° RMSE, which is a significant deviation, and most likely due to not only the system itself, but also the nature of each of the test protocols. Moreover, the performance of the inertial systems seems lower for the shoulder joint, when comparing with the rest of the upper-body joints, due to the complexity of the joint.

Table 2: Human joint angle estimation errors, reported for each of the referenced publications.

Joints	DOF	Ji et al. (2019) [109] Error	X. Robert-Lachaine et al. (2019) [62] Error	R. Sers et al. (2019) [61] Error	P. Isabelle et al. (2019) [60] Error
Spine	F/E	5.97° (4.18°)	-	-	-
	Rot	2.42° (1.78°)	-	-	-
	Abd/Add	1.86° (0.91°)	-	-	-
Shoulder_R	F/E	16.00° (11.29°)	-	-	6.21° (3.90°)
	Rot	25.13° (8.62°)	-	-	6.72° (4.20°)
	Abd/Add	17.05° (7.73°)	-	3.2° (1.1°) - Slow; 2.9° (1.5°) - Fast	4.92° (3.02°)
Shoulder_L	F/E	17.51° (11.11°)	-	-	-
	Rot	20.36° (6.86°)	-	-	-
	Abd/Add	18.96° (11.34°)	-	3.2° (1.1°) - Slow; 2.9° (1.5°) - Fast	-
Elbow_R	F/E	8.14° (3.19°)	-	-	-
	Rot	-	-	-	-
	Abd/Add	-	-	-	-
Elbow_L	F/E	8.90° (4.00°)	-	-	-
	Rot	-	-	-	-
	Abd/Add	-	-	-	-
Wrist_R	F/E	15.04° (10.05°)	9.5°	-	-
	Rot	15.58° (8.22°)	8.3°	-	-
	Abd/Add	14.81° (9.23°)	9.0°	-	-
Wrist_L	F/E	14.90° (11.42°)	9.5°	-	-
	Rot	16.62° (8.27°)	8.3°	-	-
	Abd/Add	15.84° (10.03°)	9.0°	-	-
Trunk	F/E	-	-	2.3° (1.5°) - Slow; 1.6° (0.6°) - Fast	-
	Rot	-	-	2.2° (0.7°) - Slow; 2.4° (0.7°) - Fast	-
	Abd/Add	-	-	1.3° (0.7°) - Slow; 1.4° (0.9°) - Fast	-
Neck	F/E	-	-	3.7° (1.2°) - Slow; 2.7° (0.6°) - Fast	-
	Rot	-	-	2.5° (1.2°) - Slow; 1.9° (0.8°) - Fast	-
	Abd/Add	-	-	2.0° (1.1°) - Fast; 2.3° (1.2°) - Fast	-
Inertial System		Xsens Awinda	Perception Neuron	Perception Neuron	Xsens Awinda
Ground Truth		Cortex	17 Optotrak (Northern Digital, Canada) clusters	12 Vicon cameras (Vicon Motion Systems Ltd., Oxford, UK)	9 Vicon MX cameras (seven MT40-S and two MT10- S cameras)
Nº of Participants		20	5 healthy adults	8 healthy individuals (5 male & 3 female)	16 healthy participants (eight males)
Environment		Laboratorial ->simulating industrial assembly line	Laboratorial	Laboratorial	Laboratorial
Interferences		Presence of Metal components	Magnetic disturbances avoided	-	-
Tasks		Automotive assembly line tasks	Moving empty boxes	Isolated joints movements	Isolated shoulder & trunk movements
nº of trials & duration		6 tasks / >10 s & <60 s	≈ 32 minutes	2 trials per movement / <10 s	5 trials per movement
Error metric		RMSE angles (Standard Deviation (SD))	RMSE angles	RMSE angles (SD)	RMSE angles (SD) / only the simple tasks were recorded here

Joints	DOF	M. A. Wirth et al. (2019) [110] Error	S. Sara et al. (2020) [22, 111] Error	Morrow et al. (2017) [112] Error	Esfahani et al. (2018) [66] Error
Spine	F/E	-	-	-	-
	Rot	-	-	-	-
	Abd/Add	-	-	-	-
Shoulder_R	F/E	-	16° (Flexion) - 19° (Extension)	-	Max. - 3.53° / Min. - 2.09°
	Rot	-	-	-	Max. - 3.86° / Min. -2.89°
	Abd/Add	-	23° (Abduction) - 14° (Adduction)	6.8° (2.7°)	Max. - 3.74° / Min. - 1.75°
Shoulder_L	F/E	-	-	-	-
	Rot	-	-	-	-
	Abd/Add	-	-	-	-
Elbow_R	F/E	-	34° (Flexion) - 23° (Extension)	8.2° (2.8°)	-
	Rot	-	-	-	-
	Abd/Add	-	-	-	-
Elbow_L	F/E	-	-	-	-
	Rot	-	-	-	-
	Abd/Add	-	-	-	-
Wrist_R	F/E	10.47° ± 4.22°	39° (Flexion) - 38° (Extension)	-	-
	Rot	-	-	-	-
	Abd/Add	2.42° ± 1.19°	14° (Radial dev.) - 18° (Ulnar dev.)	-	-
Wrist_L	F/E	-	-	-	-
	Rot	-	-	-	-
	Abd/Add	-	-	-	-
Trunk	F/E	-	21° (Flexion) - 8° (Extension)	1.6° (1.1°)	-
	Rot	-	-	-	-
	Abd/Add	-	6°	-	-
Neck	F/E	-	-	2.9° (0.9°)	-
	Rot	-	-	-	-
	Abd/Add	-	-	-	-
Inertial System		2 DyCare (DyCare® Lynx, Barcelona, Spain) IMUs	Proposed System - Fusion filter: Quaternion CF (QFC)	6 sensors (OpalTM, APDM, Inc., Portland, OR USA)	2 Custom Imus
Ground Truth		11 Vicon MX3+ and Vicon MX3 cameras	10 Vicon camera setup	10 camera, Raptor 12 Digital RealTime (Motion Analysis Corp., USA)	8 camera Vicon system
Nº of Participants		10 healthy participants (5 male)	14 healthy participants (9 men and 5 women)	6 surgical faculty members (3 male)	1 subject
Environment		Laboratorial	Laboratorial	-	-
Interferences		-	-	-	-
Tasks		wrist radial-ulnar & flexion extension movements - Full ROM	Only Static tests were considered - Isolated movements	Surgical task - minimally invasive laparoscopy	Static, isolated joint movements - upper limb
nº of trials & duration		5 trials per movement	-	-	-
Error metric		Mean Absolute Difference (MAD)	RMSE angles (SD) / only the laboratorial validation and QFC was assessed here	RMSE angles (SD)	RMSE angles (SD)

Table 3: Angle estimation errors (RMSE), reported for each of the referenced publications, for the Roll, Pitch and Yaw orientation.

Reference	Ground truth	Error (RMSE)			Observations
		Roll	Pitch	Yaw	
[113]	Manipulator with an absolute encoder	0.85°	1.14°	1.41	Fusion Filter: Digital Motion Processor (DMP) (Invensense)
[113]	Manipulator with an absolute encoder	0.75°	0.83°	1.32°	Fusion Filter: Partial DMP (Invensense) + CF + GDA
[113]	Manipulator with an absolute encoder	0.93°	1.22°	1.30-4.63°	Fusion Filter Partial DMP (Invensense) + CF + Mahony Filter
[66]	Controlled turn and tilt table	0.613° ± 0.133°	1.646° ± 0.195°	2.750° ± 1.619°	Calibration of the IMU - turn and tilt table. Angular velocity: 150 °/s
[93]	Oqus 6+	1.0953°	1.4176°	1.9574°	Human user. Upper arm. No joint angle constraint model.
[91]	Optitrack Flex 13	3.98°	1.45°	1.48°	Only results from the test 4. Fusion Filter: Constrainted Augmented KF
[114]	Vicon	2.6716°	1.4824°	1.2609°	Only the squatting test. Human participants.
[115]	MTx (IMU)	0.1° (min.) - 1.62° (max.)	0.12° (min.) - 0.80° (max.)	0.33° (min.) - 6.06° (max.)	Only the best and worst test results were displayed. / Fusion Filter: EKF
[116]	da Vinci surgical robot system (Intuitive Surgical, Inc., Sunnyvale, USA)	0.96°	0.76°	1.06°	Only the best and worst test results were displayed. Fusion Filter: EKF
[92]	10 Bonita cameras (Vicon)	1.10° ± 1.30°	1.46° ± 1.71°	1.35° ± 1.62°	Dynamic test - platform randomly rotating in space. 100 Hz sampling test was selected. Fusion Filter: Proposed Multiplicative EKF (MEKF)
[92]	10 Bonita cameras (Vicon)	1.38° ± 1.37°	2.28° ± 2.43°	2.11° ± 2.24°	Dynamic test - platform randomly rotating in space. Only the 100 Hz sampling test was selected. Fusion Filter: GDA
[92]	10 Bonita cameras (Vicon)	2.23° ± 2.25°	2.70° ± 2.90°	2.42° ± 2.62°	Dynamic test - platform randomly rotating in space. Only the 100 Hz sampling test was selected. Fusion Filter: Non-Linear CF

As stated, it is necessary to consider that the different tests were executed in different conditions regarding: number of trials, trial duration, environmental interferences, number of participants, ground truth, tasks, among others. These factors significantly influence the overall result of the system, which makes it impossible to perform a benchmark between inertial MoCap systems. For example, the inertial systems have lower validity for more complex movements, as stated by Poitras et al. [59]. Furthermore, the lack of standardization in validation protocols, makes it hard to determine the factors that contribute the most to the orientation estimation errors [59].

Regarding Table 3, it is possible to observe that, as demonstrated in Table 2, the different validation experiments are not standardized, leading to the impossibility of performing a reliable benchmark. In contrast, the differences in results, as the overall error is smaller. This could be justified by the fact that there was a low number of participants in these studies, leading to more controlled experiments. Even the studies that included participants, only had one volunteer, leading to low variability in the data.

2.3.2 Wearable's Hardware

In Table 4, a general overview of various analyzed inertial systems is shown.

In most of the reviewed studies (Table 4), the authors reported the use of commercial systems, or IMUs (e.g. the MTw IMU series from Xsens), which present a significant cost for the system. For the commercial type of IMUs, the Xsens Awinda system, or the MTx line of IMUs, were the most reported inertial sensing system in the literature.

Outside of these commercial alternatives, other low-cost IMUs available on the market were also utilized (e.g MPU series IMUs from Invensense), in a lower frequency in regard to the commercial systems however. The MPU series IMUs were the most used type of IMUs, outside of the commercial ones.

Lastly, in some other studies, fully homemade inertial units were described and used. Caputo et al. [117], for example, developed an inertial sensor unit using the MPU-6050 - accelerometer and gyroscope - the HMC5883L - magnetometer - and an STM32F103 as the processing unit.

In one publication [118], the authors compared the orientation estimation accuracy between three IMUs: the MTw Awinda IMU from Xsens, the MPU-9250 from Invensense and the MetaMotionR IMU (MBIENTLAB, CA, USA). The tests were executed in a robotic arm, and in two different trials. In one trial, the IMUs used their proprietary filter to estimate the orientation, in which the MPU didnt't take part. In the second trial, the IMUs used the Madgwick's GDA to estimate the orientation. In the first test, the MTw was he most accurate system. In contrast, in the second test, the MMR proved to have the best performance ($1.04° \pm 0.49°$), with the MPU being the worst of the three ($1.44° \pm 0.62°$). The price of the MMR presents a cost of up to 80.99 € per unit [119]. In contrast, the MPU-9250 IMU's monetary value rounds the 15 $, as its a lower-cost alternative.

In [120], a benchmark between 3 sensors, of different categories, was made. Two of the sensors were commercially available - FMT1030 (Fairchild Semiconductors, Virginia, USA) and the Xsens MTi-1 [121] -

with the other being custom-made [122]. The FMT1030, which was discontinued, was the selected IMU, following its superior performance in comparison with the other alternatives.

In terms of the available sensors, a substantial amount of the revised systems integrated commercial IMUs, which contribute to the **rise in cost of the system**. Therefore, since the focus is the **development of a low-cost, inertial MoCap system, lower-budget sensors like the MPU-9250**, which were also prevalent in the reviewed studies, **were considered for the wearable**. If better **low-budget alternatives are identified, they will be integrated instead of the MPU-9250**.

2.3.2.1 Wireless Communication Protocols

For the communication between the acquisition system and the processing unit, or a main station, different wireless communication protocols were reported in the studies. The most prevalent ones were based on WiFi or Bluetooth (Bluetooth Low Energy included).

Some other wireless alternatives were also reported. The XSens Awinda system, in contrast to the WiFi protocol used in the XSens Link, utilizes an IEEE 802.15.4 - 2.4 GHz [123]. This communication standard is more associated with lower bit-rate, low consumption applications [124].

Some systems, although to a lesser extent, use wired protocols to establish this type of communication. Such examples can be seen in [66, 69].

Furthermore, the use of memory cards, which can be utilized for offline acquisitions, was also reported in some studies [41, 125].

In terms of sampling rate, the frequency is concentrated around the 100 Hz, which goes in accordance to the publication [126]. Some systems made use of less sampling frequency.

In this project, the data acquired by the IMUs will be sent to a processing station, wirelessly. To do that, a WiFi or Bluetooth communication protocol will be established between the portable processing unit and the main station, as they are the standard wireless communication protocols.

Table 4: General overview of the reviewed publications. Information discriminated in: N.º of sensors, sensors used, sensor placement, degrees of freedom, sampling frequency, data trasnmission protocol, calibration sequence, fusion filter/software used.

Reference	Nº of sensors	Sensor	Sensor Positioning	DOF	Sampling Frequency	Data Transmission	Calibration	Fusion Filter / Extra Software
[70]	15	TEA CAPTIV T-Sens Motion	Neck, Upper body (back), Upper Extremities, Shoulders, Elbows, Wrists, Lower Extremities, Hips, Knees, Ankles	34	32 Hz-128 Hz	-	N-pose/Camera-Laser-Mirror custom setup	-
[33]	50	Nansense Sensor suit	Torso, Shoulders, Forearms, Wrists	24	-	-	-	Proprietary software (Nansense)
[109]	17	Xsens MVN Awinda IMU	Spine, Shoulders, Wrists, Right/Left hip, Elbows, Knees & Ankles	27	60 Hz	IEEE 802.15.4 - 2.4 GHz	N-pose + walk	Xsens KF-3
[117]	10	MPU-6050 (accelerometer (acc) & gyro) + HMC5883L (magnetometer (mag))	Pelvis, Trunk, Right (Left) arm, Right (Left) forearm, [Right (Left) Upper leg and Right (Left) Lowerleg]	18	-	-	-	EKF
[21]	17	Xsens MVN	Head, Sternum, Shoulder blades, Upper arms, Lower arms, Hands, Pelvis, Upper legs, Lower legs, Feet	-	240 Hz	WiFi	N-pose/walk back and forth following the MVN Analyze software guide	Xsens KF-3
[21]	11	MPU-9250	Upper arms, Lower arms, Upper legs, Lower legs, Pelvis, Head, T1 vertebra	-	100 Hz	WiFi	N-pose/Joining hands	**UKF**
[21]	17	Perception Neuron Sensor Suit	Head, Sternum, Shoulder blades, Upper arms, Lower arms, Hands, Pelvis, Upper legs, Lower legs, Feet	-	120 Hz	WiFi	Steady pose/ A-pose/ T-pose/ S-pose	Propietary software (Axis Neuron)
[96]	1 - Tested	IMU based on a MSP430. AXL345 (tri-axis accelerometer), HMC5883 (AMR sensor), L3G4200 (tri-axis angular rate gyroscope).	-	-	35 Hz	RF	-	Two-step KF
[64]	4	MPU-9250	Trunk, Right Upper arm, Right Forearm & Right Hand	6	100 Hz	-	N-pose/ 90° flexion in the sagittal plane	Dual Linear KF + TRIAD
[127]	13	Xsens MVN Awinda	Whole body	-	-	WiFi	N-pose + walk	Xsens KF-3
[61]	18	Perception neuron	Head, Thorax, Pelvis, Shoulders & Upper arms	-	120 Hz	Perception neuron software	Steady pose - User was sat down at a desk with palms face down on the table + T pose + Standing A pose + S pose	Proprietary software (Axis Neuron)
[62]	17	Perception neuron	Feet, Shanks, Thighs, Pelvis, Sternum, Head, Scapulae, Upper arms, Forearms & Hands	-	120 Hz	Perception neuron software	Steady pose/ A pose/ T pose/ S pose	Proprietary Software (Axis Neuron)
[32]	5	Custom micro IMUs: MPU-6050 (acc and gyro), HMC5883L (mag)	Trunk, Arms, Forearms	-	-	-	-	KF

Reference	Nº of sensors	Sensor	Sensor Positioning	DOF	Sampling Frequency	Data Transmission	Calibration	Fusion Filter / Extra Software
[60]	9	MVN Awinda system, Xsens	Head, Shoulder (2), Sternum, Upper arm (2), Forearm (2) and Pelvis	-	60 Hz	IEEE 802.15.4 - 2.4 GHz	N-pose	Xsens KF-3
[66]	18 (2 for testing)	gyro (InvenSense Inc., San Jose, USA), acc (Analog Devices Inc., Norwood, USA), mag (Honeywell Inc., Morris Plains, USA)	Head, Shoulders, Back, Trunk, Thighs, Legs, Feet, Arms, Forearms, Hands	-	100 Hz	RS485 protocol	N-pose + Upper limbs Functional Calibration	Adaptive EKF
[113]	13	MPU 9250	-	-	50-120-135 Hz	WiFi	-	DMP (Invensense) / DMP+CF/DMP+CF with Mahony / Kalman-based CF + DMP
[45]	2 IMUs (1 potentiometer)	UM7-LT Orientation Sensor	Shoulder & Wrist joints	7	100 Hz	USB	T-pose	GDA + Zero-Velocity Update
[69]	2 IMUs (2 flex sensors)	-	Hand & Arm.	6	-	Serial Port	-	CF
[46]	15	MPU-9250	-	-	-	-	-	UKF
[114]	16	MTx sensors	-	-	100 Hz	-	-	Complementary KF
[35]	4	Xsens MTx sensors	Hand, Forearm, Arm and Back	-	50 Hz	Bluetooth or USB	N-pose	-
[22, 111]	4	IoTiP (Fraunhofer AICOS, Porto, Portugal)	Hand, Forearm, Arm, Torso	8	100 Hz	Bluetooth	N-pose + T-pose	Quaternion CF + Algebraic algorithm
[120]	18	FMT1030	Feet, Legs, Thighs, Pelvis, Trunk, Shoulders, Neck, Head, Upper Arms, Forearms and Hands	-	100 Hz	WiFi	T-pose or N-pose	Nonlinear CF / EKF / Adaptive EKF/
[128]	17 - full suit	Xsens MVN sensors	pelvis, upper legs, and upper arms	-	240 Hz	WiFi	N-pose	Xsens KF-3 + Artificial Neural Network (ANN) / Nearest Neighbor Search (NNS)
[129]	10	MPU-9250	Head, trunk, shoulders, upper arms, forearms, lower limbs	-	-	RF 2.4 GHz ISM	-	DMP (Invensense)
[88]	2	Xsens Mtx sensors	Forearm, Upper arm	-	100 Hz	-	Arm beside the body with the palm of the hand facing forward	Quaternion UKF
[93]	2 (used for testing)	Xsens Mti-3 sensors	Upper limb	-	-	RF 2.4 GHz	T-pose	Second Estimator of the Optimal Quaternion (ESOQ-2) + Linear KF + Joint Angle Constraint Method
[40]	4	ViMove (Dorsavi©, Australia) sensors	Occiput, T3 level, between the posterior superior iliac spines, over the T12 vertebra	-	100 Hz	Bluetooth	ViMove system's software	ViMove system's software
[110]	2	Lynx (Dycare®) sensors	Right, dorsal forearm, proximal to the wrist, and on the right hand	-	102.4 Hz	Bluetooth	Neutral position	Lynx (Dycare®) software
[30]	20	MPU9250	Hand (including fingers) and Forearm	-	200 Hz	-	-	EKF

Reference	Nº of sensors	Sensor	Sensor Positioning	DOF	Sampling Frequency	Data Transmission	Calibration	Fusion Filter / Extra Software
[38]	4	ADIS16448	Lumbar spine, Wrist & Ankle	-	200 Hz (400 Hz máx.)	Flash memory; RF 2.4 GHz	-	GDA
[47]	17	MPU-6050	Head, Trunk, Pelvis & Upper/Lower extremities	-	100 Hz	Bluetooth Low Energy	-	Mahony Filter
[42]	3	MPU-9150	Upper limbs	7	-	WiFi	-	CF
[125]	Not specified	MPU-9255	Not specified	-	-	WiFi/128 GB micro SD card	-	GDA
[36]	17	MVN Awinda	Full body setup	-	-	RF 2.4 GHz	N-pose + Walking sequence (Awinda calibration protocol)	Xsens KF-3
[130]	2	Custom sensor - 3-axis acc (LIS3LV02D) + 3-axis mag(HMC5843) + 3-axis gyro (ITG3200)	Upper arm & Forearm	-	-	-	-	Adaptive-gain CF
[31]	17	Xsens MVN Awinda / Perception neuron sensors	Full body suits	-	125 Hz	-	N-pose + Walking sequence (Awinda calibration protocol) / Perception Neuron calibration sequence (N-pose + T-pose + S-pose)	Xsens KF-3 / Proprietary software (Perception Neuron)
[131]	-	Razor IMU - gyroscope: (ITG-3200) + accelerometer: (ADL345) + magnetometer (HMC5883L))	Variable	-	240 Hz	Bluetooth	-	IMOTECH software
[34]	31	Synertial (UK)	Full body suit including Hands	-	-	WiFi	-	Synertial Fusion Filter
[15]	7 + 2 goniometers	CAPTIV Motion IMUs (TEA, Nancy, France)	Upper arms, Forearms, Head, Trunk (chest), Pelvis (sacrum)	20	64 Hz	-	Neutral position	EKF
[132]	2	XSens MTw sensors	Upper arm & Forearm	-	75 Hz	-	-	-
[133]	Tested	Opal version 2 sensors (OpalTM, APDM Inc., Portland, Oregon)	Tested	-	128 Hz	RF 2.4 GHz, ultra low power	-	KF
[112]	6	Opal sensors	Base of the back of the Head, Anterior sternum & lateral aspect of the bilateral Upper-arms & Forearms	-	80 Hz	RF 2.4 GHz, ultra low power	Arms down, thumbs forward	KF
[134]	-	MPU3050, 3-axis gyro + LSM303DLH, 3-axis acc & mag	Head, Upper arms, Forearms, Thighs, Calfs - Not specified	-	-	RF 2.4 GHz	-	EKF
[41]	2	ViMove sensors	Sensors were attached at spinal levels T12 and S2	-	19.6 Hz (full range 19.0–19.8 Hz).	RF 2.4 GHz, Flash memory	N-pose	-

Reference	Nº of sensors	Sensor	Sensor Positioning	DOF	Sampling Frequency	Data Transmission	Calibration	Fusion Filter / Extra Software
[135]	17 in total	Synertial IGS-180	Wrists, Forearms, Upper arms and Shoulders	-	60 Hz	-	-	Fusion Algorithm (Inertial Labs Inc., Virginia, USA)
[39]	Varied	MPU-9250	Versatile	Versatile	7 Hz	USB cable	-	-
[39]	Varied	ST iNemo-M1	Versatile	Versatile	25 Hz	WiFi	-	-
[136]	2	Data-logging 3-Space™ Sensor (Yei Technology Inc.)	Trunk (T6) and Pelvis (L5/S1)	-	100 Hz	MicroSD card or USB	T-pose	-
[71]	1 - Tested	MPU-6050	Back side of the arm centered with elbow-marker - Tested	-	100 Hz	USB port	N-pose	Customized Complementary Algorithm
[63]	15	BNO055	Upper arms, Forearms, Hands, Upper legs, Lower legs, Feet, Shoulders' gridle, Lower and Upper spine, Pelvis	-	up to 320.4 Hz (25 in the tests)	Bluetooth Low Energy	Pose-based calibration, while facing the North	KF (BNO055 embedded algorithm)

2.3.3 Sensor-to-Segment Calibration

The different types of STS calibration methods reviewed from the literature are: manual calibration, static calibration, functional calibration and anatomical calibration. Each method has its own advantages and disadvantages.

Through Table 4, it is possible to observe that the most reported type of STS calibration sequence were comprised of static postures. This was expected since these type of sequences are **more convenient for the user**, who needs to only execute **simple, static, postures during a short period of time to estimate the misalignment between the sensor frame and the segments'**. The same can be observed in Table 1, for the commercial systems whose calibration sequence were found, except for the XSens systems, which have their own standard sequence, which is comprised of a static pose (N-pose and T-pose), followed by a walking sequence. The high prevalence of static calibration sequences can be explained due to it's **simplicity, quickness and it's easy to perform**, as it is based on the execution of simple and convenient static poses.

Overall, for a day-to-day motion capture system, there needs to be a **compromise between the accuracy of the calibration sequence, with its accessibility and quickness to perform by the user** [76]. Anatomical calibration requires a **subject, with knowledge about anatomical landmarks, and specialized instruments to be applied, which makes it difficult to be applied on a day-to-day basis**. This type of calibration sequence seems more driven towards clinical applications, with an examiner responsible for the positioning of the sensors, eliminating the need for the subject to perform certain poses and movements which might be difficult to execute due to possible constraints [74]. The main advantage of this calibration sequence is the fact that it does **not require extra computational load** [75].

It was reported that there is a big discrepancy in performance between the use or the non-use of a STS calibration. But, that discrepancy is small when comparing different calibration sequences [75]. In the specific case of Bouvier et al. [75], it was observed that the static calibrations sequences obtained similar results with the functional calibration sequences. In the same study however, it was concluded that the manual calibration achieved poorer results, namely on the shoulder and elbow joints. Moreover, manual calibration sequences present significant limitations, e.g., **the presence of surface irregularities of the human body present a problem for the manual alignment of the IMU**. These can be the result of, for example, muscle presence or other deformities [74]. Furthermore, this method seems less convenient for day-to-day applications, as a **detailed positioning and adjustment of the sensor needs to by done before starting a motion aquiring session** [64, 75, 137].

For these reasons, an **algorithm-based calibration sequence was deemed necessary for the improvement of the system's accuracy.**

In terms of the static and functional calibration, there are conflicting results when comparing both in terms of performance, with neither being recognized as the best method [74, 75, 138, 139].

For the functional calibration in particular, its use may be compromised in joints with more DOFs, since

they are more difficult to perform one-dimensional rotations [74, 75]. Moreover, functional calibration sequences can be exhaustive if they are comprised of various individual movements. Alternatively, a combination of one or more static poses with functional movements to optimize the calibration in specific joints can be applied [75, 138].

An overview of some considerations for each of the reported STS calibration types is described in Table 5

Table 5: Overview of the different STS calibration methods.

Calibration strategy	**Considerations**	**Notes**
Manual	- No computational load - Human body presents irregular surfaces - affecting the quality of the positioning - Needs a subject to accurately position the sensors.	Manually align the sensor orientation with the anatomic orientation
Static	- Extra computational weight - User-convenient - quick and easy to execute - Isn't as dependable to the sensor placement	Based on static poses
Functional	- Can only define a single axis for a single segment, for each movement - Difficulty in applying for certain segments like the trunk - Difficult to perform in joints with more than 1 DOF - Extra computational weight	Uni-axial and uni-joint movements / Is not as dependable to the sensor placement / Can be combined with static postures
Anatomic	- No computational weight - Needs specialized measuring devices - Needs a subject with anatomical knowledge for the sensor positioning	Technical location of anatomical landmarks

Therefore, For the **STS calibration**, it was concluded that manual calibration procedures are less accurate then the alternatives, being discarded for this project. For the other calibration algorithms, there seems to be conflicting evidence regarding about which has the best or worst performance. Therefore, and also because the static calibration procedures presents less computational load and is more easy

to implement and perform by the user, this was the considered the most attractive STS routine for this project.

2.3.4 Fusion filters

The orientation estimation in inertial systems is done through the fusion of the different sensors present in the in the inertial unit. This is done so that the different sensors nullify each others' limitations.

From the information displayed in Table 4, it is possible to observe that the KF was the most prevalent fusion filter class reported in the reviewed literature. This is also reflected from the fact that the Xsens MVN MoCap systems were the most used, which applies a proprietary EKF - XKF-3 [104, 123].

The Mahony filter, although well-known, was reported as having **poorer performance** when compared with the GDA filter [92, 107] in benchmarking tests. In [92], the Mahony filter appeared to **suffer immensely from Yaw drift**, moreso than the GDA.

The ECF is the newest filter developed by Madgwick et al. [85]. It is based on the design of the classic CF. Due to this, it has a very low computational weight when compared with the KF, **being more adequate for lower power processors.** Furthermore, this filter is being used in a commercial line of inertial sensors, developed by X-io Technologies (X-io Technologies, Bristol, UK). This filter presents a threshold-based strategy to reject magnetometer measurements in case a magnetic disturbance is detected. The ECF was validated against the previous filter designed by the same author - the GDA - using a virtual IMU. The ECF showed to have a faster convergence time - 68 % faster on average. Furthermore, it has a very important advantage regarding its predecessor: **contrary the GDA filter, it decoupled the Yaw angle from the Roll and Pitch orientations. Therefore, magnetic disturbances do not affect the horizontal orientations.** Still regarding the ECF, in the benchmark study made by B. Fan et al. [81], it was observed that, between the selected filters, the DLKF by Ligorio et al. and the ECF had the best performance in terms of static and dynamic accuracy, without magnetic disturbances. Moreover, it was also observed that in the presence of magnetic disturbances, the ECF6 had the best performance in orientation estimation, primarily due to the fact that it didn't employ the magnetometer's measurements, and relied solely on the gyroscope for the estimation in the Yaw angle.

The prospect of having a fusion filter that combines a good orientation estimating performance with a low computational weight, as it was developed to be embedded in the hardware [85], makes this filter an interesting option for the project.

In regard to the studied fusion filters, an overview, considering their main advantages and disadvantages, is described in Table 6.

For the fusion filter (Table 6), since the system needs to be able to operate in real-time, the processing load of the algorithm needs to be considered. The filter must not be a bottleneck point for the system. In this context, the ECF was considered the best filter for this project, to the best of the author's knowledge. It is overall more efficient than the analyzed KFs, and it was also benchmarked against the GDA and a KF, obtaining better results in performance. Also, the filter is capable of decoupling the Yaw from the Pitch

Table 6: General overview of the most prevalent fusion filter methods, with the inclusion of the ECF.

Class	Subclass	Considerations
Kalman Filter	Linear KF	- More efficient then the EKF and UKF - Not adapted to non-linear problems
	EKF	- Most common in non-linear applications
	UKF	- Alternative to the EKF in non-linear problems - More robust during initialization - Less efficient than the EKF
Complementary Filter	GDA	- Contains only one tuning parameter for acc & mag: 1) Simple to implement; 2) Lack of tuning optimization - Pitch and Roll not decoupled from Yaw; - Used as basis for improvements; - Prevalent use as a benchmark filter; - Computationally efficient.
	Mahony	- Computationally efficient
	ECF	- Pitch and Roll are decoupled from Yaw; - Fast initialization convergence; - Integrated with a magnetometer disturbance rejection method (threshold) - Computationally efficient

and Roll, which the GDA cannot do. Moreover, as a guarantee that this filter is computationally efficient, the authors claimed [85] that the ECF was developed to integrate embedded systems. Lastly, the ECF is easier to implement than the analyzed KFs, as it does not present a process noise or measurement noise matrix that needs to be defined and calibrated with the system.

2.3.5 Wearable's Garment

Lastly, for the wearable's garment, more attention was addressed towards the commercial MoCap systems. **It was concluded that a strategy capable of covering the hardware needs to be addressed for the garment, to improve it in aesthetic terms**. Furthermore, **the suit itself will need to be tight-fitted, to improve the fixing of the sensors in regard to the user's body, and avoid the suit from sliding.** Moreover, for the connectors, several systems integrate them in the sensor casings. This can lead to problems concerning the orientation of the sensors, due to the fact that the connectors are rigid elements, and the force applied to the cables provides pressure to the sensor modules. Therefore, the XSens Link and Rokoko strategies were considered, in which the connection

is not present in the sensor modules, but on the anatomical segment. This way, **the sensor casings have freedom of movement in regard to the connectors.** Lastly, in terms of the placement of the heaviest units in the wearable - power supply and processing unit - it was seen, in the case of the XSens Link and the Rokoko Smarsuit Pro, that they were placed on the spine area, or close to the waist. **This makes their weight less perceived by the wearer, due to being close to the user's center of mass.**

3

Design Conceptualization

This chapter focuses on the description of the proposed solution, whose fundamentation is based on the SOA, and in compliance with the respective project requirements. Furthermore, it discusses the solution conceptualization, based on a user-centred design.

3.0.1 Ergowear Framework Description

The previous version of the Ergowear is described, in detail, in [29]. The Ergowear is also illustrated in Fig. 15.

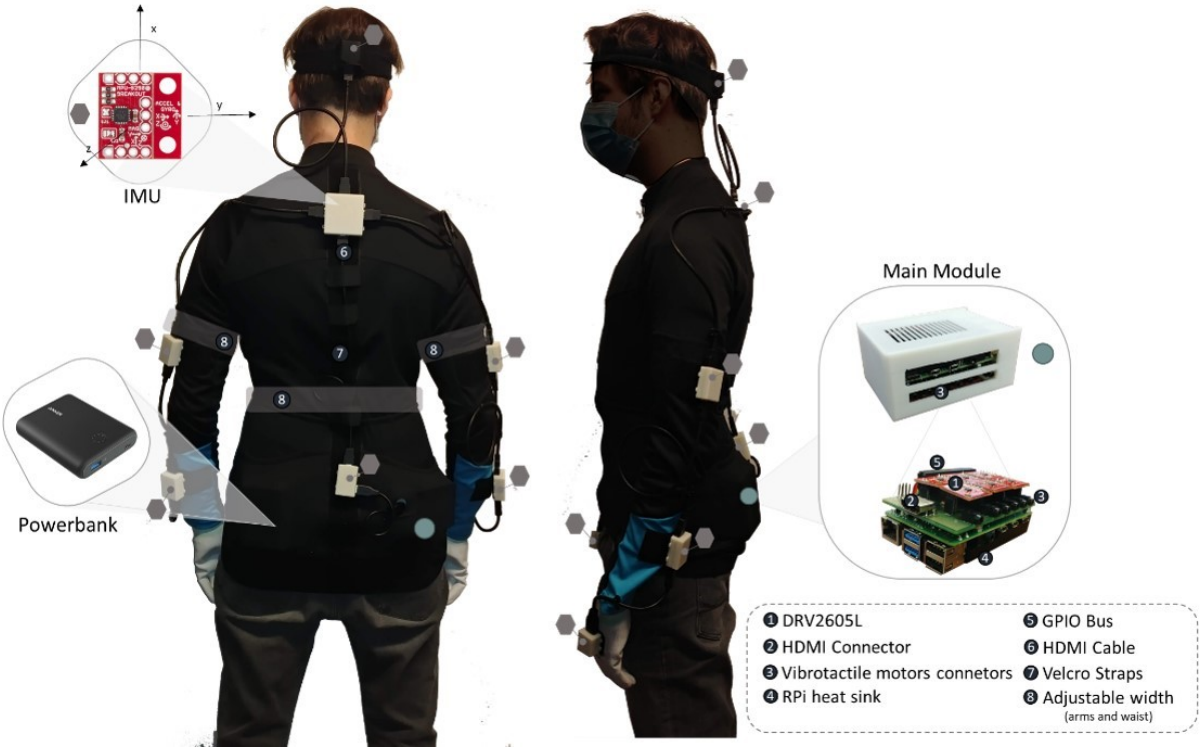

Figure 15: Previous version of the Ergowear overview, as shown in [29].

Firstly, to identify the limitations of the previous system, a test protocol was developed, in which participants would perform a number of different tasks with the previous Ergowear.

3.0.1.1 Test Protocol

21 volunteers (15 males and 6 females; 66.0 ± 7.8 kg; 171 ± 8.6 cm) participated in a data acquiring session whilst using the system from the previous iteration. This protocol was designed with two sub-protocols in consideration: a dynamic testing protocol and a static testing protocol. In both types of testing protocols, the XSens Awinda system was used as **ground truth**, being worn at the same time as the Ergowear system.

The former is composed by several trials in which the subject performs normal day-to-day tasks. This type of testing was more dedicated to acquire data to train neural networks, but was also used to detect limitations regarding the usability and general robustness of the system.

The latter is based on the subject being in a static pose, and performing uni-axial movements, for each upper body joint, at two different speeds - slow and fast. The slow speed corresponds to 23 Beats per Minute (BPM), whilst the fast speed is 45 BPM. To mark the beat, a metronometer cue was used, with the selected speed configured. Each movement was executed with the full ROM of the dynamic joint. Each movement was repeated 6 times - 3 in slow speed and 3 in fast speed. The analyzed joints, and respective movements, were: **the shoulder flexion/extension and abduction/adduction; elbow flexion/extension and pronation/supination; wrist flexion/extension, radial/ulnar deviation and rotation (both directions); trunk flexion/extension, side bend (both sides) and rotation (both sides); neck flexion/extension, side bend (both sides) and rotation (both sides).** A total of **42 movements** were registered for each participant.

3.0.1.2 What Could be Improved

During the execution of tests, in which a variety of people used the previous wearable system and performed different tasks, some limitations regarding the wearable and its hardware were noted.

Firstly, it was observed that the HDMI cables (including the connectors), used to connect the sensor modules, were too heavy and rigid, altering the orientation of the modules, which would diminish the accuracy of the system. To mitigate this effect, **more freedom of movement for the connectors, in regard to the sensor modules, needed to be secured.** So, it was established that **the connection between modules would be performed on the middle of the anatomical segments**, and not in the sensor modules. Adding to this, the wearable fixed the sensors through velcro patches sewn onto the tissue. These didn't offer much structural support, leading to the sensors' freedom of movement. Therefore, **new attachments that offered more structural support were analyzed, like external straps or compressive pockets.** These limitations can be observed in Fig. 16.

This led to the sensors not tracking the joint's accurately. Moreover, it is relevant to add that if there is space between the skin and the textile, the vibrotactile actuators will not be felt by the user. To correct this,

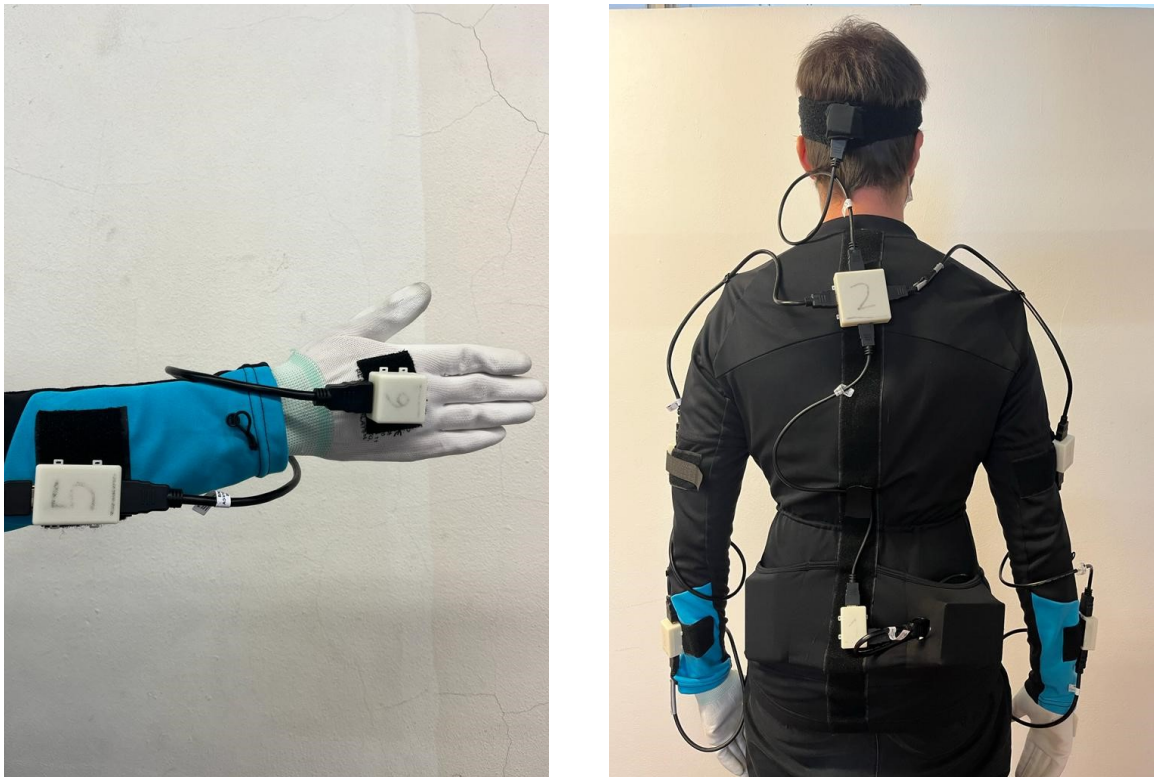

(a) (b)

Figure 16: Misalignment between the a) hand sensor and the forearm sensor, and b) on the back.

during the tests, tape was used to guarantee that the sensor modules would be fixed, which had relative success. Fig. 17 illustrates this problem. Furthermore, when the user performed certain motions, the jacket would slide in regard to the trunk, or the arm, depending on the motion. For example, when the user stretched the arm, the sleeve would not accompany the segment, altering the position of the sensors. To correct this, **fingerless gloves were considered for the sleeves of the new garment, to anchor these sleeves onto the user's arm, avoiding any slipping**. The same solution was defined for the trunk, with the addition of shorts, transforming the jacket into a bodysuit. Furthermore, to add to this solution, a tightly-fitted suit was considered necessary to help fix the sensors, and making sure the biofeedback system can be felt by the user.

Also, the previous iteration accumulated a lot of heat during the sessions. This was mainly due to the fact that the garment was made of a thermal cyclist jacket, which didn't allow much heat dissipation, as well as the processing unit (Raspberry Pi 4) heating up considerably during the data acquisition sessions. In regard to the textile, **it was decided to use breathable fabric which allowed heat dissipation**. For the processing unit, according to the description of the previous version in [29], it is possible to extrapolate from the autonomy tests that the system has a base consumption of 1827,27 mA, which is considerable. The Raspberry Pi 4 (RPi4) alone consumes up to 1200 mA, and an average of 600 mA. This led to the selection of a new low-level processing unit, which could be more efficient for the proposed tasks. Still regarding the processing unit, the RPi4 limits for the maximum sampling frequency were tested. The

Figure 17: Adhesive tape used to fix the sensor modules onto the respective anatomical segment.

obtained result showcased that the new RPi4 was limited to a maximum sampling frequency of around 100 Hz. One of the main features the new iteration will be equipped with is the Strap-Down Integration (SDI) block, which is dependant on higher sampling frequencies of the gyroscope. With a limit of around 100 Hz, the RPi4 is not able to acquire the data fast enough to perform the SDI, being another reason to change the low-level processor.

Regarding the headband, user's complained about it's heat accumulation, as well as the fact that it was too compressive, causing discomfort. A new headband was designed, in which these limitations were tackled.

Furthermore, it was observed that the sensors placed on the forearms were directly positioned on top of muscle tissue. This leads to complications related to muscle movements, which translate in misalignments of the sensors, and low frequency noise. To correct that, **the placement of these sensors was altered to be on top of the bony landmark, immediately before the wrist joint.**

The sensor casings were also deemed possible to miniaturize, which would positively affect the system in terms of wearability (sizing and attractiveness). The main reason for this was the use of extra PCBs to include the connectors for each of the sensors. Moreover, it was considered that the wearable could improve in terms of attractiveness. One of the reasons for the lack of aesthetic standards of the suit is the

exposure of the wearable's electronics, which, in commercial products, is covered inside external layers of textile and accessible using zippers.

3.1 Design Concerns

When designing an inertial wearable MoCap system, it is required to address, along with its technical specifications, two major concepts: usability and wearability. This prerequisite arises from the fact that even the most precise system will be rapidly abandoned by the user if it does not fulfill the usability and wearability requirements that are imperative to make the user feel satisfied and happy to wear the system.

3.1.1 Usability

According to the ISO 9241-210:2019 [140], which tackles the human-centred design for interactive systems, the concept of Usability can be defined as the "extent to which a system, product or service can be used by specified users to achieve specified goals with effectiveness, efficiency and satisfaction in a specified context of use". This respective ISO form was successful in implementing an accepted foundation for defining and applying usability in a variety of different fields [10]. When addressing Usability, it is important to address the terms listed in the ISO 9241-11:2019 that surround this concept: **Satisfaction**; **User**: Person who interacts with the product; **Weight** of the components; **Size** of the components; **Material** used on the components. According to Nielsen [141], Usability can be defined through the following attributes:**Learnability**: the system should be easy to learn; **Efficiency**: the system should be efficient in a way that the user can be highly productive with it; **Memorability**: the system should be easy to remember, without the user needing to learn how to work with it after long periods of time without using it; **Errors**: the system should perform with few, and if the case, easily recoverable errors, i.e. without breaking errors; **Satisfaction**: the users should be satisfied with the system.

There are currently several standard and multi-purpose questionnaires focused on assessing the perceived usability of products or systems according to the user's own satisfaction [28]. Some of the most widely used standardized usability questionnaires are the Questionnaire for User Interface Satisfaction (QUIS), Software Usability Measurement Inventory (SUMI), Post-Study System Usability Questionnaire (PSSUQ), and System Usability Scale (SUS) [28]. This usability validation concern is depicted in Wang et al. systematic review [142], where the multiple MoCap systems are not only validated in terms of hardware and performance, but also in terms of usability.

3.1.2 Wearability

Wearability was defined by Gemperle et al. [143] as the "interaction between the human body and the wearable object". According to Knight et al. [144], when analyzing the wearability of a product, it is important to assess the impact of the system on the user, at the physiological, biomechanical and comfort

level. Physiological effects are related to the energy expended when performing a task while using the wearable device [144]. Biomechanical effects refer to the physical loading that can induce fatigue on the user, and the changes in posture and movement patterns [144]. Lastly, the comfort is associated with the discomfort perceived by the wearer, induced by the musculoskeletal loading or due to stresses localized in certain physiological systems, and his general well-being [144].

When addressing the wearability of MoCap systems, concerns such as sensor placement and attachment, as well as the weight, weight distribution, dimensions, and materials of the components need to be considered [72, 142]. Also, the shape and system aesthetics can have a psychological impact on the user and need to be addressed to maximize its wearability.

Therefore, the following factors are intertwined with the wearability requirements for wearable systems [72, 142]: **Placement**: it should fix the sensors in the right location; **Comfort**: it should promote physical and psychological comfort, be light, and use a comfortable textile; **Flexibility**: it should not restrain the movements of the user; **Scalability**: it needs to be adaptive to the different body types; **Ease of use**: it should be easy to use and easy to put it on and take it off; **Aesthetics**: it should be acceptable in a social and personal context. A wearable motion capture system, to be accepted and worn by the user, should fulfill these wearability requirements. The way the electronics are integrated in the textile also influences the system's wearability [114].

3.2 System Conceptualization

The main goal of this work is to improve Ergowear 1.0, by assessing its limitations and building upon those, based on a user-centered design methodology.

The system was designed as a wearable, MoCap system, capable of estimating the orientation of the user's upper body joints, using magnetic and inertial data. Furthermore, the hardware and software of the system needs to be prepared for the addition of future features. Currently, the planned applications for this system are to serve as a stand-alone, instrumented-based ergonomic assessment tool, provide postural awareness to the user, and to be integrated as sensing technology in a Human-robot Collaboration framework. For this, two main approaches were defined: a technical based approach and an usability and wearability approach. Fig. 18 illustrates the different aspects that comprise each approach.

For the production of the new iteration, **low-cost, but efficient approaches were deemed of great value**, since the system is to be used as a cheaper alternative to the commercial line products. This low-cost approach was already proved to be possible by the authors of [63]. **Moreso, the performance of the technical aspects must not compromise the wearability of the system**. This translates in: quantity and quality of the inertial sensors and vibrotactile motors, as well as their positions; portability of the system, and sizing and weight (and weight distribuition) of the system and the individual parts that compose it.

Furthermore, substantial attention was dedicated to the reform of the wearable garment, since the

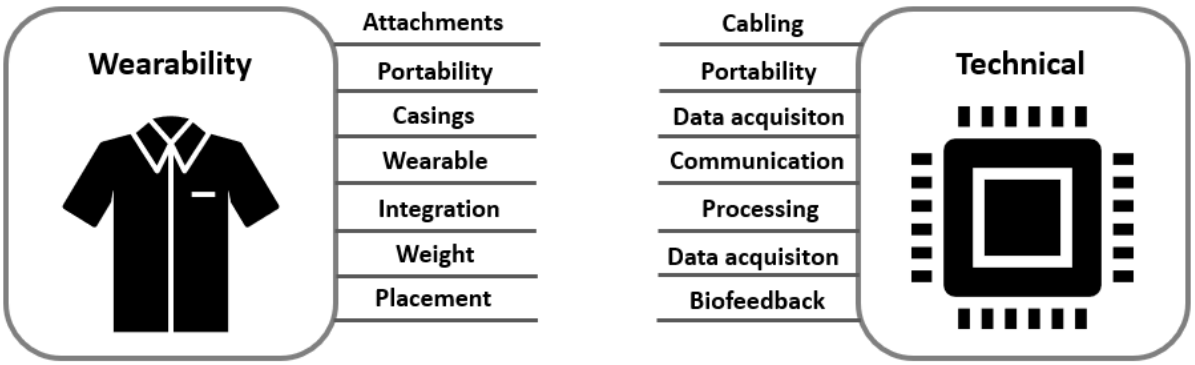

Figure 18: System's approaches.

previous one presented several limitations in terms of wearability and usability. The casings were also a target of rework, since it was observed that they have great potential in terms of miniaturization. These casings serve as a means to integrate the hardware onto the suit.

For the biofeedback system, vibrotactile motors were considered to be placed on each of the user's upper body joint. These motors are responsible for warning the user to correct his posture in the respective joint that is taking an incorrect posture. This will be done if an ergonomic-based reference sheet is added to the system as an ergonomic assessment tool, such as the RULA [19].

For the system to be portable, a decent-sized power source must be embedded in the suit. Moreover, a processing unit must also be integrated into the wearable so it can centralize the data and send it to a main station, **in real-time**, as well as receive commands from the main station to enable/disable the biofeedback motors.

The main station, in turn, must be able to process the acquired data, estimate the orientation of the joints, perform the sensor-to-segment calibration, and execute any future features that are to be added into the system. For it to be possible, a computer with the required specifications will be used.

3.2.1 Requirements

As previously stated, a set of requirements were devised for the system's design. The nature of these requirements can be divided in: Functional requirements, Usability requirements, and Technical requirements.

It is important to state that the system's requirements were defined by a multidisciplinary stakeholder panel composed by engineers (electronic and biomedical) and ergonomists. Most of the requirements were drawn from previous field work and from experience. These requirements are based on the ones in [29]. Some requirements were added, namely in the Usability and Technical requirements' list. One of the main requirements added to the list was the fact that the system needs to be low-cost, which was based on the work developed in [63].

Table 7: System's Functional Requirements.

Type	Requirement
Functional	Correctly measure human movement (f = 10 Hz)
	Monitor the upper body (i.e., trunk, neck, and both arms and wrists)
	Communicate wirelessly to a base station (processing computer)
	Allow real-time data streaming
	Allow joint angle estimation
	Allow ergonomic risk estimation
	Provide posture awareness to the operators
	Promote the improvement of the user's posture
	Allow the integration with the collaborative Robot
	Assure interoperability

3.2.1.1 Functional requirements

These requirements are associated with the functionality and purpose of the system. As specified, this system comprises a **smart garment, capable of monitoring the upper body segments of the user**. This is done through the use of inertial sensors embedded in the garment. With the data acquired by these sensors, the upper-body joint angles are calculated, and with the help of an ergonomic assessment sheet, it is possible to determine the real-time ergonomic risk of the worker. These requirements are described in Table 7.

3.2.1.2 Usability Requirements

The Usability requirements focus on the Usability and Wearability aspects of the Wearable. These requirements are described in Table 8.

Table 8: System's Usability Requirements.

Type	Requirement	Metric	Ideal Values
Usability	Must be comfortable	-	-
	Shall not restrict or jeopardize the user's movements	-	-
	Should be lightweight (comparable to women's winter jacket)	weight (kg)	0.5-1.0
	The modules' height dimensions should be inferior to the limits of intimate space of the human being (so that the garment is perceived as part of the body [143])	height (cm)	<12 cm
	Shall not create skin irritation	-	-
	Should be easy to don/doff(to be similar to a casual piece of clothing)	time (min)	<1 for each action
	Should be compact and discrete	-	-
	Should be intuitive to use	-	-
	Should be easily rechargeable	-	-
	Should be pleasant for the eye(to be more accepted by the user)	-	

3.2.1.3 Technical Requirements

The Technical requirements target the system's technical performance, covering its hardware and software's specifications. These requirements are described in Table 9.

Table 9: System's Technical requirements.

Type	Requirement	Metric	Ideal Values
Technical	Autonomy for a full work cycle	hours	8
	Absence of packet loss	% of packet loss	<1 (at least <2.5)
	Absence of packet corruption	% of packet corruption	0 (at least <2.5)
	Low latency times	ms	<19 (at least <50)
	Cover the predicted distance of operation between a main station and the processing unit	meters	10 (at least 4)
	No failures in receiving commands from the main station	% of failures	0
	Electromechanical robustness	No failed connections with the sensors	0
	Be Low-cost [63]	EUR	<500

3.2.2 Sensor Placement

To successfully estimate the orientation of a human joint, it is necessary to possess a sensor in each of the adjacent anatomical segments. For example, if the objective is to estimate the orientation the elbow,

the orientation of the IMU placed on the forearm must be known in regard to the orientation of the IMU placed on the respective upper arm [48]. Therefore, to extract the orientation of a respective joint, the difference between the attitude of the distal segment and the proximal segment must be calculated.

In terms of sensor positioning, the previous iteration of the system was expected to acquire data from all of the upper body joints, including the trunk. This leads to having a sensor placed in each of the user's anatomical segment. This conforms with what can be observed in Table 4, in which the more complete MoCap systems possessed an IMUs in each of the anatomical segments. However, the spine is more complex to estimate its orientation due to the fact that it is comprised of several vertebrae, which have some freedom of movement between between each other. In this case, a compromise between data quality and comfort and data output was considered. More sensors on the trunk would lead to a better representation of its curvature. Nevertheless, it would also lead to: increase weight, less comfort for the user, increase in the overall costs and in data output, which could compromise the data sampling frequency. Therefore, as a compromise, both the sensors in the upper trunk and pelvis were maintained in the same positions.

Therefore, a sensor in each of the human body's upper body anatomical segments, including the pelvis, was defined for the wearable. Furthermore, if possible, the sensors need to be placed on areas with a planar surface, as the sensors need to be aligned with the respective anatomical segment's frame. Moreover, the area where the sensors are placed should lack muscle tissue, due to the low-frequency noise originated from its activation, which would affect the data acquisition.

In this context, there were no substantial changes from the previous iteration regarding sensor placement. The sensors are currently positioned on the: pelvis (S1), upper trunk (T2), head, upper arms, forearms and hands. More specifically, and according to the requisites defined in the previous paragraph, the sensors should be placed on: the back of the hands; the top of the forearms, close to the wrist where it's mostly plane and lack muscle tissue; midpoint of the upper arms, facing outside of the body, in between the triceps and the biceps; back of the head, to be aligned with the trunk; upper trunk (T2) and close to the pelvis (S1). This setup is illustrated in Fig. 19

3.2.3 Wearable System

The first concern regarding the wearable was its overall design, which was mainly inspired by the reviewed commercial, wired, MoCap systems: Shadow Motion, XSens Link, Rokoko Smartsuit Pro, Nansense Products, among others. One common feature between commercial systems is the **concealment of the electronics**, under zippers or textile channels. This is a useful measure to increase the overall appeal of the suit leading to it being more generally accepted by the user - increase in wearability. Furthermore, an elastic headband was considered to integrate the head sensor. **An elastic waistband was defined to help press the lumbar area of the garment to the skin, if needed.** Fig. 20 represents an illustration of the design of the new wearable, excluding the vibrotactile motors.

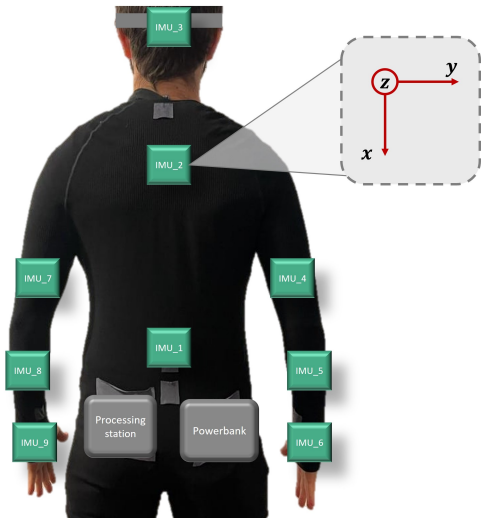

Figure 19: Sensor positioning on the wearable, along with its orientation.

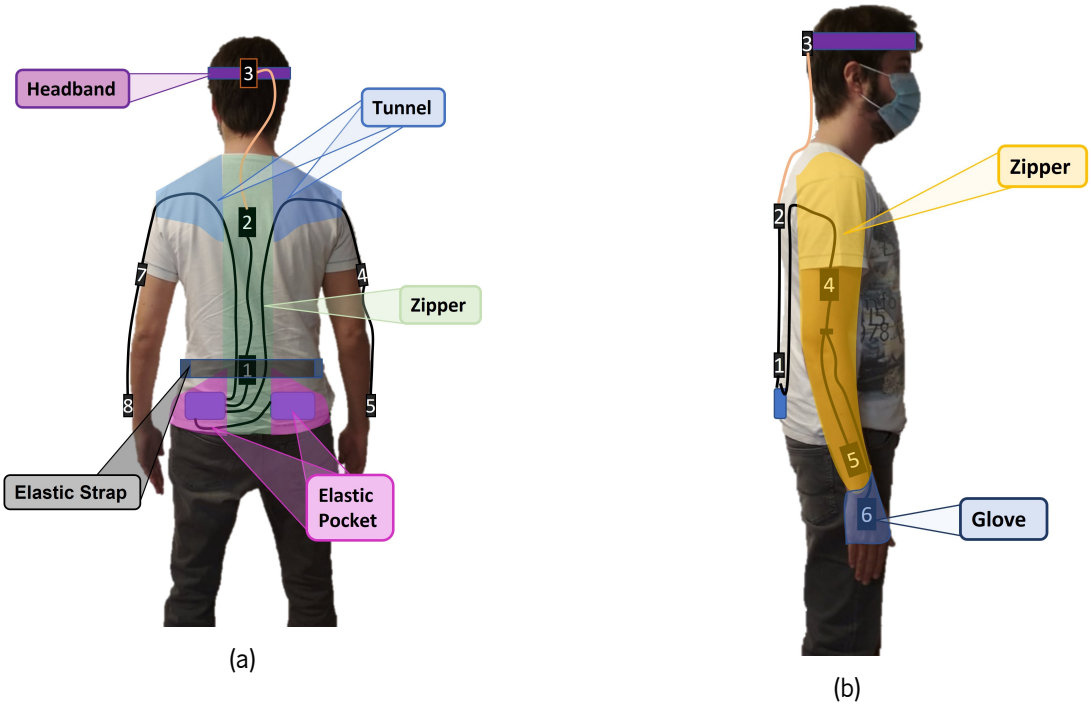

Figure 20: Proposed schematic for the wearable, illustrated on a person for reference. a) Picture from the back and b) side-view.

3.2.4 Biofeedback System

For the biofeedback system, each of the analyzed joints need to be able to receive feedback: trunk, neck, elbows and wrists. Moreover, the vibration of the biofeedback motor must be clearly felt by the user, and not be muffled by the textile of the garment. Using less denser meshes on the areas where these

motors are placed can conform with this requirement. Elastic pockets will be used to fix the motors and compress them against the skin. The motor channels in the proposed setup are displayed in Fig. 21.

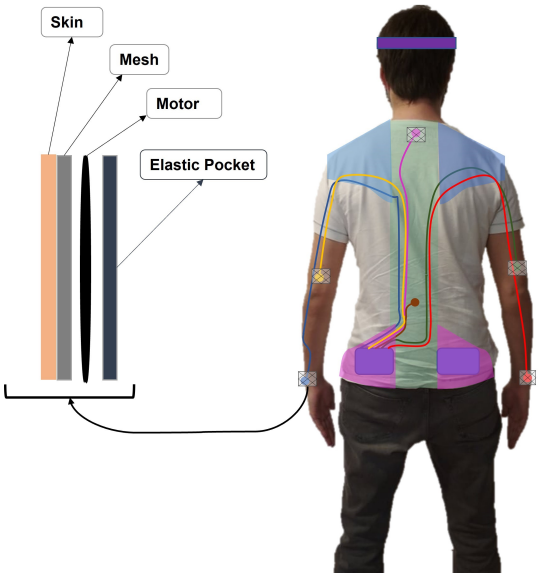

Figure 21: Feedback system overview.

4

System's Development

4.1 System's Development - Wearable

To integrate the designed electronics in a wearable system, a piece, or multiple pieces, of clothing were devised. To address this part of the system, inspiration was drawn from the reviewed, commercial, inertial MoCap systems, as they have their systems validated enough to be commercial products.

Several aspect of the wearable configuration were considered, such as the textile, attachments, piece of clothing, cabling configuration, and segment dimensions. These factors were addressed in accordance with the respective requirements, as stipulated in the Chapter 3.

This part of the project was done in collaboration with the enterprise Valérius Textiles S. A.. The wearable itself, along with all the testing samples, were produced at Clothius. Fig. 22 represents the confection wing of the company, where the garments developed for this project were produced.

4.1.1 Clothing

The garment was the first step addressed in the wearable's design, as it would serve as the basis for the system. In the previous iteration, a combination of a cyclist's jacket, headband and gloves was used to integrate the hardware. This led to the origin of certain limitations which would hold back the overall performance of the system.

As observed, for example, in the case of the XSens Link, a tight-fitted full-body garment, including fingerless gloves, was used as the basis of the wearable. But since the proposed work was only targeted for upper-body monitoring, a full-body piece of clothing was not deemed necessary. Instead, as an alternative to pants for the lower body, shorts were used, **as a fixing point is only necessary in the crotch area, to avoid the garment to slide along the torso.** In addition, fingerless gloves were added to avoid the sleeves from sliding along the arm.

Figure 22: Confection warehouse of Clothius.

4.1.1.1 Textile Composition

To enable the fixation of the sensors in regard to the user's anatomic landmarks, a compressive textile, capable of contouring the user's body, was necessary. This can be observed in the commercial examples mentioned previously. This can be achieved with a textile composition with a sufficient prevalence of elastane.

Two samples of a garment, that served as the basis for the wearable, with different compositions - 95 % polyamide / 5 % elastane; 92 % polyamide / 8 % elastane - were provided by Clothius. In Fig. 23, one of the samples is illustrated. In Fig. 24, a user, wearing the same sample, can be observed. Both samples were trialed by the same user, which evaluated them in terms of comfort and mobility. The sample with the **composition of 95 % polyamide / 5 % elastane was selected**, as the alternative proved to be **more compressive, restricting the user's movements and being overall more uncomfortable, according to the user.**

4.1.1.2 Cabling and Connectors

Cabling and connection spots were addressed. One of the major problems regarding the previous wearable was the fact that the connectors were integrated into the module's PCB. Due to this, when the cables' connectors rotated, the sensor rotated with them, which highly affects the angle estimation accuracy. So, when the cable moved in regard to sensor module, the connector would directly rotate the same module, due to its rigidity and heavy weight, **compromising the fixation of the sensor in regard to**

Figure 23: Basis for the proposed wearable.

(a) (b)

Figure 24: Wearable sample worn by a user, with markings for further alterations. a) Picture from the back and b) side-view.

the respective anatomical segment. Therefore, to overcome this limitation, the connections were to take place in the **middle of the respective anatomical segment** - cable-to-cable connections - away from the sensor modules, allowing the connector's movement without influencing the sensor's position and orientation.

4.1.1.3 Attachments

To attach the sensors to the respective anatomical position, velcro patches, with exterior tightening straps to reinforce sensor fixation, and compressive elastic pockets were considered. The latter were selected for the following reasons:

1. Velcro **does not have elasticity**;
2. Velcro needs to be sewn onto the textile, while the pockets can be thermoglued, which provides a more clean and professional look to the wearable. Moreover, the process of sewing the velcro patches would require the use of more machinery, raising the production costs, while the elastic pockets can be produced using the same machine that manufactured the garment;
3. Elastic pockets are compressive by nature, without the necessity of any exterior reinforcement, which is not the case with the velcro straps.
4. The use of elastic pockets, that would exert pressure downwards, would guarantee that the sensor modules would be fixed to the skin, so that they are more resistant to movement-inducing factors.

For the biofeedback system, a type of elastic pocket was designed in which each motor would slide in. The inner textile in those areas are composed of a lighter mesh which does not significantly attenuate the motor's vibration, so it can be easily perceived by the user. In addition, the outer part of the pocket was made of an elastic textile, so it compresses the motor, maintaining it immobile, and pressures it against the skin.

4.1.2 First Sample - Inner Layer

The first sample, provided by Clothius, corresponded to the inner layer of the wearable, i.e., the basis of the garment, with the elastic pockets glued on. In Fig. 25, the referenced sample is displayed while being worn by a user. In Fig. 26, a sensor module placed inside the respective pocket can be observed. To help with the compression of the sensor area onto the user's skin, a mesh with a vertical pattern was used, as illustrated in Fig. 27.

Some limitations were detected in this first sample:

1. Sensor pockets unaligned on the arms;
2. Lack of suit compression in the lumbar area in some cases;
3. Lack of suit compression in the wrist area.

They were later communicated to Clothius, with several possible solutions being discussed. In Fig. 28, these limitations can be observed.

(a) (b)

Figure 25: Inner layer of the wearable. a) Front view and b) back view.

(a) (b)

Figure 26: Inner layer of the wearable, showcasing the elastic pockets. a) Upper arm pocket and b) hand pocket.

Figure 27: Vertical pattern mesh to help with the compression on the sensor area.

(a) (b) (c)

Figure 28: Limitations of the first wearable sample. a) Lack of wrist compression, b) misalignment between the hand and forearm sensors and c) lack of lumbar compression.

4.1.3 Prototype - Full Suit

To obtain the final prototype, several intermediary samples were trialed and tested, to detect and correct certain limitations. An elastic waistband, attached to the suit using holes, was used to compress the textile in the lumbar area. Furthermore, to not restrict the user's movements, a more elastic, and less denser mesh was used on the elbow and shoulder joints, as demonstrated in Fig. 29.

Moreover, an elastic headband was also produced, with an elastic pocket attached to it, for the head sensor. Unlike the headband used in the previous iteration, this one was produced taking into account

(a) (b)

Figure 29: Lighter mesh used on the a) elbow and b) shoulder joint.

heat dissipation and breathability. The headband is also depicted in the final prototype.

Lastly, the external layer was added onto the skinsuit. To access the electronics, zippers were used. Moreover, unlike the wearable of the XSens Link, textile tunnels were not used to allow the passage of the cables between the trunk and the sleeve, **as this layer would increase the textile rigidity in this area.** As consequence, this could limit the shoulder's range of motion, resulting in the user's discomfort. The final prototype is depicted in the Section "System's Development - Hardware".

4.2 System's Development - Hardware

This section addresses the hardware of the wearable, and the selection of the individual components.

4.2.1 System's Description

The hardware needs to cover the data acquisition system, biofeedback system, low-level processing unit, power supply unit, wireless communication system, and the cabling and connectors. The hardware integrated in the prototype can be divided in several classes, as illustrated in Fig. 30.

4.2.2 Acquisition System

The acquisition system is comprised of 9 MIMUs, that acquire the linear acceleration, angular velocity and magnetic field. The selected MIMU for the project was the Adafruit LSM6DSOX (3-axis accelerometer + 3-axis gyroscope) + LIS3MDL (3-axis magnetometer) board (Adafruit Industries, New York, USA).

The primary features of these sensors are the fact that they are **low cost**; have **low gyro bias and noise**, lower than the MPU-9250, used in the previous iteration, and with the same cost ($\approx$ 15$) and are widely accessible. The MIMU's characteristics are displayed in Table 10, as well as a direct comparison between the selected IMU and the previously used IMU - MPU-9250 [145–148].

One feature of these boards is the presence of wire-to-board connectors on each side, for Inter-Integrated Circuit (I2C) communication with the sensor. These connectors have 4 pins connected to

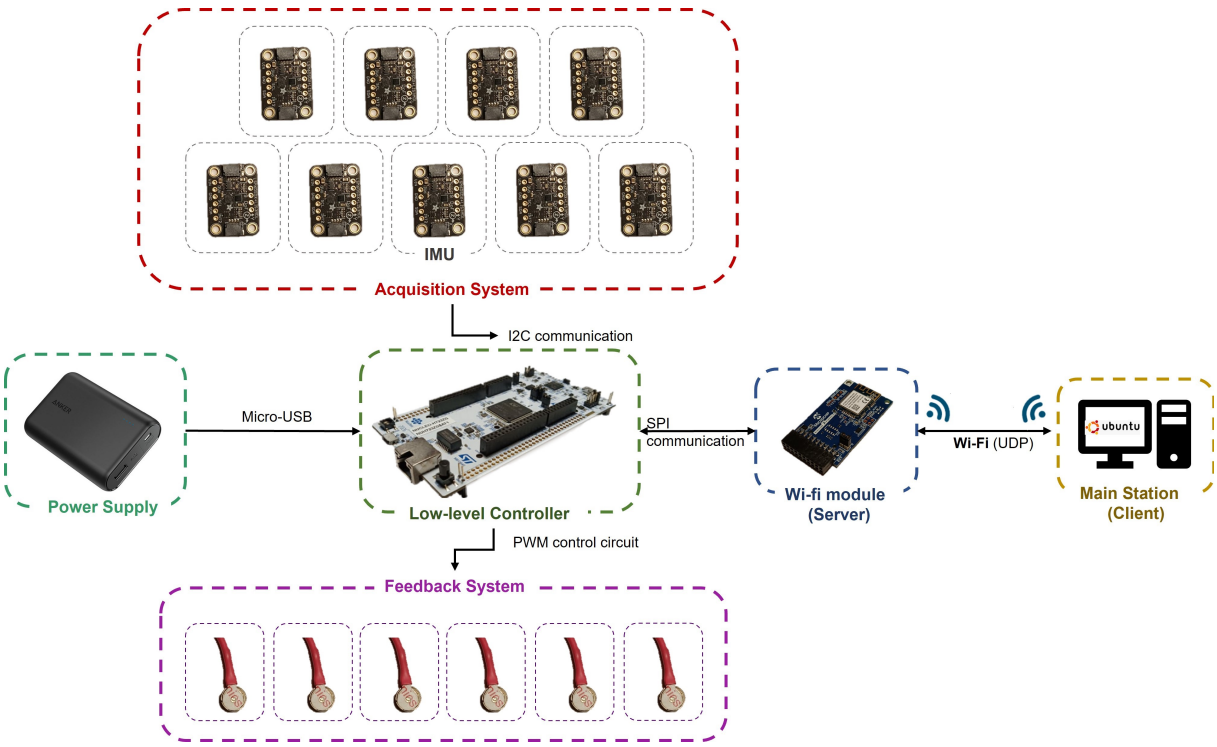

Figure 30: System's hardware overview.

the boards': input voltage, ground, I2C serial data (SDA) and serial clock (SCL), as illustrated in Fig. 31. **These connectors allow a direct connection to the sensor, avoiding the necessity of ad hoc designed PCBs with integrated connectors, which was the case wit the previous version**. This leads to a decrease in the sensor module's sizing, which is important to increase the overall usability of the wearable.

4.2.2.1 Sensors' Communication

Due to the use of the sensor boards inbuilt connectors, it is only possible to communicate with the sensor boards using the I2C protocol, discarding the use of the Serial Peripheral Interface (SPI) communication protocol. Each sensor board can alternate between two static I2C addresses [145]. Therefore, to cover all 9 sensor modules, **5 I2C buses** are required. According the datasheet [145], the sensor is established with a fast-mode I2C communication protocol, with a communication speed of 400 kHz. The sensors' communication setup is illustrated in Fig. 32. In this configuration, three separate ramifications will connect the sensors to the processing board. One of the ramifications will connect the lower trunk, upper trunk and head sensors. The other two will address each respective arm. Therefore, each ramification will connect three sensors.

From Fig. 32, it is possible to observe that at least 4 (I2C wires) + 2 (Supply + Ground) will need

Table 10: LSM6DSOX + LIS3MDL vs. MPU-9250.

Parameter	LSM6DSOX + LIS3MDL	MPU-9250
Supply voltage	1.9 V Min. - 3.6 V Max.	2.4 V Min. - 3.6 V Max.
Gyroscope rate	6.7 kHz	8.0 kHz
Accelerometer rate	6.7 kHz	4.0 kHz
Magnetometer rate	80 Hz	-
Gyroscope range	±2000 °/s	± ±2000 °/s
Accelerometer range	±16 g	±16 g
Magnetometer range	±16 gauss	±49 µT
Zero-g offset	±20 mg	±60 (X,Y) / ±80 (Z) mg
Zero rate offset	±1 °/s	±5 °/s
Zero-gauss offset	±1 gauss	-
I²C slave clock frequency	400 kHz Max.	400 kHz Max.
Current consumption	0,82 mA	3,7 mA
Dimensions	26 x 18 x 5 mm	26 x 18 x 5 mm
Price	$14.95	$14.95

to be present in each of the ramification's (trunk, right arm and left arm) cable. Since only 4 wires can be connected to the board at once, as illustrated in Fig. 31, the wires associated with the remaining I2C bus needed to continue along the cable. Therefore, the cable could not be totally cut to establish the connection to the sensor board. Thus, the defined solution was to apply the configuration illustrated in Fig. 33.

As detailed in Fig. 33, this configuration revolves around maintaining the wire wrapping of the unused conductor pair. This wire pair is untouched and proceeds to the next modules.

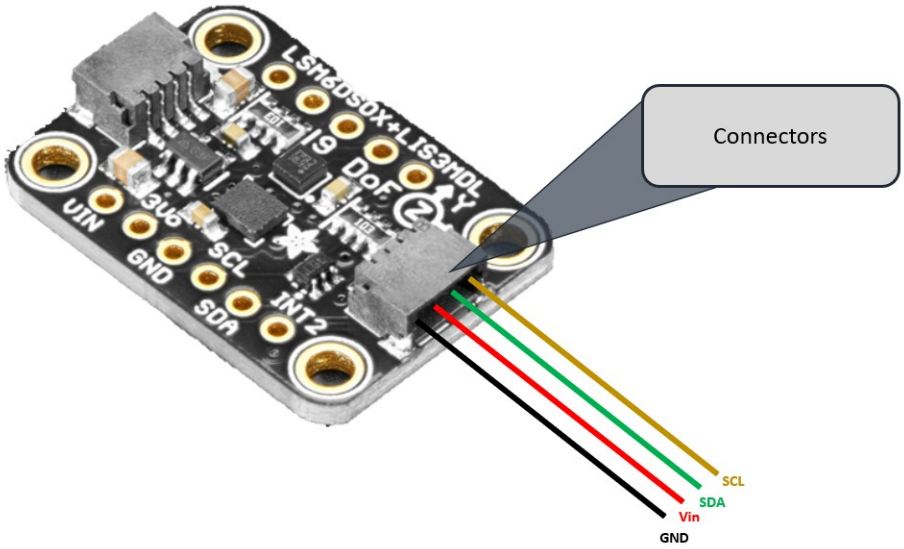

Figure 31: Sensor boards connectors.

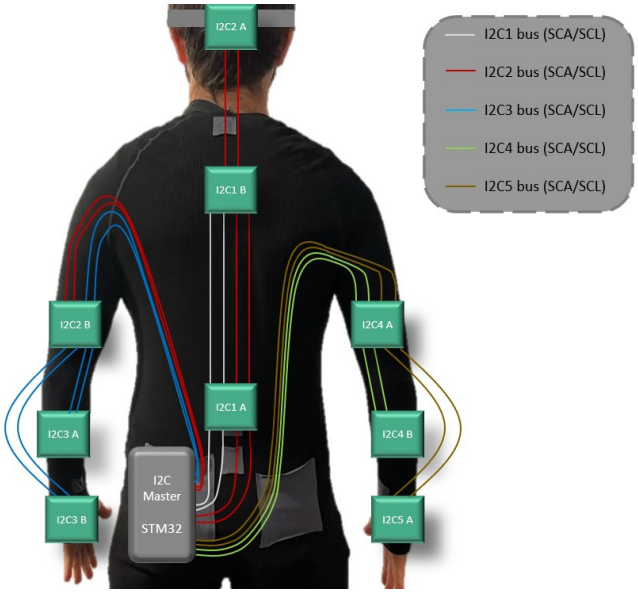

Figure 32: Sensors' communication setup.

4.2.2.2 Connectors

As previously stated, one of the priorities for this new iteration was to improve the cabling (and connectors) system, as the HDMI cables were to stiff and heavy, inducing unwanted changes in the sensor modules' orientation. Moreover, the previous cables were to long for the distances between consecutive modules.

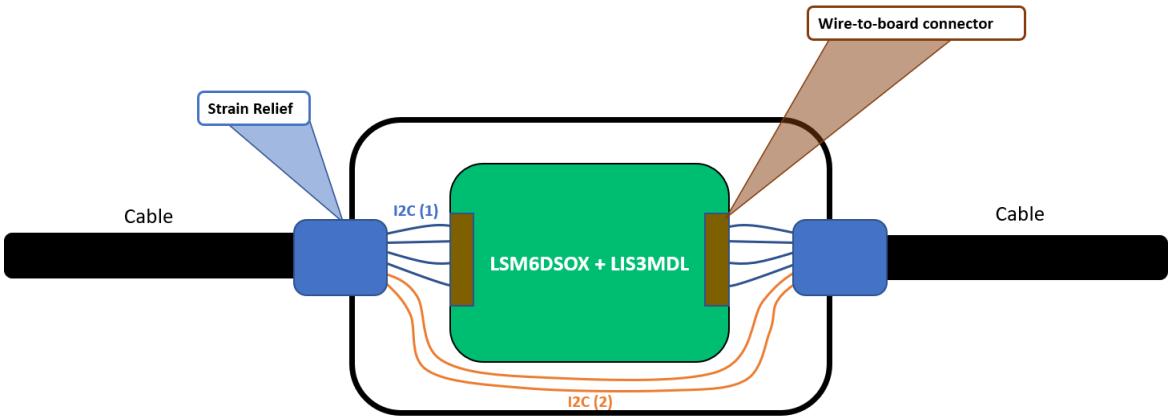

Figure 33: Wire configuration inside the sensor's casings.

For the connectors, it was decided that the connection point between the sensor's modules should be at the middle of corresponding anatomical segment, away from the joints. Therefore, the movement of the cables would not interfere with the sensor modules. For this type of connection, circular, push-pull connectors were selected, as they can be easily connected/disconnected, whilst being robust.

Lastly, the connection between the cable's wires and the respective sensor is done through the use of wire-to-cable connectors. To establish this connection, wire crimps were manually crimped on the cable wiring. Then, the individual wires were placed inside the female housing, which then connected to the sensors' connectors. These types of connectors are illustrated in Fig. 34.

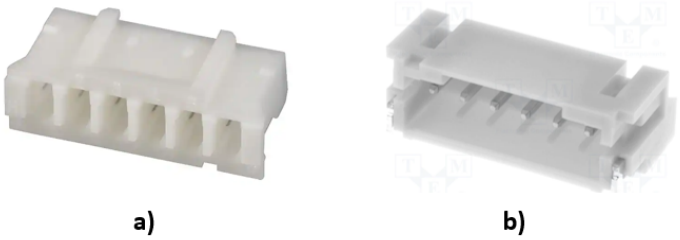

Figure 34: Wire-to-board connectors. a) Female version and b) the male equivalent.

These types of connectors were also used in the low-level processing unit, to establish the connection between the processor and the cables.

4.2.2.3 Cables

Various alternatives were procured, such as flat cables, conductive textiles, USB-C cables, and circular cables. But since the selected connectors were circular, the search was limited to circular cables. Specifically, cables with a **maximum outer diameter of 5 mm**, so they could be clamped to the connectors, and **with high flexibility**, so they would not restrict the user's movements and tilt the sensor modules due to their stiffness.

Although the flexibility of the cables is an important aspect to take in consideration, it was also necessary to consider that, for the robustness of the sensors' data communication, especially in an industrial environment, the **cables should be shielded**. This is due to the fact that the wired communication protocol (I2C) can suffer disturbances from electromagnetic noise, which is prevalent in the industrial context. Thus, only shielded cables were considered. Moreover, as previously observed, each cable will need to have at least 6 conductors to cover the communication and power supply needs of the sensors.

During the design of the system's configuration, in terms of the cabling and connectors logistics, some issues were identified and addressed. Firstly, the length of connection between the circular connectors correspond to 7.7 cm, which is too long for it to occur between the forearm and the hand sensors' modules. In this case, the connection would happen on the wrist joint, meaning that this joint would be restricted of movement. Therefore, an y-splitter was used to separate the upper arm cable in two: one for the lower arm and another for the hand. Two alternatives were evaluated for the cable splitter: welding the respective cable wires together, and cover them with a printed casing and fixing the wires with strain reliefs, or using circular connectors. To serve as a cable splitter, the circular connectors were used as they were robust enough to establish the connection between the cables' wires without compromising the wires' structure. This was the major limitation regarding the direct welding of the wires, as the **solder is a critical point, and can be easily broken with little tension.** In Fig. 35, the proposed cable splitter is displayed.

Figure 35: Y-Cable splitter.

With the use of the splitter cable, less conductors - 4 conductors - were required for the cables heading to the forearm and hand. This led to the procuring of cables with less diameter, specifically 2.8 mm of diameter. The selected cables are also made with a rubber jacket, making them more flexible, which is critical on the arm and hand segments of the user, as to not disturb their movement. This leads to an **improvement of the system's wearability.**

4.2.3 Biofeedback System

The biofeedback system is composed by 6 vibrotactile motors whose purpose is to vibrate to indicate that the user's posture is ergonomically incorrect in the respective area of the actuation.

The selected vibrotactile motors were **coin-styled ERM motors**. The model of these motors are the 310-122 (Precision Microdrives Ltd, London, UK) with: 10 mm of diameter, 3.4 mm of thickness, and 1.2 g of weight. These same motors were used in the previous iteration, and there was no defined reason to select other alternatives.

According to the datasheet [149], the motors' functioning can be summarized according to the graph illustrated in Fig. 36.

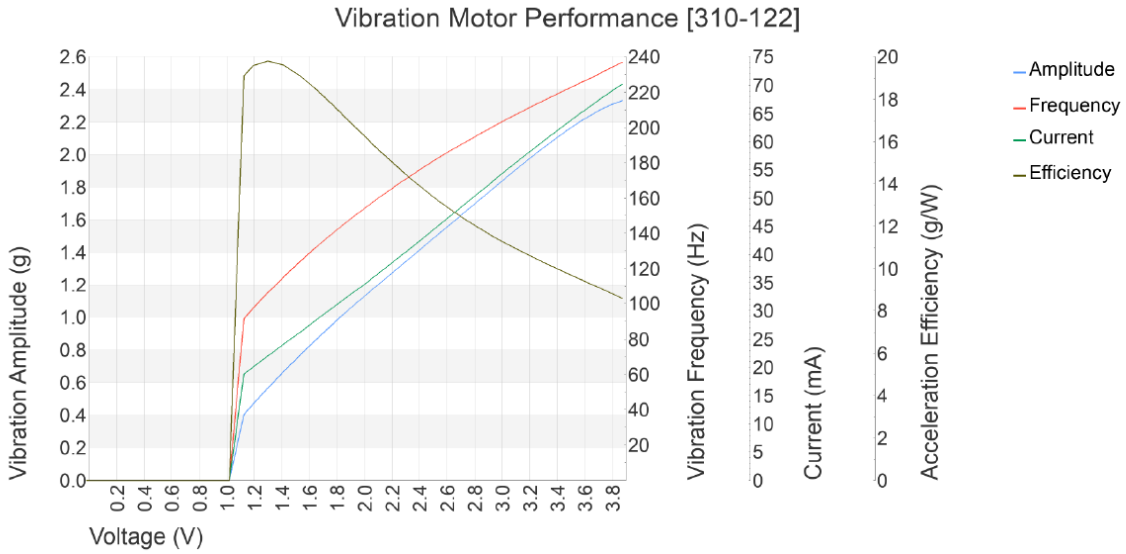

Figure 36: Vibration motor performance, obtained from [149]. Vibration amplitude (g), vibration frequency (Hz), current consumption (mA) and acceleration efficiency (g/W) vs. input voltage (V).

As described in Fig. 36, the current consumption, for an input voltage of 3.3 V, is around 60 mA, which is higher than the maximum current output - 20 mA - provided by the microprocessor's pins. Therefore, a Pulse-Width Modulation (PWM) control circuit was designed and implemented [150], using the TINA software (DesignSoft, Budapest, Hungary). The schematic for this circuit is illustrated in Fig. 37.

The circuit is based on a motor controller, using a CMOS n-channel MOSFET as a switch. The gate of the MOSFET is connected to the respective microcontroller output pin, which is a PWM channel pin. PWM output pins were selected to activate the motors, as they the have the capacity to control the motors' vibration frequency through their duty cycle, with a duty cycle of 100 % corresponding to an output signal of +3.3 V.

When the output signal of the respective PWM pin is LOW, the MOSFET is operating in the cutoff region, and therefore no current is flowing through the circuit. When the output signal is HIGH, the

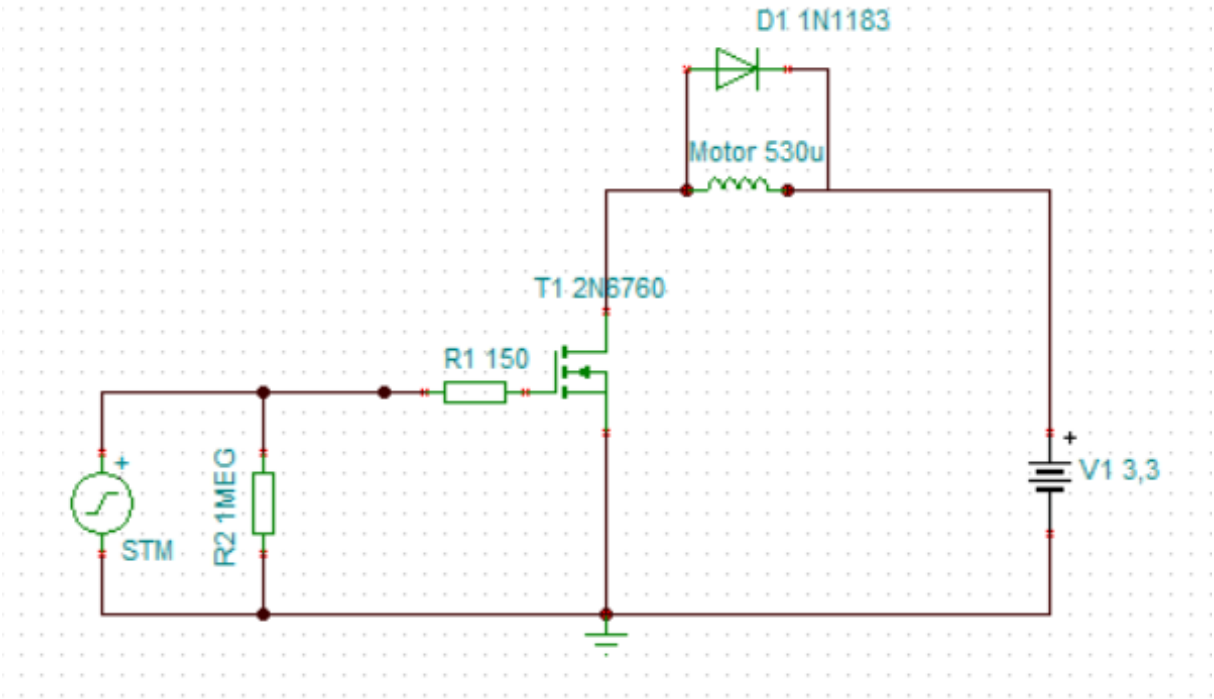

Figure 37: PWM motor control circuit.

MOSFET operates in saturation, as the Drain-Source voltage is always superior to the difference between the the Gate-Source voltage and the MOSFET's Threshold voltage. In this situation, the gate presents a theoretical impedance value of $0\ \Omega$, and the current will correspond to about 60 mA, as observed in Fig. 36. A rectifier diode - D1 - was added in parallel to the respective motor, functioning as a flyback diode. This was devised to allow the safe discharge of the inductive charge of the motor, avoiding unwanted electric arcs. Moreover, two resistors were added in the circuit design. Following Fig. 37, the purpose of R1 is to limit the current at the gate when the signal changes, which could lead to the accumulation of heat in the MOSFET. R2 is a pull-down resistor whose function is to force the respective PWM signal to ground, when it would be floating during the startup. This way, the motor is not activated during the setup of the processor.

4.2.4 Processing System

The processing system is composed of a low-level controller and a processing station. The main station is the primary processing force of the system, and is comprised of a personal computer.

For the low-level controller, only **low-cost**, development boards were considered. The main features considered for a processing board were: the presence of at least **6 PWM output channels** for the 6 vibrotactile motors; **high CPU core clock frequency**, to avoid any bottleneck or packet loss; and at least **5 I2C bus peripherals**, to avoid the use of multiplexers, which could negatively impact the speed of data acquisition rate. This last requirement was defined due to the fact that the selected sensor boards

can have **2 separate I2C addresses**, leading to 5 I2C buses to cover all of the sensor communications. Furthermore, features like the **current consumption and weight** of the processing unit were accounted, as the previous low-level controller was unable to fulfill the power consumption requirement, achieving a maximum autonomy of less than 8 hours, which is the equivalent of the daily working time in Portugal. In terms of the RPi4, it was considered that it consumed too much power, which compromises the system's autonomy requirement. Moreover, the high energy consumption also translates to heat accumulation, being uncomfortable for the wearer during its use.

Only one development board was encountered with **5 I2C bus peripherals**, the NUCLEO-H723ZG (STMicroelectronics, Genebra, Switzerland). A comparison between the main features regarding this board and the RPi4 are specified in Table 11 [150–152].

Table 11: Stm32H723ZG vs. RPi4.

Parameters	NUCLEO-H723ZG	RPi4
Nº I2C channels	5	1 (Multiplexer)
PWM channels	8	2
CPU core speed	550 MHz	1.5 GHz
RAM	564 b	4 Gb
Dimensions	133,34 x 70 x 19 mm	85 x 56 x 16 mm
Weight	200 g	180 g (w/ heatsink)
Current comsumption	215 (430 Max.) mA	600 (1200 Max.) mA

One of the main disadvantages of this processing board is the **increase in width and length dimensions** compared to the RPi4. However, the advantages of this processor make this compromise necessary.

4.2.5 Wireless Communication System

For the wireless communication system, Bluetooth and WiFi modules were considered. The ATWINC1500 Xplained Pro [153] selected, due to the the accessibility and available documentation support of this product. The challenge was to port the libraries to the Nucleo-STM32H723ZG processor board. The board's dimensions are 21.5 mm $\times$ 14.5 mm $\times$ 2.1 mm. This WiFi module can connect to the Processing board using the SPI communication protocol.

4.2.6 Power Supply

To power up the processing board, a micro-usb connector which allows for a **5 V** input, is available. Moreover, the power supply **needs to be portable**, to endow the system with ambulatory characteristics.

The powerbank has the advantage of being **portable**, **aesthetically pleasing**, **easily rechargeable**, and can **directly provide 5 V to the processing board**. Moreover, due to its USB ports, it can directly connect to the respective processing board, using a USB-to-micro-USB cable. Furthermore, **it is easily replaceable**. Therefore, if the current power supply unit is over-dimensioned in regard to the system, it is easy to replace it with a more suitable alternative.

4.2.6.1 System's Power Consumption Tuning

An analysis of the proposed hardware's system theoretical current consumption was performed. The STM board is expected to supply the voltage to all of the wearable electronics: feedback system, WiFi module and the acquisition system. Each of these modules are supplied with ≈ 3.3 V. The expected maximum current consumption for each of these systems is (assuming all systems are active at the same time) [145, 146, 149, 150, 153]:

- Feedback system ≈ 60 mA $\times 6 = 360$ mA;
- Acquisition system $\approx (0.27 + 0.55)$ mA $\times 9 = 4,92$ mA;
- WiFi module ≈ 268 mA
- Feedback system + Acquisition system + WiFi module $\approx 632,92$ mA
- STM32 ≈ 250 mA
- $total_{max} \approx 882,92$ mA

Extrapolating this value to an 8-hour session, results in a minimum capacity of $7063,36$ mAh, which is significantly smaller than the selected powerbank's capacity of 13400 mAh.

According to the NUCLEO-H723ZG datasheet [151], its 3.3 V output is limited to a maximum current of 500 mA (limited by a voltage regulator), which is less than the stipulated total theoretical current consumption - disregarding the Processor. Therefore, a fixed 3.3 V output voltage regulator was procured, to safely supply the WiFi module. The regulator receives 5 V from the 5 V output of the STM board, which does not have a maximum current limit. The board's 3.3 V output was used to supply the acquisition and the feedback systems.

In terms of the power supply, no better alternative was found than a powerbank. These are **portable and can generally be directly connected to the circuit if the latter has a USB charger integrated**. To make a proposal regarding the powerbank, the current system's autonomy was tested with the

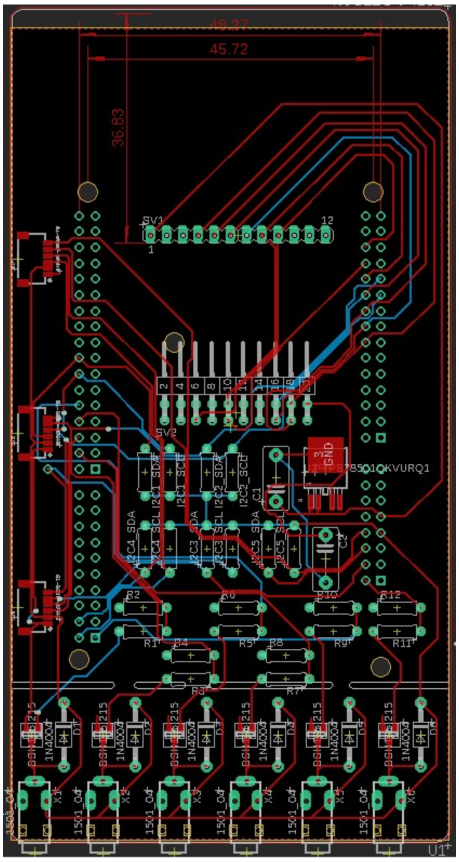

Figure 38: PCB layout.

one used for the previous iteration of the system. Therefore, the Anker Powercore **13000 mAh** (Anker, Changsha, China), with 100 mm ×100 mm ×50 mm, and 260 g, was temporarily maintained for the new iteration. This power supply is theoretically over-dimensioned when compared with the wearable's power consumption, as seen previously. Nevertheless, one of the main reasons this powerbank was selected was due to the fact that it presents a weight comparable to the processing station. This is important to address since the power supply and the processing unit are located at the same height, simmetrically in regard to the user's spine. In this context, if one of the units is considerably heavier compared to the other, the weight distribution is unbalanced at the hip level, leading to the human body trying to compensate this weight disparity. This would lead to a lower level of comfort of the overall system.

4.2.7 Prototyping

After the hardware was tested and validated on a breadboard, namely the biofeedback system, sensor reading system and WiFi communication system, the respective PCB was designed and developed using the Eagle Software (Autodesk, San Rafael, USA). The PCB layout is illustrated in Fig. 38. The resulting board is shown in Fig. 39.

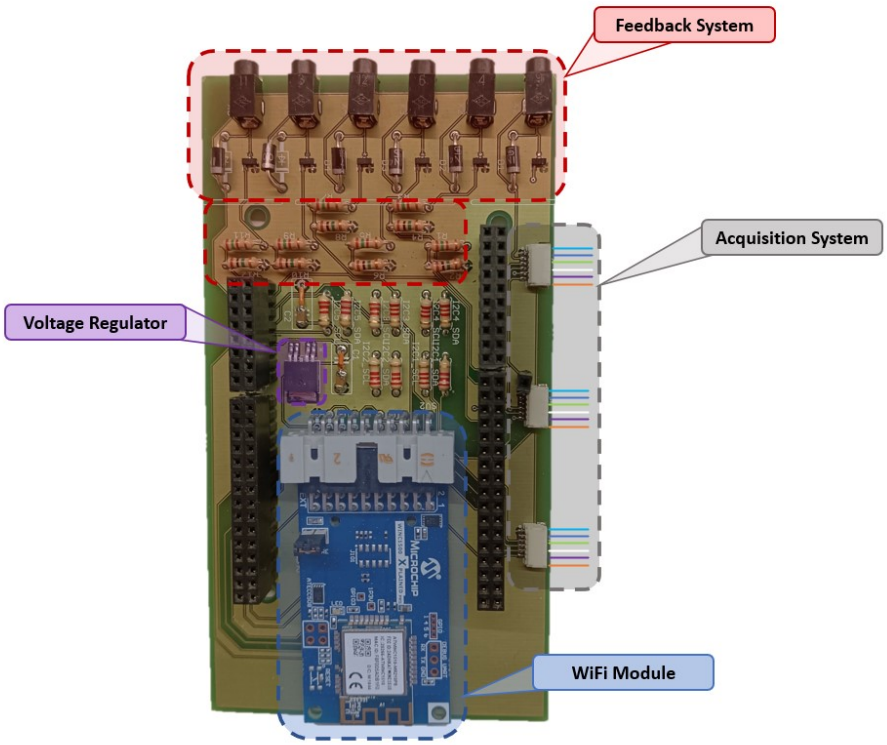

Figure 39: Master PCB overview.

4.2.8 System Integration

Along with the PCB of the master board, the hardware associated with the acquisition system was integrated into the suit. The cable wiring was manually connected to the PCB and the sensor boards. After each connector was manually assembled, the conductivity between the sensor boards' pins, and the processing unit, was evaluated, to ensure that the connections were robust. Several connections were repaired, due to the difficulty regarding the assembly process: the wiring, due to the small dimensions, was fragile, which led to situations in which the contacts ripped the wires, causing disconnections; in some situations, the contacts were crimped onto the wire, but the filaments were not in contact with the crimp; and in some other cases, there were short-circuits between cable wires due to the exposed conductors, after welding the wires.

Furthermore, the strain reliefs used inside the sensor modules didn't present much in terms of rotation attrition. Therefore, the wires inside the casings could rotate in regard to the sensor board, which was fixed onto the casing using screws. This could present a problem since the wires would suffer tension from these rotating movements. Therefore, to mitigate this effect, adhesive tape was applied into the socket where the strain reliefs would be set.

To integrate all of the hardware onto the suit, 10 3D printed plastic casings, using the Solidworks

(SolidWorks Corp., MA, USA) software, were designed and produced. These casings were carefully designed to include **rounded edges so they would not damage the wearables pockets and affect the user's comfortability.** Two main types of modules were produced: one master module, which was designed to carry the processing board, and 9 sensor modules, with each containing a MIMU. The master module weighs 189 g, and its dimensions are $146 \times 92 \times 37$ mm. Figs. 40 and 41 illustrates the processor inside the respective casing, with the latter the sensors' wire-to-board connection as well. Fig. 41 also demonstrates the final processing unit.

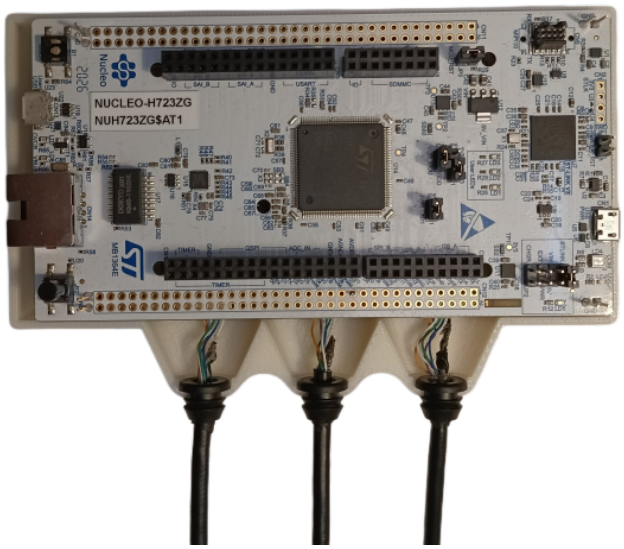

Figure 40: Processor inside the open master module. Upside view.

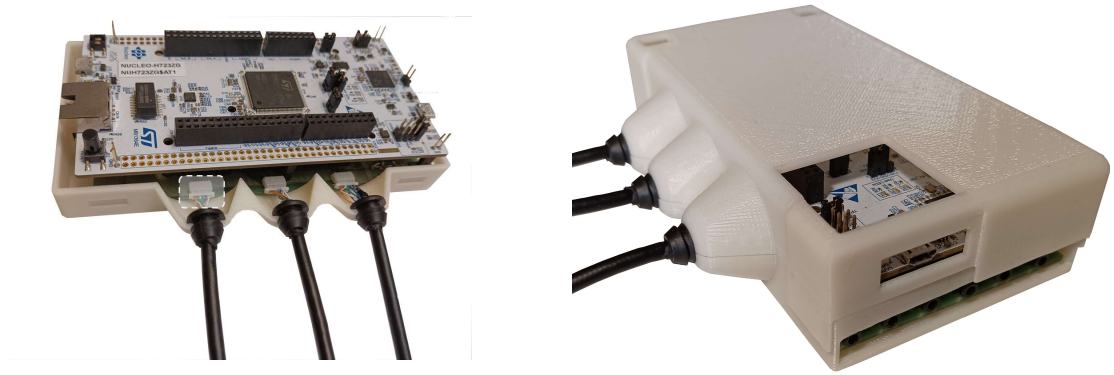

(a) (b)

Figure 41: a) Processor inside the open master module, with the sensors' wire-to-board connection shown. b) Processing unit,

The sensor modules can be divided in two types: the intermediary modules and the extremity modules. The former covers the sensors positioned on the back of the user, as well as the upper arms, in which

both sensor board connectors are used, which lead to the design of an inning and an outing for the cable. These modules weigh 15 g, with $52 \times 22 \times 13$ mm. Fig. 42 showcase the intermediary modules.

(a) (b)

Figure 42: a) Intermediary sensor module. b) Interior of the intermediary sensor module.

Lastly, the extremity modules cover the sensors on the head, forearms and hands, with $41 \times 22 \times 13$ mm, and 12 g. With the presence of screw holes in the sensor boards, these were harnessed on the casings to fix the sensors inside the modules. Fig. 43 illustrate these modules. In Fig. 43, it is also possible to observe the different components of the extremities sensor module, including the wire-to-board connection setup.

(a) (b)

Figure 43: a) Extremity sensor module. b) Interior of the extremity sensor module.

Furthermore, due to the lack of connectors in the modules, **strain reliefs were used to protect the cable wiring inside the casings from movement**, improving the robustness of the connection

between the cable and the board. The strain reliefs for the cables used on the wearable were procured in several distributors. However, the reliefs' dimensions were large enough to require an increase of the modules' dimensions just to include these strain reliefs. Therefore, the strain reliefs used in the casings were manually designed, and printed using a 3D printer, with the exception of the master module. For the latter, rubber grommets were used, as the casing was large enough to include them.

The garment, plus electronics, weighs around 1130 g. The full system is depicted in Fig. 44. Fig. 45 demonstrates the back and the sleeve of the wearable's external layer open.

4.3 System's Development - Software

Along with the hardware of the system, the software part of the system was also reworked on. A fusion filter was added, and since the low-level processor was altered, its software architecture was also updated. Moreover, a new block was added - the SDI.

The processing load of the system is divided in two processing stations: the low-level processor, which is located in the wearable, and the main station which is composed of a personal computer. The software overview of the system is illustrated in Fig. 46.

Since the designated sensor sampling rates are high, it was necessary to reduce all of the processing load to a bare minimum, to dedicate its processing power in sampling and sending the sensors' data. Therefore, the low-level processor is responsible for sampling the sensors' data, performing the SDI block, sending the resulting data, wirelessly, to the main station, and performing the sensors' calibrations. Furthermore, this processor also enables/disables the vibrotactile motors, through the commands sent by the main station.

In turn, the main station is dedicated to performing all of the more high-level functions such as performing the joint angles estimation, as well as any other system feature that is to be added in the future.

4.3.1 Low-level Control Unit

The software embedded in the low-level controller can be divided in three parts: **the system's setup, the main program and the interrupt routine.**

The system's setup covers the initialization of the microcontroller's GPIO, the timers, the SPI and I2C peripherals, followed by the initial connection and configuration of the WiFi module. Then, the WiFi module starts its own network, acting as an Access Point (AP). After the main station connects to the Atwinc's network, the initial communication with all 9 IMUs (or the IMUs that were specifically selected to operate in that session) is followed. Next, a 5-second subroutine is initialized, in which the each gyroscope's data is acquired, by starting the timer interrupt subroutine dedicated to acquire the sensors' data. During this subroutine, the user must be static and adopting the n-pose. After this subroutine, the timer interrupt is stopped, an the User Datagram Protocol (UDP) socket is initialized and bound to the selected communication port and to the IP address of the main station. When the controller binds the

(a) (b)

(c)

Figure 44: Overview of the wearable while closed. a) Front view, b) side view and c) back view.

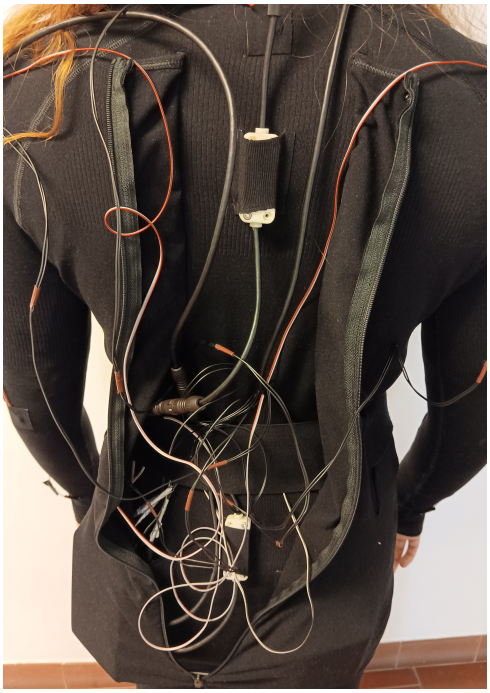

(a)

(b)

(c)

Figure 45: Overview of the wearable open. a) Rear view and b) side view. In c) the biofeedback system is absent, to showcase the connections between the modules.

UDP socket, it sends back to the main station the first message, signalizing the start of a data acquiring session. Lastly in the system's initialization, the processor waits for the start command sent by the main station. When it receives this command, the Real-Time Clock (RTC) and Timer_16 interrupt routine are initialized.

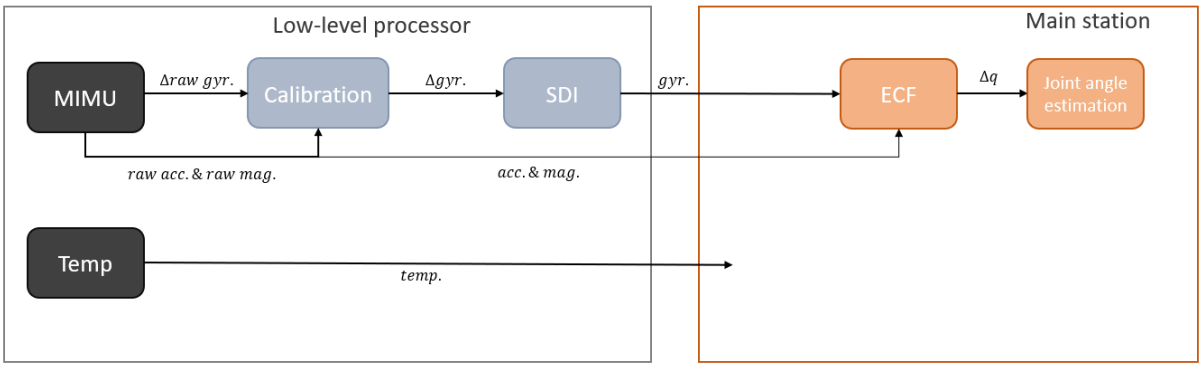

Figure 46: Software architecture overview.

The main program is dedicated to the WiFi handler, which is responsible for the WiFi communication callbacks, and building and sending the sensors' data to the main station. This block activates after the initial setup of the system, and it is constantly called in a "while" loop. The callbacks are triggered whenever the low-level controller: receives a connection request from the main station, is disconnected from the main station, sends the first message to the station, receives a command from the station and binds the UDP socket. In regard to the **receive callback**, its primary function is to activate/deactivate the selected motors - the selection of the motors is made by the main station. When the *send flag* is high the send block is executed in the main loop. In this block the SDI of the 5 saved gyroscope values is executed, resulting in an output value at one fifth of the gyroscope's sampling rate. Furthermore, also in the send block, the processor builds the message, and sends it wirelessly to the main station. The message is composed of the concatenation of: the message ID, the RTC timestamp, and each sensor's angular velocity, linear acceleration, magnetometer values and temperature.

Lastly, the **interrupt routine** is a time-based interruption, with an activation frequency of 240 Hz (frequency defined after the tests performed in the "System Characterization" section). This block is initialized the moment the main station sends the start command to the low-level processor. During each interruption, the controller acquires the gyroscope, and depending on the interrupt, the first, intermediary or final three sensors are fully read. This partition of the sensors' reading is done so that the full acquisition of all 9 sensors is not done in a single interrupt, which would take more time than what the interrupt frequency could handle. After **5 consecutive interrupt cycles**, the program acquires the timestamp from the RTC, and sets the *send flag* high.

To guarantee the automatic I2C communication between the processor and the sensors, a subroutine that analyzes the I2C communication status was implemented. If the communication fails, the processor will try to reset the failed communication with the respective sensor. If the time this subroutines takes surpasses the pre-determined timeout value, a mandatory reset is needed. For the user to know that the system will need to restart, a biofeedback signal was added in which all of the vibrotactile motors activate for a small amount of time.

The low-level controller software's architecture is illustrated in Figs. 47 and 48. For the sake of clarity,

the flowcharts depicting the main and timer programs were separated from the callback flowchart.

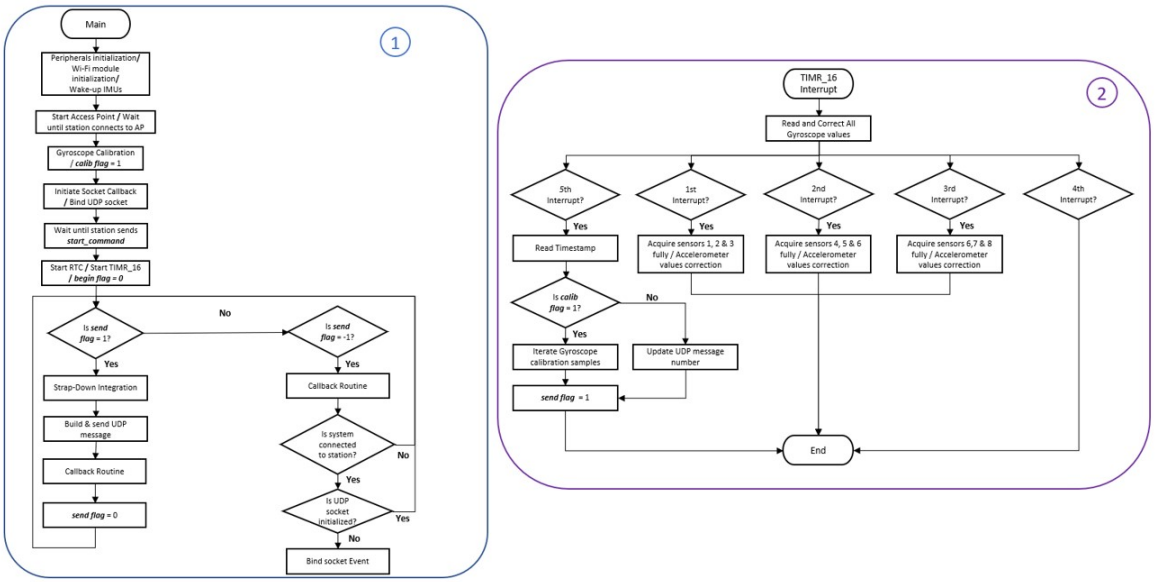

Figure 47: Low-level controller's flowchart for the main program (1) and the timer interrupt routine (2).

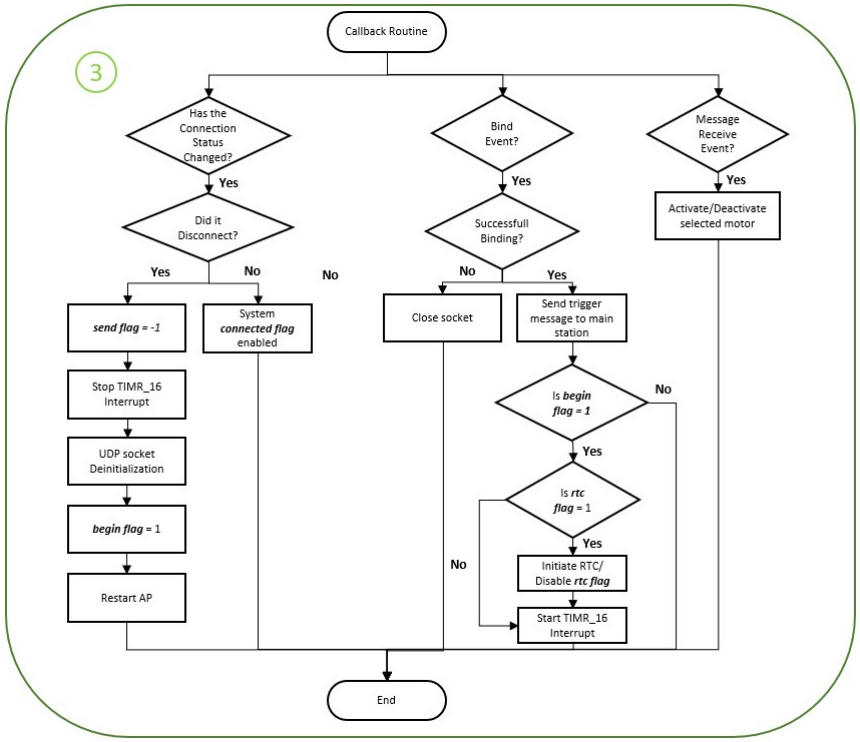

Figure 48: Low-level controller's flowchart for the WiFi module callback routine.

4.3.1.1 UDP Packet

As previously mentioned, the UDP packet sent by the processing station to the main station is composed by the packet index number, the data of each IMU's gyroscope, accelerometer, magnetometer and thermometer, and the message's timestamp. Each of these values was converted to a fixed length sequence of bytes, instead of directly converting it into a string which would lead to a message of variable and bigger size. By having a fixed length message, it is easier to parse the receiving message, and avoids the use of physical separators in the message which would further increase the length of the message. This would be followed by a larger time cost associated with the building and sending of the packet, which could lower the system's performance in terms of sampling frequency. This resulted in a sending packet with a **fixed size of 249 bytes**.

4.3.1.2 Strap Down Integration

SDI is the mathematical process of calculating the rotation, through the integration in relation to time, of the gyroscope's values. Through the processing of the resulting values, it is possible to determine the angular rate of change.

The SDI algorithm, integrated in the XSens products, is designed around the sampling of the gyroscope and accelerometer data at higher frequency rates - namely 1 kHz. By sampling these values at much higher rates, the authors claimed that the accuracy of the orientation estimation is more successfully preserved [154]. This algorithm was validated by estimating the orientation drift, in human motion tracking applications. It was concluded that reducing the SDI frequency lead to an increase in orientation drift. Furthermore, the authors stated that to accurately measure human motion "several hundred Hz SDI rates are needed."

The SDI block was integrated in this project, although only targeting the gyroscope measurements. This is due to the fact that the accelerometer is ideally used to correct the gyroscope readings only when the individual is in a quasi-static state, with the absence of external acceleration [73].

Therefore, to mitigate the effect of the gyroscope' bias, an SDI block was introduced in this system. In Fig. 49, an illustration of the SDI's input and output is illustrated.

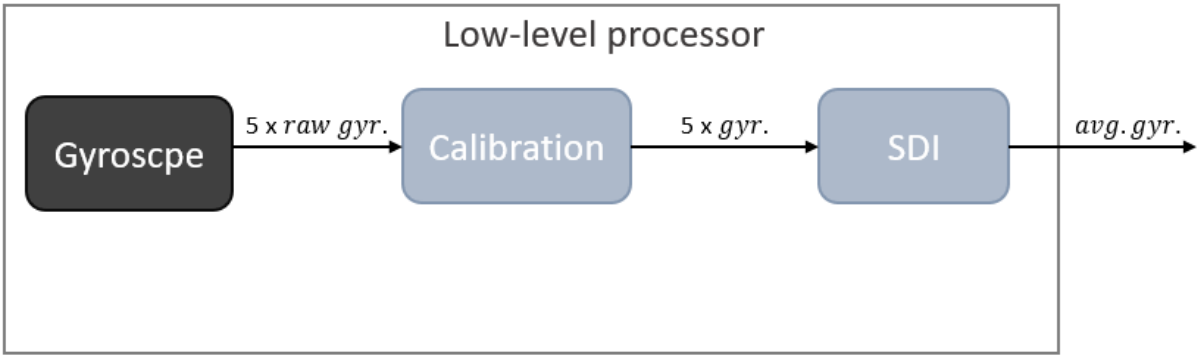

Figure 49: SDI block overview.

However, the SDI block in the low-level processing unit does not output rotations (°) as specified in [154]. It outputs the estimated angular velocity (°/s) that occurred during 5 consecutive frames. To execute this estimation, a trapezoidal integration sequence was implemented.

Trapezoidal Integration Trapezoidal integration is defined as the approximation of a curve, through the division of a curve into several partitions, with each being graphically represented by a trapezoid, as illustrated in Fig. 50.

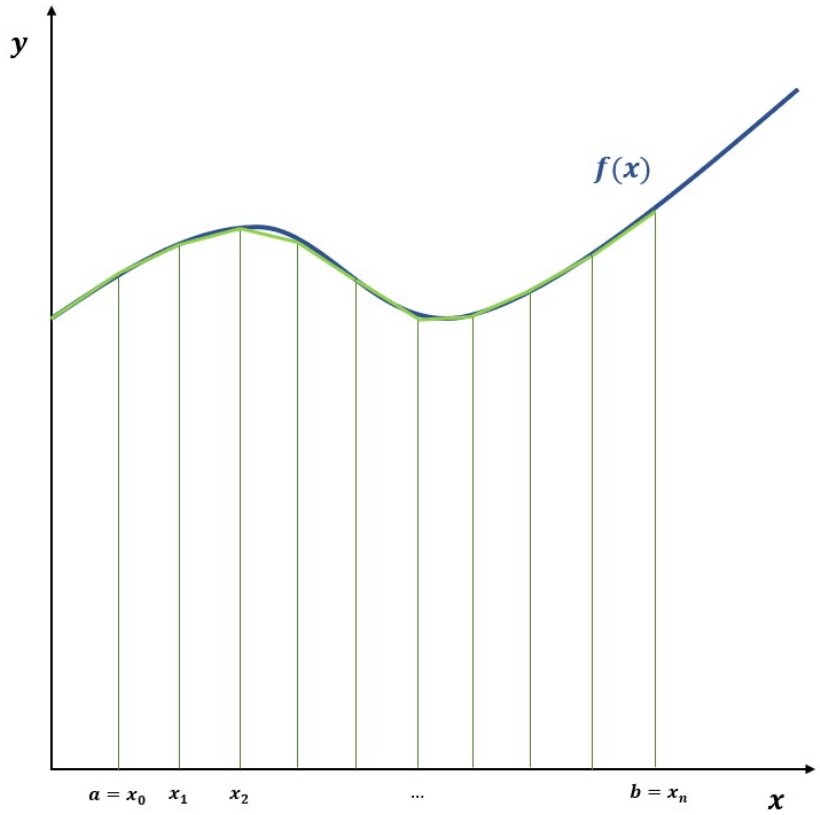

Figure 50: Illustration of a trapezoidal approximation of a curve.

The sum of the area of all partitions is afterwards calculated, obtaining an approximation of the area under the curve, by using the following Eq. 4.1:

$$\int_a^b f(x)\,dx \approx \frac{1}{2}\Delta x(f(x_0)+f(x_1)) + \frac{1}{2}\Delta x(f(x_1)+f(x_2)) + \ldots + \frac{1}{2}\Delta x(f(x_{n-1})+f(x_n)) \quad (4.1)$$

By following the illustration in Fig. 50, a and b are the first and final x-coordinates points, respectively. n is the number of partitions that divide the curve.

4.3.1.3 RTC setup

The Nucleo-144 STM32H723ZG board has an embedded RTC, that is connected to a 32 768 kHz external crystal oscillator. This clock respects the calendar format, including the hour:minute:seconds format. Furthermore, it can count up to the subseconds, which are configurable using the respective prescaler [155].

The timestamp that is sent to the main station, along with the sensors' data, should have count up to the milliseconds resolution, to be easily comparable to the main station's time stamp which has the same format.

This clock is configured using two prescalers: an asynchronous prescaler (7-bit prescaler), and a synchronous prescaler (13-bit prescaler). Using these prescalers, a 1 Hz clock can be obtained to count the calendar unit. According to the datasheet [155], the formula used by the system to calculate the calendar domain clock frequency is 4.2:

$$f_{CK\_SPRE} = \frac{f_{RTCCLK}}{(PREDIV\_S + 1) \times (PREDIV\_A + 1)} \tag{4.2}$$

The f_{CK_SPRE} is the internal clock that manages the calendar format. f_{RTCCLK} corresponds to the Low-Speed External (LSE) oscilator frequency - 32768 Hz. Lastly, $PREDIV\_S$ and $PREDIV\_A$ are the synchronous and asynchronous prescaler values, respectively.

For the subsecond domain - subsecond - a different clock is used, which is only configurable using the asynchronous prescaler. The formula used to calculate the subsecond clock frequency is 4.3:

$$f_{CK\_APRE} = \frac{f_{RTCCLK}}{PREDIV\_A + 1} \tag{4.3}$$

In which the f_{CK_APRE} is the clock frequency used to count the RTC subseconds. To achieve a subsecond resolution of a millisecond, a $PREDIV\_A$ value of 1023 was implemented. Next, to configure the calendar clock frequency to 1 Hz, $PREDIV\_S$ was initialized with a value of 31.

4.3.2 Sensors' Configuration

The sensors Lsm6Dsox and allow to configure their Output Data Rate (ODR) and Full-scale values. For the accelerometer and magnetometer, their ODR and Scale was setup at 1.66 kHz and 16 g, and 80 Hz and 16 G, respectively. This was the configuration applied in the previous iteration. Furthermore, the output with these values was analyzed, whilst the IMU was static, giving out normal values. For the case of the gyroscope, the same analysis was performed. It was seen that the higher the ODR values, the more inconsistent were the values acquired from the gyroscope. These values are displayed in Fig. 51.

From Fig.51 it is possible to observe that for 416 Hz of ODR, the system outputs more stable values, with less variability, while the IMU is static.

For the gyro Full-scale, a bigger value results in a bigger range of values that the sensor can read. However, the gyroscope's sensibility is decreased. So a compromise needs to be made, in which we

Figure 51: Angular velocity static outputs for different ODR configurations.

need sensibility but we cannot saturate the sensor. For this, the values obtained from the experiments performed by the previous iteration were addressed. Due to reported overflow angular velocity data in previous iteration's tests, the full-scale of the gyroscope was selected as 2000 °/s, which is the maximum available scale value.

4.3.3 Sensors' Calibration

Before acquiring real data from the IMUs, a calibration step is required to mitigate errors and susceptibilities present in these sensors. The IMU's main error sources are the bias and scale factor (hard iron and soft iron specifically for the magnetometers), which are compensated by pre-defined calibration routines [64]. **Bias** is the constant offset between the sensor's output and the real value. By subtracting the offset value from the measured data, the bias is removed. **Scale factor error** is the ratio between the measured values and the true values. For the magnetometer specifically, **Hard iron biases** are constant offsets that originate from unwanted magnetic sources, acting like a bias for the magnetometer. **Soft iron errors** are derived from external magnetic fields present in the environment, which affect the local geomagnetic field [156]. If these error sources are left uncompensated, the data acquisition quality will be severely compromised.

4.3.3.1 Accelerometer Calibration

The accelerometer calibration step is comprised of a bench routine in which each sensor is positioned statically on a flat surface, in **six different orientations**, during 5 seconds per orientation [157]. For each position, one of the sensor's axis, x, y or z, needs to be aligned with the gravity vector. This is followed by the acquisition of the maximum and minimum acquired value for each sensor, which are then saved on the processor's firmware [145]. In Fig. 52 it is possible to observe each of the defined orientations.

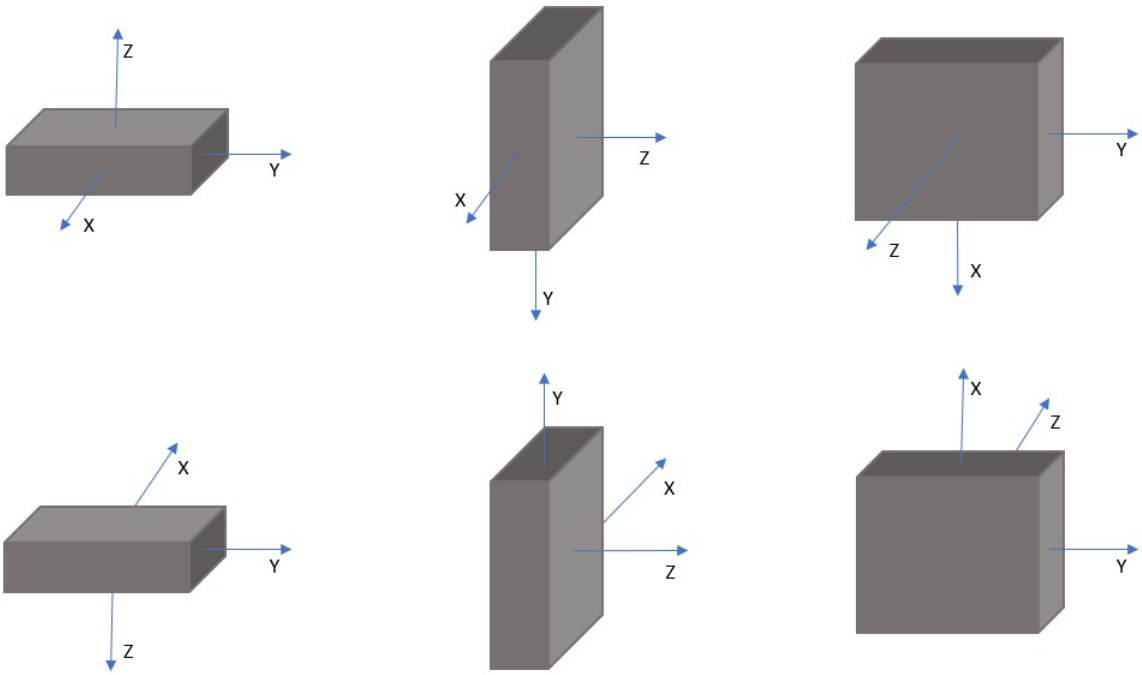

Figure 52: The sensor module positioned in all 6 predefined orientations for the calibration of the accelerometer.

After attaining the maximum and minimum values for each axis, per sensor, Eq. 4.4 is used to calibrate any future accelerometer measurements:

$$calibrated\_value = \frac{(raw\_value - acc_{min}) \times (out_{max} - out_{min})}{acc_{max} - acc_{min}} + out_{min} \tag{4.4}$$

With $calibrated\_value$ being the measured data after applying the calibration constants, and raw_value being the raw measured data. acc_{min} and acc_{max} correspond to the minimum and maximum value acquired during the calibration routine, respectively. Lastly, out_{min} and out_{max} are the minimum and maximum range that the sensor can read, which is -16 g and 16 g, respectively. The function illustrated in Eq. 4.4 is applied for each axis of the accelerometer.

4.3.3.2 Gyroscope Calibration

The system's gyroscope calibration is the only on-body sensor calibration procedure implemented in the system. It is comprised of a five-second period cycle that is activated when the system is initialized. During this period, the user must be static, and performing the n-pose. While in this pose, the sensors are assumed to be static, and the system will read the gyroscope data of each IMU, at the same sampling rate that the system will acquire the same sensors' data during the normal operation cycle. After the five seconds passed, the mean of each sensor's readings is calculated, resulting in their offset. During the normal operation cycle, the respective offset value, calculated during the calibration cycle, is subtracted from each subsequent gyroscope reading, in an effort to minimize the system's bias.

4.3.3.3 Magnetometer Calibration

In contrast to the rest of the sensors, the magnetometer is considered the sensor which are most essential to calibrate, so that they are usable.

To calibrate the magnetometer, the system was fixed onto a plane cardboard cutout, with all the sensors laying horizontally. Afterwards, each IMU's data was acquired sequentially, and continuously for 60 seconds. Each 60 second session started with a participant pointing the respective sensor's x-axis pointing "North". Afterwords, the user would rotate the board holding the sensor along each axis individually. The setup used to calibrate the magnetometer of the MIMUs is illustrated in Fig. 53.

Afterwards, the half-point between the maximum and the minimum acquired measurements is calculated for each axis of each sensor, corresponding to that axis' hard-iron offset. The respective offset is then subtracted for each measured magnetometer value.

4.3.4 Angle Estimation

The purpose of this system is to accurately estimate the upper body joint angles of the user. To achieve this, it was defined that the orientation estimation would be computed using quaternions units, instead of the Roll - Pitch - Yaw configuration. This is due to the fact that quaternions are not targeted by singularities, unlike the alternative. The Roll - Pitch - Yaw rotations would however be used in post-processing to facilitate the orientation interpretation by the user.

4.3.4.1 Fusion Filtering

The selected fusion filter was the SOA ECF, developed by Madgwick [85]. This filter was developed for embedded systems, leading to a possible increasing autonomy of the portable system, and diminishing the processing load of the station. Furthermore, it is **fairly lightweight**, which is ideal, due to the fact that the filter is to be integrated in a neural network, so more heavier filters, like the Kalman Filters, were avoided. Moreover, this filter was directly benchmarked against the well-known and established Gradient-Descent Filter - another lightweight filter - developed by the same author [84], scoring higher in

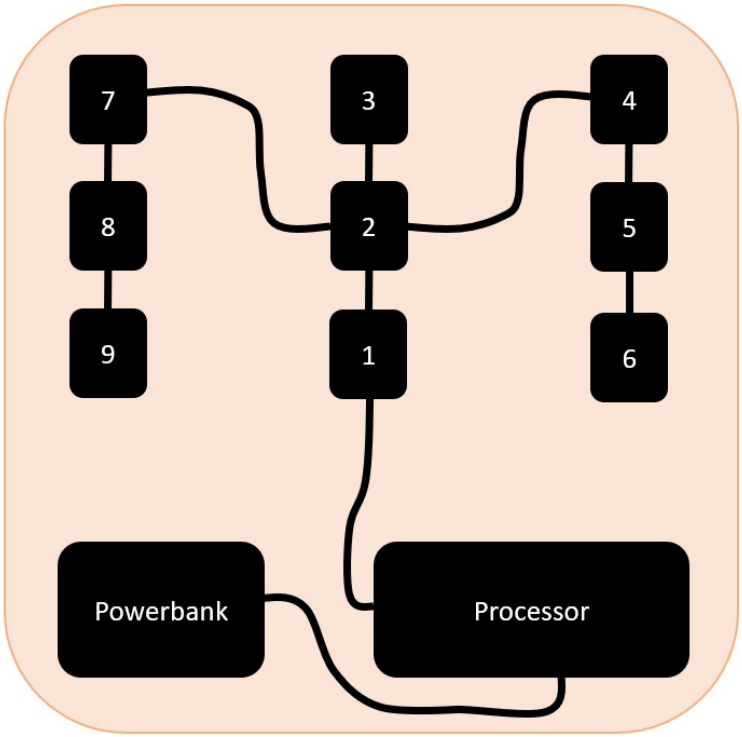

Figure 53: Magnetometer calibration setup, with the sensors, processing station and powerbank fixed onto a plane cardboard.

all performance tests. Compared with the GDA, the ECF has a decoupling mechanism, as the former cannot decouple the Yaw from Pitch and Roll, meaning that the magnetometer readings can affect the orientation estimation in Pitch and Roll. In contrast, the ECF assumes that the rotation in each axis is independent to the other axis. Furthermore, the results obtained in the benchmark tests indicated that the ECF was able to converge to the accurate angle faster, when compared with the GDA [85].

Moreover, the filter is equipped with a threshold-based system, to avoid magnetic disturbances. This system is fairly simple: when the sampled magnetometer values fall off the limits of what can be considered as the interval of values in which the geomagnetic field force can lie on, the sampled values are discarded, and the filter will only use the accelerometer readings as the world reference.

Filter Description This description is based on the description given by the authors of the ECF [85].

The angle estimation is based on the integration of a rate of change (${}^{I}_{G}\dot{q}$) values, resulting in a new orientation, as described in Eq. 4.5:

$$ {}^{I}_{G}q = \int {}^{I}_{G}\dot{q}\, dt \tag{4.5} $$

G and I are the world and IMU reference, respectively, and q is the current estimated orientation.

To approximately calculate the rate-of-change ${}^{I}_{G}\dot{q}$, the gyroscope values can be used, using the previous estimated orientation ${}^{I}_{G}\hat{q}$ as a reference, as shown in Eq. 4.6:

$$ {}^{G}_{I}\dot{q} = \frac{1}{2}{}^{G}_{I}\hat{q} * [0(\omega)]^{T} \tag{4.6} $$

With ω being the angular velocity vector [x,y,z].

Since the integration of the angular values is necessary, and the gyroscope is known for having susceptibilities regarding offsets, the estimated values will be affected by drift. Therefore, to mitigate this cumulative drift, the accelerometer and magnetometer values are used in the filter to correct the Roll, Pitch and Yaw, respectively. These sensors' data are integrated in an error term which is used to correct the gyroscope value at each step. such that:

$$ {}^{G}_{I}\dot{q} = \frac{1}{2}{}^{G}_{I}\hat{q} * [0(\omega - Ke)]^{T} \tag{4.7} $$

With e being the error term, and K its weight. This error term is comprised of two subterms that are derived from the accelerometer and magnetometer vectors. Both subterms result from the cross product between the measured vectors - $\hat{v}_{m(a)}$ for the accelerometer and $\hat{v}_{m(m)}$ and the world reference vectors - gravity and geomagnetic vectors:

$$ e_a = \begin{bmatrix} x \\ y \\ z \end{bmatrix} = \hat{v}_{m(a)} \times {}^{L}v_{r(a)} \tag{4.8} $$

With ${}^{L}v_{r(a)}$ being the gravity vector in the local body frame, as $v_{r(a)}$ is defined by:

$$ v_{r(a)} = [0, 0, -1] \tag{4.9} $$

And by applying Eq. 4.10, the reference frame is applied to the local body:

$$ {}^{L}v_{r(a)} = q \cdot v_{r(a)} \cdot q^{-1} \tag{4.10} $$

With $q = \left[q_w, q_x, q_y, q_z\right]$.

$$ {}^{L}v_{r(a)} = \begin{bmatrix} 2(q_x * q_z - q_w * q_y) \\ 2(q_w * q_x + q_y * q_z) \\ 2(q_w * q_w) - 1 + 2(q_z * q_z) \end{bmatrix} \tag{4.11} $$

For the magnetic error term e_m, the reference geomagnetic vector, $v_r(m)$, is represented by the magnetic west:

$$ v_{r(m)} = [0, -1, 0] \tag{4.12} $$

Followed up by the applying Eq. 4.10 substituting $v_{r(a)}$ by $v_{r(m)}$. Leading to:

$$^{L}v_{r(a)} = \begin{bmatrix} 2(q_x * q_y + q_w * q_z) \\ 2(q_w * q_w) - 1 + 2(q_y * q_y) \\ 2(q_y * q_z - q_w * q_x) \end{bmatrix} \tag{4.13}$$

Furthermore, due to the necessity of guaranteeing that the magnetic error term is perfectly orthongonal to the gravity vector, a cross product between the measured magnetic vector and the accelerometer vector is executed, as illustrated in Eq. 4.14:

$$e_m = \begin{bmatrix} x \\ y \\ z \end{bmatrix} = |\hat{v}_{m(a)} \times \hat{v}_{m(m)}| \times {}^{L}v_{r(a)} \tag{4.14}$$

Therefore, in an ideal situation the error term is defined as:

$$e = e_a + e_b \tag{4.15}$$

This is true when:

$$\hat{v}_{m(m)} > \hat{v}_{m(m)min} = 24\,\mu T \ \wedge\ \hat{v}_{m(m)} < \hat{v}_{m(m)max} = 66\,\mu T \ \wedge\ \hat{v}_{m(m)} > 0 \tag{4.16}$$

$\hat{v}_{m(m)min}$ and $\hat{v}_{m(m)max}$ are the minimum and maximum values considered to be the possible values of intensity of the geomagnetic fields. The magnetic interval values were based on an observation made by the Portuguese Institute for Sea and Atmosphere [158]. If the measured magnetic values' norm fall outside of this interval, then the magnetic measurement is discarded, with the error term being only dependent of the accelerometer measurements:

$$e = e_a \tag{4.17}$$

As long as:

$$\hat{v}_{m(m)} > 0 \tag{4.18}$$

Furthermore, in regard to the error term gain, K, its value depends on the following conditions:

$$Condition1 : T < T_{init} \tag{4.19}$$

$$Condition2 : T > T_{init} \tag{4.20}$$

With T and T_{init} corresponding to the current operation time and initialization time. The initialization time is the period in which the system is considered to be in an initialization mode. If the system is in this condition - Condition 1 - the filter's gain can be calculated by:

$$K = K_{init} * \frac{T_{init} - T}{T_{init}} * (K_{init} - K_{norm}) \tag{4.21}$$

T_{init} is the initialization period duration, in seconds, which correspond to 3 seconds. Moreover, $K_{init} = 10$ is the initialization gain. Both of these values were recommended by the implementation of the filter's authors.

If the system is operating during Condition 2, then the gain K is:

$$K = K_{const.} \tag{4.22}$$

With $K_{const.}$ being a constant value, defined when the filter class is created. This value was defined as 0.5, which is the recommended value provided by the authors of this filter [85].

This fusion filter was tested with the previous system. In Fig. 54 is depicted the motion tracking resulted from the ECF, for two uni-joint motions.

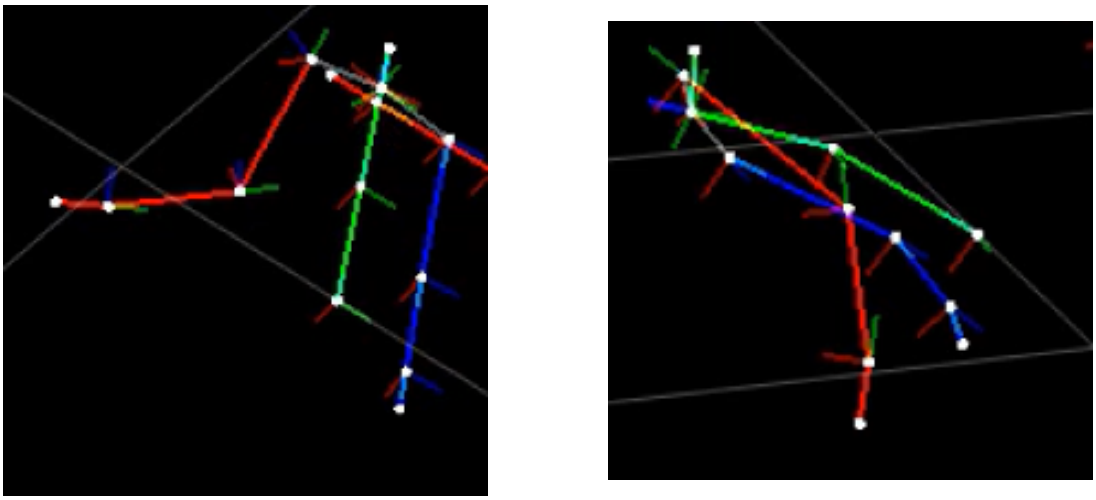

(a) (b)

Figure 54: Motion tracking resulted from the ECF for a) elbow flexion and b) trunk flexion.

4.3.4.2 Sensor-to-Segment Calibration

In the new system, a sensor-to-segment calibration routine was added. It is composed of three available individual calibration routines, which can be selected. Fig. 55 represents the

The manual calibration sequence is based on the use of pre-calculated quaternion rotations on the sensor data, to correct the sensor orientation in regard to the North-West-Up (NWU) reference frame. This calibration is not ideal since it is impossible the user places the sensors in the same exact position each time the system is used, making this calibration sequence inflexible.

The simple static calibration sequence is based on the user maintaining the n-pose while the system is initializing. During this period, the gravity frame is used to correct the Roll and Pitch of each of the sensors' data, by using the acceleration data. If the rotation quaternions are know, they are applied to approximate

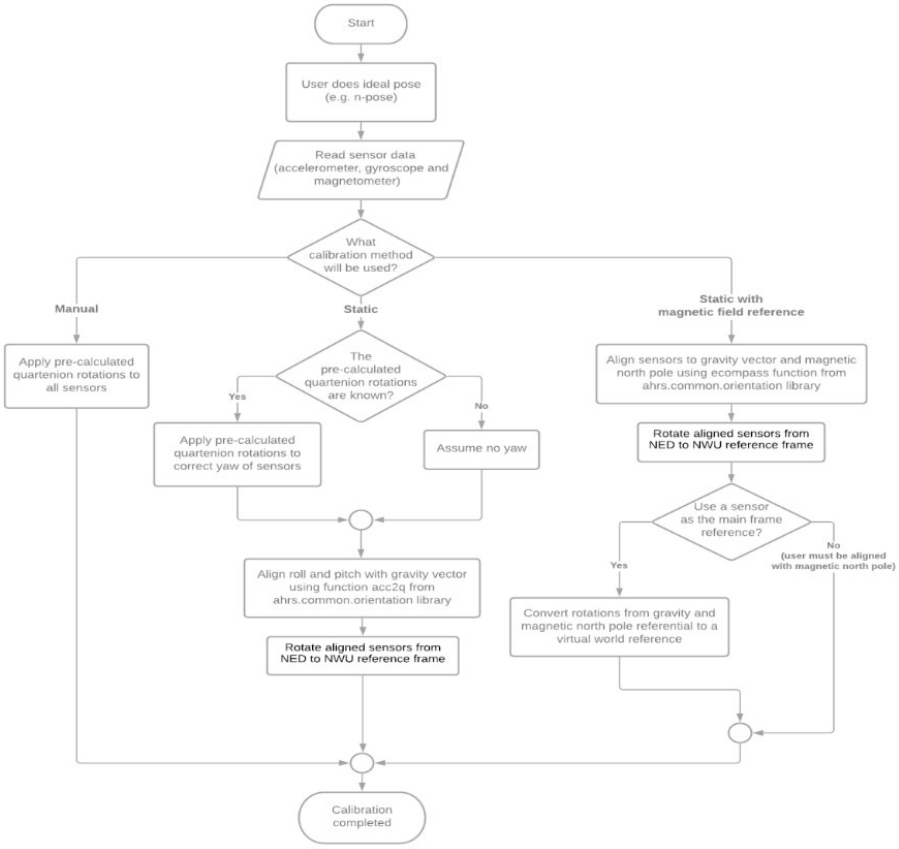

Figure 55: Sensor-to-segment calibration overview.

the sensors' orientations to the world reference frame. Afterwards, the gravity vector is used to correct the Roll and Pitch of each IMU. In this calibration, the Yaw cannot be estimated, and it it therefore, not corrected and it is assumed that it is aligned with the world. This method is more flexible in regard to the manual calibration, but it still presents inflexibility on the Yaw axis, being dependant on the pre-calculated quaternion rotations.

Lastly, the magnetic static calibration uses the gravity vector to correct the Roll and Pitch of the sensors' data in regard to the world reference, and also the magnetic north to correct the Yaw, using the magnetometer's data. Since it covers all three axis, it is not dependant on the manual quaternion rotations, and therefore does not apply them to the sensors' data. This calibration sequence assumes that the user is performing the n-pose while perfectly aligned to the magnetic north. This may be somewhat difficult to perform, so optionally the rotations of all sensors can be aligned with the Yaw of one reference sensor. This is the most flexible calibration sequence.

5

Results & Discussion

5.1 System Characterization

Several validation bench tests were executed to evaluate if the system conforms with the designated technical requirements. Furthermore, the wearable's physical characteristics, namely its weight and the dimensions of the different units, is also addressed, since one of the goals was towards the system's miniaturization.

5.1.1 System Timings

To guarantee that the processing unit was able to handle the system's timing requirements, as to not compromise the real-time nature of the prototype, the different processes were analyzed in the oscilloscope. All of the systems processes regarding the reading of the IMUs data and the processing and dispatch of the data to the main station were analyzed using an oscilloscope. To do this, before each respective process, a GPIO pin was set to HIGH before its immediate execution, and then set to LOW immediately afterwards. The biggest restriction for the system's sampling frequency and output frequency is the time cost regarding the two main active algorithm blocks during the system's operation: the sending block, and the interrupt block.

The sending block is composed by the SDI block, building and sending of the package, and the WiFi module event handler. Each of these processes were analyzed individually, and compared against the total duration of the sending block. Fig. 56 displays the time required for each of the sending block's processes, and for the entire sending routine.

To verify about the time needed for the processor to execute the SDI and the package building function, they are presented individually in Fig. 57.

From Fig. 56, it is possible to observe that the entire sending sequence is mostly occupied by the sending function. The entire sending routine takes about 1,58 ms, and the sending function around 1.55 ms. With the disabling of the UDP sending event, the WiFi handler does not contribute to the processing load. Furthermore, from Fig. 57 it is possible to conclude that the building of the data package

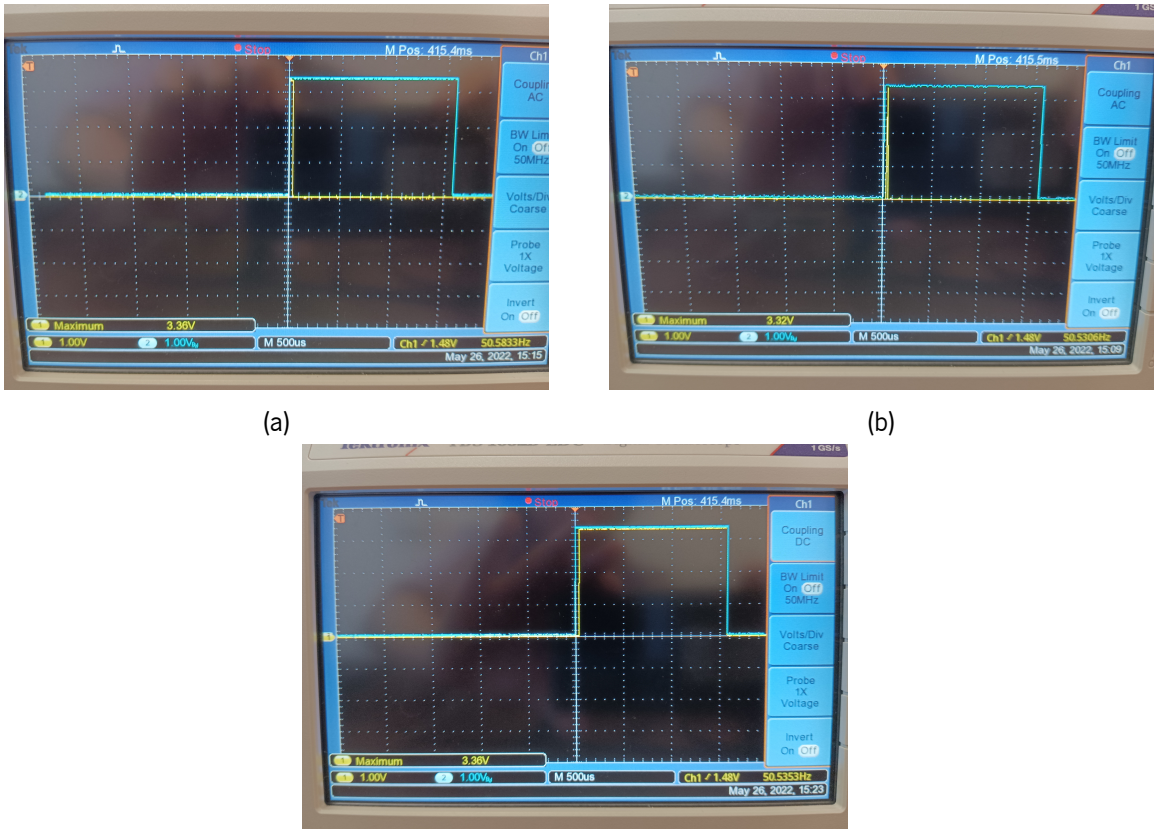

Figure 56: Duration time of each of the sending block functions (yellow), with the total block time duration displayed as comparison (blue). a) SDI, b) building of the package and c) sending function.

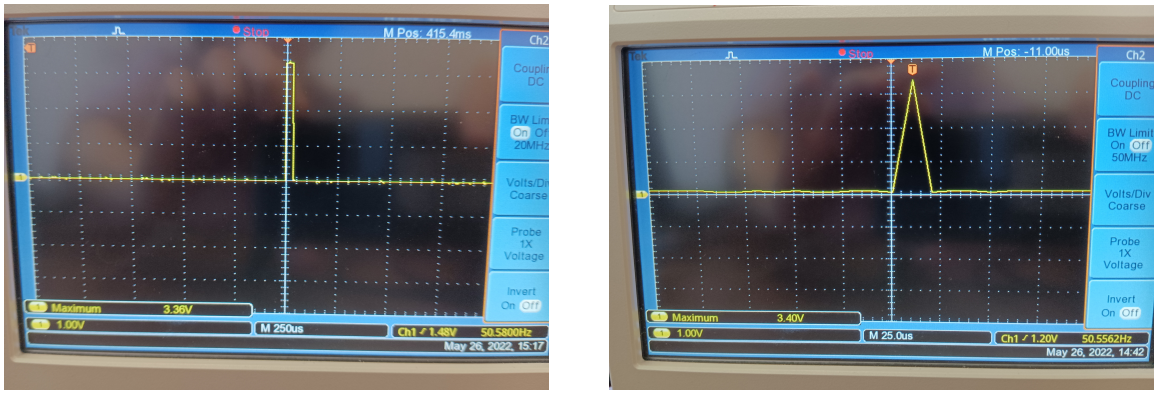

Figure 57: Duration time of the a) SDI and b) package building.

takes around 20 μs to execute, presenting almost no computational load. Lastly, the SDI block needs approximately 35 μs to be performed.

5.1.1.1 Interrupt Time

The interrupt subroutine is comprised of at least all of the sensors' angular velocities readings. Furthermore, during an interrupt, three of the sensors' accelerometer, magnetometer and thermometer values can also be acquired. These are the most time-consuming processes of the interrupt routine. For means of comparison, both the timings required for one gyroscope reading, as well as all 9 gyroscope readings, are depicted in Fig. 58. Furthermore, also in Fig. 58 is showcased the time needed for the acquisition of three of the sensors' accelerometers, magnetometers and thermometers.

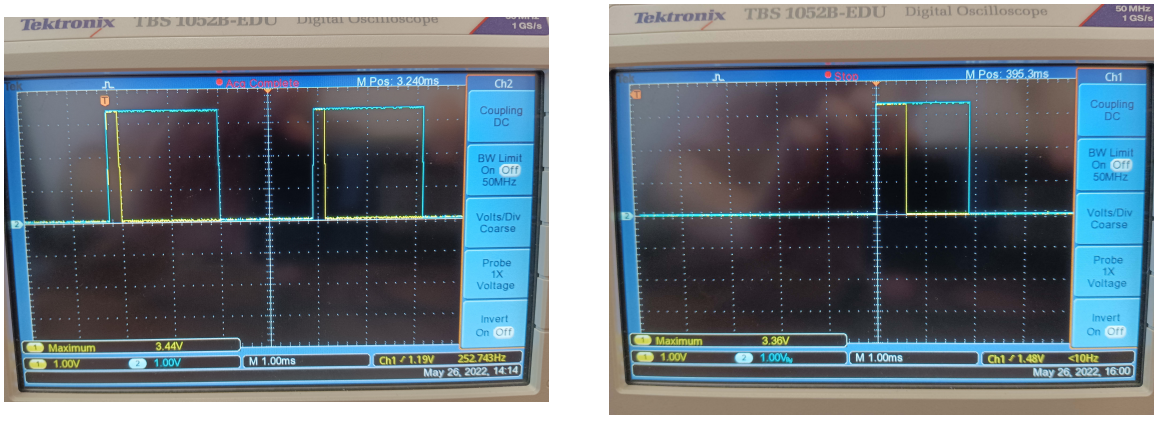

(a) (b)

Figure 58: Duration time of the a) SDI and b) package building.

From Fig. 58, the time needed to acquire the data of one IMU's gyroscope can be observed, which is close to 250 μs. From the same figure, it is also possible to conclude that approximately 2.25 ms are needed to acquire all of the gyroscopes' data. Moreover, to acquire the accelerometer, magnetometer and thermometer data of one IMU and all of the IMUs, approximately 600 μs and 1.8 ms are needed, respectively.

To evaluate the real period of each interruption, the process to read all of the gyroscopes and three of the IMUs' accelerometer, magnetometer and thermometer was visualized. In Fig. 59 the result of this test can be observed.

From Fig. 59, it is possible to determine that the processing system takes about 4.1 ms to successfully acquire all of the gyroscopes' data, including the data of three accelerometers, magnetometers and thermometers. For a frequency of 250 Hz, each interrupt would need to be inferior to $4ms$ worth of processing time to safely acquire the data at a constant frequency. For 240 Hz, the interrupt period is equivalent to $\approx$ 4,17 ms which is approximate to the real interrupt's period. **This was selected as the maximum sampling frequency of the system.**

After changing the values of the sampling frequency, the duration of all consecutive interrupt times was analyzed. Fig. 60 displays the time (in milliseconds) it takes to perform a cycle of 5 consecutive

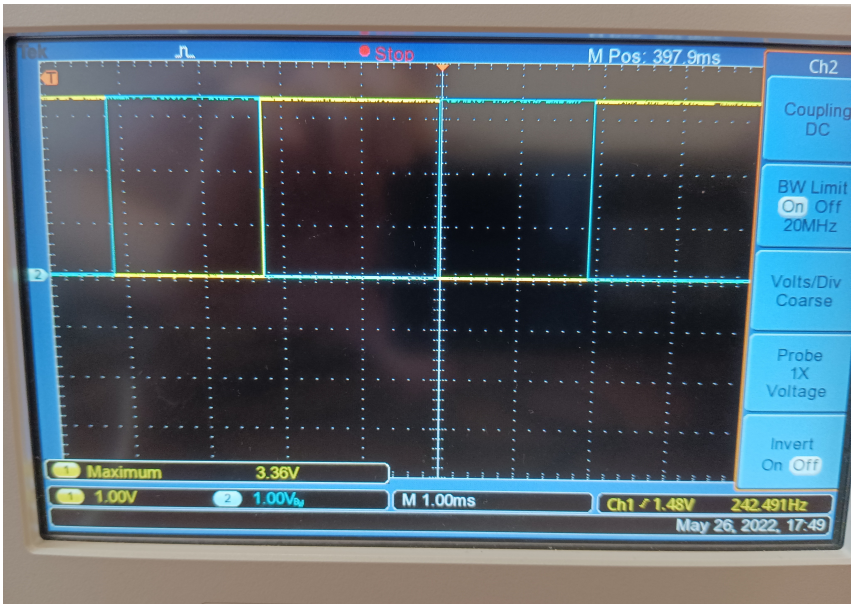

Figure 59: Overview of the time needed to perform the reading of all gyros (yellow) and of three IMUs (blue) in an interrupt cycle.

interruptions, with the sending block total time being displayed aswell, to guarantee that it can be executed in each of these cycles.

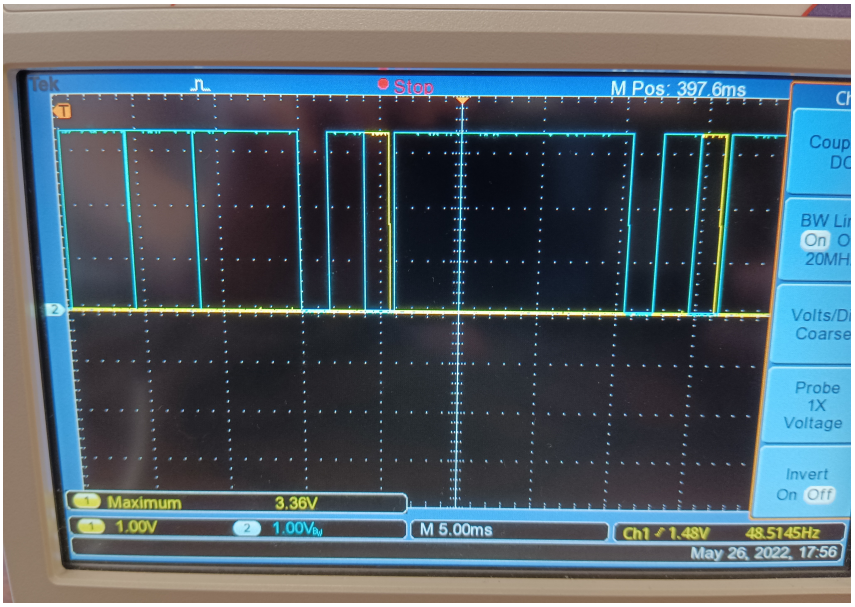

Figure 60: Overview of the time of the interrupt cycles (blue) and the sending block (yellow) between 5 interrupts.

The data acquired from these tests allowed to conclude that the system was not able to consistently sample the IMUs' data at a frequency higher than 240 Hz, with an **output frequency of 240 / 5 = 48 Hz**. This output frequency is still above the minimum requirement of 35 Hz which is the frequency of the

control algorithms in the Human-robot collaboration framework that will integrate this system. Through these results, we can conclude that in a 1-second window, the Atwinc1500 is operating in the sending mode during $48 \times 1 \times (1550 \times 10^{-6}) = 0.0744$ s. The rest of the time, the module is mostly operating in standby mode, which is approximately $1 - 0.0744 = 0.9256$ s, in a 1-second window. With the respective power consumption in each operation mode, one can extrapolate that the WiFi module consumes around $(0.0744 \times 268 + (380 \times 10^{-3}) \times 0.9256) \times 8 \approx 162.33$ mAh in an 8-hour session [153].

5.1.2 Distance Tests

One of the requirements for the system is the guarantee that it can safely operate at a range of distances from the wearable processing unit to the main station. The test was performed in an open-spaced room, with no obstacles, and lack of electronic interferences. In fact, the app "WiFi Analyzer" was used to identify the existing networks and available channels in the room where the experiments took place. From the app, it was possible to observe that 11 channels were available, and 6 WiFi networks were operating in the room. A personal laptop running Ubuntu in VMware (VMware, Palo Alto, USA) was used as the main station. To perform this test, the system was fixed on a planar table which was then placed on several marks which represented different distances in regard to the main station. The distances were 0.5, 1.0, 2.0, 3.0, 4.0, 5.0, 6.0, 7.0 and 8.0 m. The last value was the maximum distance possible in the room without physical obstructions. The evaluated metrics were namely the real system's frequency, the percentage of corrupted packages and of packet loss and the Round-Trip Time (RTT). The RTT was tested individually in regard to the other metrics. The different metrics were computed as the mean (and standard deviation) of all the trials per distance. For each distance, 3 trials were conducted, with 5 minutes per trial. Table 12 and Fig. 61 displays the overall communication results obtained for each distance.

Table 12: Influence of the distance between the main station and the low-level processing unit on the wireless communication performance.

Distance (m)	**Frequency (Hz)**	**Packet loss (%)**	**Data Corruption (%)**	**RTT (ms)**
0,5	48,50 (± 0,91)	0,00	0,00	35,37 (± 8,05)
1	48,45 (± 0,96)	0,00	0,00	33,38 (± 6,85)
2	48,49 (±0,96)	0,00	0,00	33,50 (± 7,10)
3	48,48 (± 0,94)	0,00	0,00	33,44 (± 6,56)
4	48,47 (± 0,94)	0,00	0,00	34,33 (± 7,98)
5	48,20 (± 2,67)	0,46	0,00	33,32 (± 6,49)
6	48,11 (± 4,11)	0,65	0,00	34,21 (± 7,22)
7	48,49 (± 1,14)	0,02	0,00	33,41 (± 6,58)
8	48,43 (± 1,79)	0,09	0,00	34,38 (± 6,96)

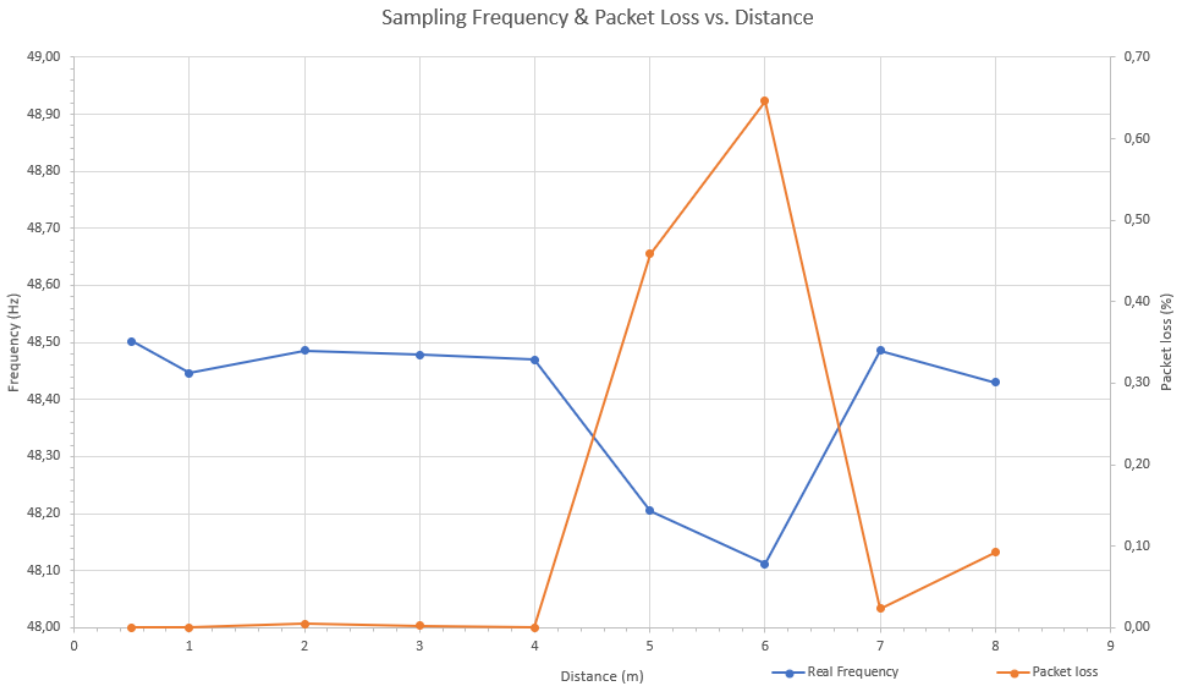

Figure 61: Real sampling frequency and packet loss in regard to the distance between the main station and the processing unit.

From Table 12, it is possible to observe that, for all distances, there was no presence of data corruption. Furthermore, the obtained sampling frequency was largely stable throughout all of the tests, reaching a maximum of 48.50 Hz at a distance of 0.5 m, and a minimum of 48.11 Hz. Regarding the packet loss, it was observed that it was null up until the 5 m of distance between the main station and the processing unit. The packet loss reached a maximum value of 0.65 %, for a distance of 6 m.

To obtain the system's RTT in these tests, a 249 byte word (simulating a real data message during the system's normal operation) was sent from the main station to the processing unit. Afterwards, the processing station would then re-transmit this message back to the main station. The time it took to send and receive back the ping message was then then acquired, resulting in the RTT value. The RTT is not equivalent to the system's latency, since latency addresses the one-way communication delay. To estimate the system's latency, we divided the resulting RTT values by 2, and removed the sending function time duration, which was determined in the "System Timings", since the size of the message correspond to the same 249 bytes. By doing this, the approximated latency values obtained for the maximum and minimum acquired averaged RTT results, correspond to approximately 17,32 ms and 16,3 ms, respectively. These values are in accordance with the latency requirements, which determined that, ideally, the latency of the system should be inferior to 19 ms. However, the resulting standard deviation values were relatively substantial, reaching a maximum of 8,05 ms at a distance of 0.5 m from the main station.

When comparing the system's wireless communication performance with the previous model [29], it is possible to conclude that the former achieves a much more stable wireless communication setup.

Since the previous iteration was not tested for more than 4 meters, it is impossible to make a full distance comparison. In terms of packet loss, the previous version constantly showed a packet loss prevalence > 1.5 %, reaching a maximum of 3.4 % at a distance of 4 m. In turn, the newer version was improved in this aspect, not having any packet loss at low distances (lower than 4 meters), and achieving a complying packet loss value of $0,65$ % at 6 m. This value is inferior to the 1 % defined, conforming with the packet loss requisites. The prevalence of data corruption was 0 % in both systems, and the stability of the packet dispatch frequency was superior in the new iteration, for different distances. The obtained values are in conformity with the specified technical requirement for each analyzed distance. Regarding the obtained latency values, it is not possible to make a fully objective comparison between both systems, since the latency measurement method was different, so no conclusions can be assessed for this metric. Nevertheless, the estimated latency for the current system was consistent between the different analyzed distances. Ideally, the system's latency should be measured with a real-time clock synchronized with the world's real-time clock at a millisecond resolution, which is possible on the main station. However, this alternative was deemed not possible, or at least extremely complicated to integrate into the STM processing unit, due to the C libraries regarding the real-time clock not being entirely compatible with the STM programming framework. Nevertheless, the obtained estimated latency values were between 17,32 ms and 16,3 ms, which conform with the ideal requirement of 19 ms.

5.1.3 Interference Tests

To infer the effect of obstructions like walls and other wireless interferences on the wireless communication performance, namely on the sampling frequency, packet loss, data corruption and latency, a test protocol was devised. In this protocol, the main station and the processing unit were separated by 0.5 m, with a 0.35 m thick concrete wall in the middle of both units. Three 5 minutes trials were performed, with the processing unit static on a table. Along with the wall, the environment where the tests were performed had a much higher level of wireless interference. Through the use of the app WiFi Analyzer, it was possible to verify that 31 networks were operating in the room, accounting for a much larger interference level, compared with the previous tests. The results obtained from this test are displayed in Table 13, as well as the result obtained from the tests "Distance Tests", for 0.5 m of distance to serve as comparison.

Table 13: Influence on the interference of walls and other wireless interferences on the wireless communication's performance.

Interference	Frequency (Hz)	Packet loss (%)	Data Corruption (%)	RTT (ms)
W/ Wall	48,38 (± 1,51)	0,06	0,00	33,67 (± 8,03)
W/o Wall	48,5 (±0,91)	0,00	0,00	35,37 (± 8,05)

It is possible to observe from Table 13, that a rise in packet loss of around 0.06 % was obtained in the interference test, in regard to the previous test, for the same distance between the main station and

the processing station. The rest of the performance metrics seem to have maintained regardless of the exterior interferences. This leads to the conclusion that the interference originated from the obstruction of a concrete wall did not significantly affect the performance of the wireless communication setup. This leads to the conclusion that, in the context where the tests were performed and for a distance of 0.5 m between both processing stations, the system conforms with the predefined technical requisites. Once again, the results obtained suggest that the wireless communication performance of the new system was significantly improved compared with the previous version of the Ergowear.

5.1.4 Power Supply Influence

The battery autonomy of the new iteration was tested in two different situations. The first one was with the system operating in monitoring mode, i.e., with the system solely acquiring and sending data to the main station. The second one was representative of the biofeedback mode, i.e., with the system operating in by activating/deactivating the vibrotactile motors in a 1 second period, in addition to the monitoring mode. Both tests consisted of a data acquiring session, which ended when the battery of the power supply would run out. Furthermore, the packet loss, percentage of corrupted data and the acquired frequency was analyzed after each hour, to analyze the influence of the input voltage on the WiFi communication robustness. The system was setup on a table, with a distance off 0.5 meters between the processing unit and the main station. Table 14 displays the autonomy duration, in hours, of the system, in each test.

Table 14: Autonomy tests results.

Trial	Autonomy (h)
Monitoring mode	23h30
Biofeedback mode	15h30

In Table 14 it is possible to verify that the system was able to achieve 23h30 of autonomy while only reading and sending data to the main station, and 15h30 while performing the tasks of the previous trial and also activating/deactivating the vibrotactile sensors in a 1 second period.

Regarding the system's autonomy, as seen is Table 14 the current version of the wearable was successful in reducing the wearable's current consumption significantly. The previous iteration was not able to operate in monitoring mode for 8 hours straight with a 13400 mAh power supply, reaching a maximum of 7h20 of autonomy. In contrast, the new system was capable of surpassing this requisite, reaching 23h30 with the same power supply, which leads to a lower power consumption. This also leads to a possibility in miniaturizing the power supply unit, in dimensions and weight. Furthermore, this increase in energy efficiency results in reduced heat accumulation, also increasing the overall wearability of the system. Moreover, it was possible to observe that the wireless communication between the main station and the low-level processing unit is stable overtime, and overall unaffected by the power supply's charge

and voltage, which guarantees that the system conforms with the technical requirements for the duration of an 8 hour operating session, as displayed in Fig. 62.

From this test, it is also possible to extrapolate the current consumption of the system during monitoring mode, which is displayed in Eq. 5.2:

$$Current = 14300/23,5 = 570,21\ mA \tag{5.1}$$

Which, in a period of 8 hours, corresponds to approximately 4561,68 mAh.

The same process was applied to estimate the current consumption during feedback mode:

$$Current = (14300/15,5) * 8 = 922,58 * 8 = 7380,65 mAh \tag{5.2}$$

From these results, it is possible to conclude that the current power supply is overdimensioned, in terms of capacity, for the current system. Therefore, to reduce the system's total weight and the unit's dimensions, a new power supply with reduced capacity can be integrated into the wearable. **The proposed powerbank is the Bluehive 5300 mAh** with 88x41x21 mm (75768 mm^3) and 120 g. In comparison with the previous powerbank, a reduction in weight and dimension of around 53,8 % and 52,6 %, respectively, is concluded for the power supply unit. Although the capacity of this powerbank would not be able to perform an 8 hour session with the feedback motors activating every 1 second, it is more than adequate for the monitoring operation mode of the system. Since the motors are not activated periodically but only to correct the user's posture, they are not expected to consume a lot of the system's current. Even so, a second powerbank of the same type can be used to substitute the drained one.

Furthermore, the first autonomy test, which was executed whilst in monitoring mode, also served to test if the wireless communication setup is stable along the operation time. These metrics, namely mean sampling frequency, packet loss and data corruption were analyzed after each hour of operation time. The test was performed in the same environment as the "Distance Tests", with lack of electromagnetic interference, and with a distance between the processing unit and the main station of 0.5 m. The results obtained from this test are displayed in Table 15. Fig. 62 gives an overview of the real sampling frequency for each hour of operation until the STM powers down.

From Table 15 and Fig. 62, it is possible to observe that the system did not present any packet loss data corruption along the 23 hours of operation. Moreover, the system's sampling frequency maintained largely constant during the session, revolving around the 48,55 ms, reaching a maximum of 48,60 ms in the 2nd hour of operation, and a minimum of 48,51 ms. From this, we can conclude that the system is capable of consistently operate for 8 hours straight, at least at a close distance in regard to the main station. Furthermore, it is relevant to refer that the values for the packet loss, sampling frequency and data corruption maintained within the specified requirements, for the total duration of the tests.

Table 15: Real sampling frequency, in Hertz, packet loss, in %, and Data corruption, in %, of the wireless communication setup vs. time, in hours.

Time (h)	Frequency (Hz)	Packet loss (%)	Data Corruption (%)
1	48,58 (±0,75)	0,00	0,00
2	48,60 (±0,73)	0,00	0,00
3	48,59 (±0,74)	0,00	0,00
4	48,59 (±0,74)	0,00	0,00
5	48,58 (±0,75)	0,00	0,00
6	48,58 (±0,75)	0,00	0,00
7	48,58 (±0,75)	0,00	0,00
8	48,57 (±0,76)	0,00	0,00
9	48,57 (±0,75)	0,00	0,00
10	48,57 (±0,76)	0,00	0,00
11	48,56 (±0,77)	0,00	0,00
12	48,56 (±0,77)	0,00	0,00
13	48,56 (±0,77)	0,00	0,00
14	48,56 (±0,77)	0,00	0,00
15	48,55 (±0,78)	0,00	0,00
16	48,52 (±0,80)	0,00	0,00
17	48,51 (±0,82)	0,00	0,00
18	48,52 (±0,81)	0,00	0,00
19	48,52 (±0,80)	0,00	0,00
20	48,52 (±0,81)	0,00	0,00
21	48,52 (±0,81)	0,00	0,00
22	48,51 (±0,82)	0,00	0,00
23	48,51 (±0,82)	0,00	0,00

5.1.5 System Hardware and Physical Comparison

The current Ergowear version was compared in terms of hardware and physical properties with the previous iteration and the XSens Link, which is the wired version of the XSens MVN line [123]. The result of this comparison are displayed in Table 16.

Analyzing the components individually, following the information illustrated in Table 16, it is possible to observe that the current system weighs 124 g less than the previous iteration. This corresponds to a decrease of around 10 % in weight. However, the current system does not fully conform to the wearable's weight requirement, which corresponds to 1 kg. It is important to note that most of the wearable's weight is close to the user's centre of mass (hip area), and uniformly distributed in that area, being more comfortable to the user. Moreover, both the power supply unit and processing unit can be miniaturized. Due to the oversized capacity of the battery unit, the proposed alternative can reduce the weight of the wearable

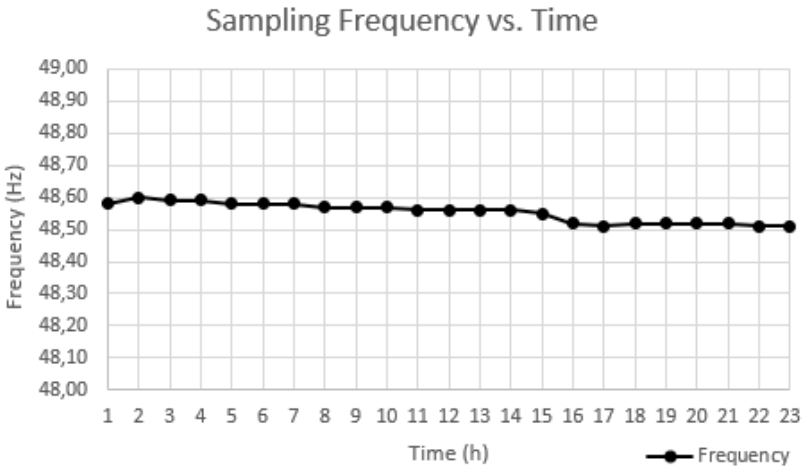

Figure 62: Real sampling frequency vs. operation time.

Table 16: Hardware comparison between the previous iteration of the ergowear with the current one, as well with the XSens Link.

	Category	Previous	Current	MVN Link
Weight (g)	Intermediary Modules	19	15	10
	Extremity Modules	11	12	
	Master Module	210	189	150
	Power Supply	260	137	-
	Wearable	356	399	485
	Full System	1254	1130	1130
Dimensions (mm)	Intermediary Modules	45 x 35 x 19 (29925 mm^3)	52 × 22 × 13 (14872 mm^3)	36 x 24.5 x 10 (8820 mm^3)
	Extremity Modules	31 x 35 x 19 (20615 mm^3)	41 × 22 × 13 (11726 mm^3)	
	Master Module	95 x 73 x 45 (312075 mm^3)	146 × 92 × 37 (496984 mm^3)	160 x 72.5 x 25 (290000 mm^3)
	Power Supply	100 x 80 x 20 (160000 mm^3)	100 x 80 x 20 (160000 mm^3)	-
Current Consumption (mA)		1 827,27	570,21	305,26

to around 1 kg, **respecting the weight requirement**. Also, the processing unit is composed by a development board and a custom-made PCB on the bottom. Ideally, this processing unit plus the contents on the PCB would be integrated in the same PCB, reducing its dimensions and weight. Specifically, for the sensor modules, the new iteration presented a reduced 4 g weight for the intermediary modules, which presents a 21 % in weight reduction. Nevertheless this weight can be further reduced, as observed from

the XSens Link MTx sensor weight. This weight value can be further improved by removing the screws and bolts used to close the casings. Although these components are a solid and robust solution to close these casings, they present a total weight of around 2 g, respectively. As an alternative, snaps can be used, dismissing the use of exterior parts to close the casings, whilst maintaining the accessibility of the interior. In terms of dimensions, the new modules are significantly smaller, presenting 14872 mm^3 for the intermediary modules and 11726 mm^3 for the extremity modules. When compared with the previous version (29925 mm^3 for the intermediary modules and 20615 mm^3 for the extremity modules) a reduction of around 50 % of size was achieved. Furthermore, a significant reduction of height was achieved, which is the most valuable dimension regarding wearable system [143]. However, the XSens Link counterpart presents smaller dimensions in all sides except in width, having 8820 mm^3. To further reduce the current sensor modules' dimensions, the sensor's board should be custom-made and not a breakout board. Furthermore, the height of the intermediary modules is limited by the integrated strain reliefs, which in turn were dimensioned by the cabling diameters. The extremity modules have the same height of the intermediary counterparts due to standardization, so they could be made smaller.

Regarding the power supply, no information could be gathered from the XSens Link's battery. Comparing the current iteration with the previous one, the power consumption was reduced by more than three times in regard to the previous model's value, without counting the vibrotactile motors. This was made possible specially due to the effective change in processing unit. Nonetheless, the MVN Link consumes 46 % less than the Ergowear. Therefore, improvements can be made in order to reduce the Ergowear current consumption. This could be tackled specially in the processor's unit strategy. An alternative could be the integration of Application-Specific Integrated Circuit (ASIC) units in each of the sensor modules, that would be dedicated in performing the SDI block for the respective sensor, being a more energy efficient instead of using the host processor to execute this block [154]. This would also reduce some of the computational load of the main processor, which would receive the data at a much less rate, and be responsible for only performing the sensors' calibration, and sending the data to the main station. This leads to the selection of a more low-budget, and not so high performance processor, which could miniaturize the processing unit. Furthermore, this strategy could lead to a higher sampling frequency to acquire more detailed data, namely from the gyroscope, possibly reaching the stipulated 1000 Hz used by the XSens [123].

Moreover, regarding the suit's weight, it is possible to observe that in the new iteration weights 43 g more than the previous version. Nevertheless, it is $\approx 18\%$ lighter than the XSens version.

In terms of the wireless communication performance, except for the prevalence of packet corruption, which is null in both systems, and the latency, which is around the same value for both iterations, the new version achieved better results in all metrics, in the performed tests. This was namely in terms of packet loss and sampling frequency consistency. Moreover, the new system corrected some limitations of the previous system, such as the fact that it did not conform fully to the packet loss rate requirement, accepted for the past version [29]. The values obtained for the previous system are described in [29]. This leads to the conclusion that the wireless communication setup in the new iteration is a direct improvement in regard to the previous one.

Lastly, the assembly of the wearable led to a cost of around 400 €, excluding the suit, which was produced and custom-made by Clothius, and the powerbank. This is lower than the price standard setup by the work in [63], which inspired to define the cost requirement regarding the wearable. Furthermore, it is a low-budget alternative to the commercial systems described in the State of Art, in which the cheapest commercial costed 2399 €, belonging to the Perception Neuron. The most expensive MoCap analyzed was from AiQ Synertial, costing 10650 €. Therefore, this current version of the Ergowear can be considered low cost, which may ease its future mass production and accessibility in the industrial world, for daily use.

5.2 Usability Validation

9 healthy volunteers (5 male, 4 female, 65,5 ±10,0 kg, 169,4 ±7,8 cm) participated in the wearable's ergonomic testing. The tests were comprised of a combination of simple joint movements, namely: (i) crossing both arms; (ii) trunk flexion/extension; (iii) trunk rotation; (iv) trunk side-bending; (v) neck flexion/extension; (vi) neck rotation; (vii) neck side-bending; (viii) arms stretching at the front, up, and back; (ix) shoulder rotation; (x) wrist rotation; (xi) wrist flexion/extension; (xii) wrist ulnar/radial deviation. Furthermore, each participant jumped with the suit, and lastly, made a motion where a box would be picked up from the floor, and placed on top of a table after the participant would reach as high as possible with the box. Each motion was repeated three times, per participant. Fig. 63 showcase several movements performed by different participants in this test.

In another trial of this test, each biofeedback motor was individually and randomly activated, with the participant having to identify the location where the vibrotactile was operating. After the tests, each volunteer answered anonymously a custom-made usability questionnaire, based on the SUS template. For each of the questions, the user needed to answer on a scale of 1 to 5, 1 for "Strongly Agree" and 5 for "Strongly Disagree" what the user perceived from the tests. The results from the questionnaire are showcased in Fig. 64. In turn, Fig. 65 showcase the results regarding the motors sensing tests.

From Fig. 65 it is possible to observe that all 9 participants felt each biofeedback motor in the respective area, with the exception of the lumbar motor. For this motor, only five of the participants reported that they felt it clearly, with two having a more neutral opinion, and the other two reporting that they did not feel it, or at least did not feel it clearly.

Moreover, for 5 of the participants, the wireless communication was established, in a trial of 5 minutes which encompassed the ergonomic test's motions. This served to analyze if the system failed the I2C communication during the tests. It was observed that for the first subject, the communication with the IMU on the right hand failed. After the test, it was observed that inside the connector the cable shielding broke from the weld and was short-circuiting with the power supply conductor. This was corrected, and the weld was reinforced. For the rest of the tests, there was no other communication failure with the sensors.

Regarding the usability tests, this system was seen as a direct improvement regarding the previous

(a)

(b)

(c)

(d)

Figure 63: Movements performed by users during the ergonomic tests. a) Trunk flexion, b) wrist flexion, c) crossing arms and d) placing the box on top of the cabinet.

system. From the test results, it is possible to observe that it was generally well accepted by the participants, whether be it aesthetically or in terms of comfortability. The participants did not report any heat accumulation in the suit, which is ideal. Furthermore, they did not feel like they were restricted of moving the upper body joints and reaching their maximum ROM, with the exception of one participant. Moreover, most of them reportedly felt like the suit's textile was comfortable, and that they would be confident to wear it in public. Although, to test the suit's usability for a 8-hour working cycle, a validation in an industrial context needs to be performed, with real workers, to obtain more accurate results. Nevertheless, this general acceptation of the wearable itself points towards its high standard in terms of usability and wearability.

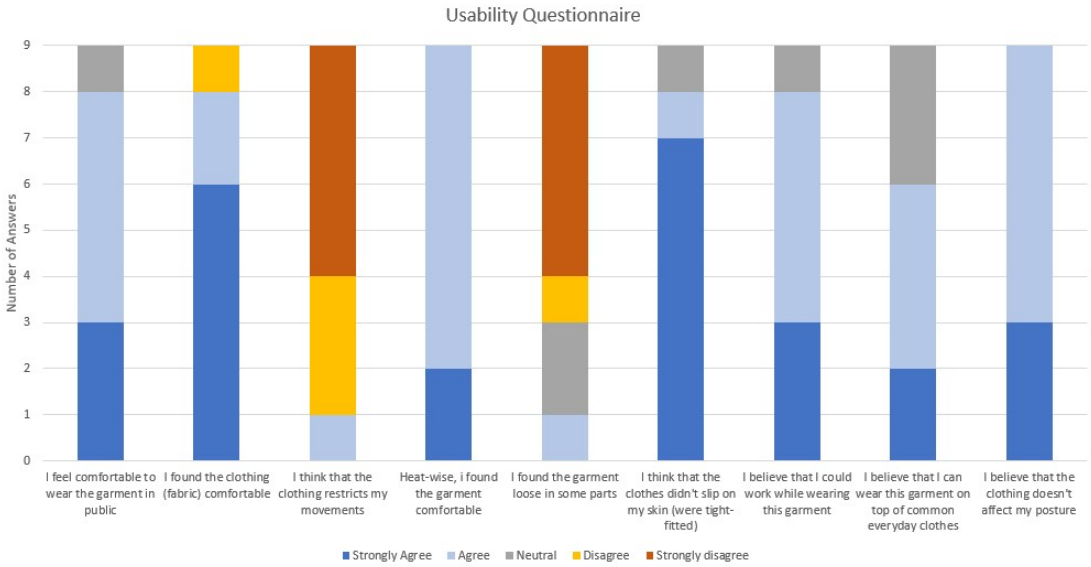

Figure 64: Sytem's Usability questionnaire answers.

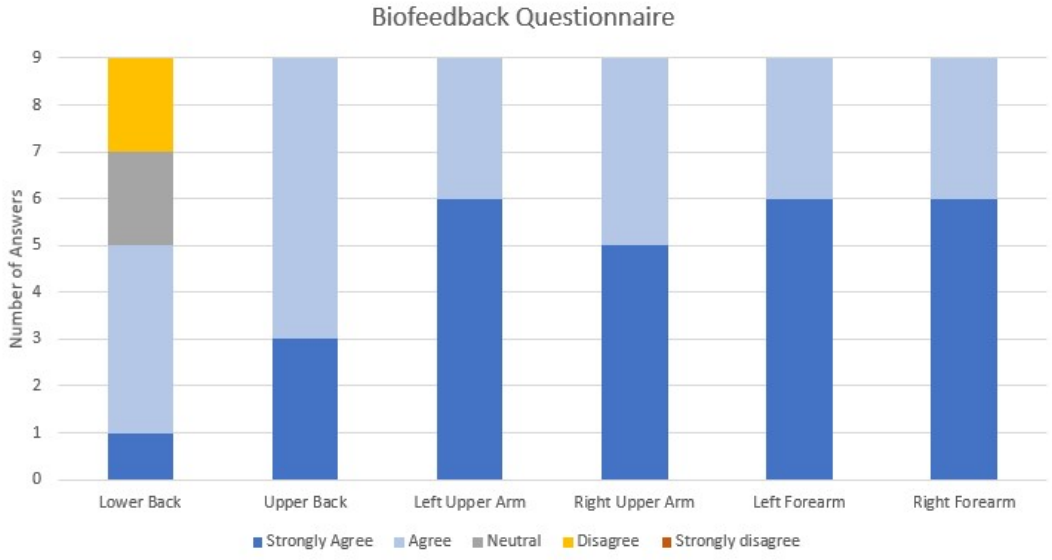

Figure 65: System's Biofeedback questionnaire answers.

Although the current system was overall well accepted by the participants, as the questionnaire results suggest, it still presents some limitations. One of the downsides of the suit is the lack of sleeve stretching, which led to resistance in the thumb's support textile on the hand. This in turn led to some cases where the user felt some minor pain or felt uncomfortable on the hand. This was more prevalent in the male participants, namely the ones which had broader shoulders. This aspect of the suit was addressed during the wearable's development phase. Nevertheless, the lighter mesh present on the shoulder area could be made even less dense, or its area can be increased. Furthermore, it was concluded that the reason for this inconvenience can be directly associated with the textile around the thumb. This part of the suit will need to be redesigned, and corrected. A possible solution is the use of a lighter and more elastic mesh in that area, such as the one used on the shoulder and elbow joint, which will lead to less pressure on the thumb.

In terms of the biofeedback operation mode of the wearable, it is possible to observe that all of the participants successfully felt the motor vibration in the respective area. However, it seems that the lower back motor was systematically less clearly felt compared with the rest. This was due to the curvature of the lower back, which is generally more notable in female users. Adding to this, the waistband that was added to compress the back of the suit's textile, fixing the lower back sensor and motor to the user's body, did not compress the latter due to the sensor module being much bigger, accumulating all of the pressure. Still addressing the biofeedback system, it was observed that the motors in each of the respective pockets were not completely fixed, and after some movements or being used for some time, they would fall out of the pockets. A more compressive strategy needs to be addressed. The use of openings in the suit, with the motor making direct contact with the user could be addressed. However, the motors heat up significantly during operation, which could make the user uncomfortable after long periods of time. One possible solution is the use of a closed channel at the entrance of the socket. The entry of the motor would need to be forced, but it would guarantee that the motor would be stuck in the pocket. Alternatively, glued velcro patches that stick to the textile could be applied to the back of the motors. These were the main limitations reported for the wearable.

Other observations were also reported regarding the usability of the system. It was reported that some users felt uncomfortable to sit while wearing the wearable, since they were afraid to damage the electronics. The only way considered to overcome this limitation is to alter the position where the powerbank and the processing unit are positioned. They would still need to be positioned symmetrically in regards to the user's spine, as to balance the weight of the wearable. Therefore, the other alternative would be to position these units a little higher on the suit. This however would lead to the fact that their weight would be more felt by the user, as they would be away from the user's center of mass, which is around the hip area. Secondly, people that did not use clothes with collar felt the front zip scratching the skin. This can be easily corrected by using a cover on he interior of the zip. Furthermore, some participants reported, during the tests, that they felt the lower back cable. Ideally, none of the wearable's electronics would be felt by the user. This is due to the high rigidity of the selected cables used on the intermediary modules. These were deemed not ideal since their selection. But due to lack of material in stock, they

were selected. The proposed solution would be to select 6-wired, with 28-32 AWG, less than 4 mm of diameter, with shielding, and with an outer jacket of silicone, cables.

Lastly, it was observed during the usability tests that the sensor pockets successfully fixed the sensors' orientation and position in regard to the attached anatomic segment. This can also be due to the connection setup developed for this system, in which the cable connectors are present in the middle of the anatomic segments, and not in the sensor modules. Therefore, as previously stated, the oscillation of the cables lead to the oscillation of the connectors, but since the connectors are separated from the sensor casings, they do not affect as much the sensors' orientation. Moreso, the waist band added to the final version of the wearable was able to push and fix the lower back sensor onto the user's skin successfully, compressing that area, which the previous iteration was unable to do.

6

Conclusions and Future Work

6.1 Conclusion

The high incidence of Work-Related Musculoskeletal Disorders (WRMSDs) in the industrial environment leads to not only a high economic impact in the EU economy, as well as a significantly high impact on the health of the workers, leading to possible lifelong impairments, or anticipated retirements. Therefore, several tools were developed to mitigate the prevalence of these disorders in the workplace. Currently, the use of inertial MoCap technology is being heavily investigated to serve as a direct ergonomic assessment system. Furthermore, with the idealization of the new 5.0 industry wave, a rise of interest in the collaboration between robots and the human worker is being observed. For this type of relation to exist, the robot needs to be aware of the worker's intention, which can be achieved through a MoCap data framework.

Chapter 2 consisted of a review of the SOA concerning the existing wearable, inertial MoCap systems, with a special focus on fusion filtering algorithms, STS calibration sequences and a hardware and textile configuration overview. It allowed to identify the benchmark limitations regarding the accuracy of several inertial systems, due to the lack of standard protocols. Furthermore, this review help selecting the fusion filter, the calibration procedure and the type of sensors used, as well as the basis for the garment. This review of the SOA was the first step of the conceptualization of the new system.

This dissertation revolved around the development of a new iteration of an inertial upper body MoCap system, that was built upon on a previous model that is described in [29]. It was developed in accordance to the functional, usability and technical requirements defined in Chapter 3. The first part of this work revolved around testing the previous iteration, identifying its downsides and consequently correcting them. It was concluded that during the execution of several trials with the previous iteration, the system had clear limitations regarding sensor fixation, usability and wearability, and cabling. Furthermore, it didn't present a fusion filter, or STS calibration routine. Therefore, to develop the new version, a user-centred design approach was implemented, in which each addressed strategy was followed to correct and improve the previous system's limitations. Moreover, the SDI block was added.

Chapter 4 describes the development process of the new version, from the garment's design, hardware units, and firmware and software, leading to the construction of a prototype. The garment is based on a

body suit, made of a tight-fitting, and elastic textile, to allow freedom of movement, high level of comfort, and the fixation of the sensors to the skin of the user. Several aspects of the garment were considered to compensate for the limitations of the previous system. Regarding the hardware, new low-cost sensors, with less bias than the previous ones, were selected. Another reason to select these sensors was due to the connectors they integrated, which allowed the use of a wire-to-board type of connection, leading to the connection between modules being made on the anatomical segments, avoiding the cable movements of interfering with the sensor modules, and the development of external PCBs dedicated to integrate the connectors, which would lead to a rise in the modules' dimensions. The processing unit was also altered, to reduce the current consumption of the system and improve the sampling frequency as well, in order to be able to perform the SDI. A WiFi communication setup, using the WiFi module as an AP, was established between the processing unit and the main station, through an UDP communication protocol, capable of sending data both ways.

Chapter 5 revolved around the validation of the new system in regard to the specified requirements, described in Chapter 3. Regarding the validation of the new hardware, firmware and textile, it is possible to conclude that it fully conforms with the specified technical and usability requirements that were targeted for validation, at least in a controlled environment. In terms of the wireless UDP communication setup, it was proven that, in the tested conditions, it is stable in terms of distancing and duration, namely in packet loss, latency, sampling frequency and data corruption. It was seen that the UDP communication setup had reduced performance with higher distances, namely starting from 5 meters between the station and the processing unit. However, its reduction in performance is negligible. In regard to the "Power Supply Influence" test results, it was concluded that the system maintains its communication characteristics throughout long sessions, leading to its proven stability for an 8 hour working session. Furthermore, its autonomy in two different conditions - monitoring mode and biofeedback mode - was also ascertained, surpassing the expected 8 hours requirement by a large margin. Therefore, an alternative powerbank, with less capacity and weight, was proposed, to miniaturize the power supply unit, leading to a higher usability for the wearable. Nevertheless, a validation in the industrial context, which provides a more accurate representation of the system's future operation, needs to be addressed. Moreover, the usability part of the testing needs to also be performed with industrial workers, as they will be the target users for this system. For the garment of this new version, focus was dedicated in its design, which led to a wearability improvement of the system. One of the majors improvements revolved around its aesthetic, whether from the garment itself, as well as the covering of the wearable's hardware. Lastly, a comparison between the current version, and the previous one was assessed, with the current system being a direct improvement regarding the hardware, and usability. A reduction of the packet loss was systematically seen in each of the tests. This leads to the conclusion that the new system presents much higher wireless communication performance, to the best of the author's knowledge. Moreover, in terms of hardware, each of the units that compose the wearable was successfully miniaturized and improved, whether being in terms of usability or energy efficiency. For the latter, a decrease of around 320 % for the current consumption was observed, with the system operating in monitoring mode. Moreso, the new system is

capable of sampling the gyroscope data at 240 Hz, with the previous iteration only achieving a frequency of 100 Hz. This leads to an acquisition of the angular velocity data with a higher level of resolution, which is necessary to obtain a more accurate joint angle estimation system.

As a final conclusion, the system appears to be a solid starting point for the development of a low-cost MoCap system that can be integrated in the industrial context. Systems like the XSens are not viable for these types of operations due to being extremely costly to be used on a daily basis at a factory.

The work performed for this dissertation was able to answer the research questions defined in Chapter 1:

- **Question 1: What are the main requirements that need to be taken into consideration when devising an inertial MoCap system, that can comply with the user's needs, in an industrial setting?** This is answered in Chapter 3. The requirements defined for the system were conceptualized by a group of ergonomists and engineers, in accordance with their specifications and needs. Three main groups of requirements were defined: functional requirements, usability requirements and technical requirements. For the functional requirements, it was observed that, namely, the system must be able to estimate the joint angles of the user, monitor the worker's posture, provide biofeedback, if needed, allow the integration of a collaborative robot, among others. For the usability and wearability aspects of the system, which target the wearable, it was defined that the system must be comfortable, cannot restrict the worker's motions, easily rechargeable, lightweight, among others. Lastly, the technical requirements, which address the hardware and firmware of the system, the system must be able to operate for 8 hours consistently, present low latency, have electromechanical robustness, have low, or ideally no packet loss or data corruption, among others.

- **Question 2: How to improve a MoCap smart-garment in terms of usability, and performance, while maintaining its low-cost feature?** This question is answered in Chapters 3 and 5. The development of a new and improved version started from the analysis of the previous system's faults and limitations. To achieve that, a testing protocol was designed, with one of the main reasons being the assessment of its limitations. The reported limitations, plus the specified requirements for the system, lead to the foundation of the development of the new system, in which each followed strategy was devised in order to surpass the previous version's limitations, or to further improve the system. Lastly, the results showed that, in every metric regarding the system's hardware, and WiFi communication performance (with the exception of the latency, which cannot be directly compared), the current system is a direct improvement in regard to the previous one. Furthermore, no sensor oscillation or misalignment was observed for the current version of the system. Moreover, regarding the usability of the system, the volunteers that participated in both tests (used the previous system and the current one), stated that the new is overall an improvement regarding the previous version. Therefore, it is possible to conclude, to the best of the author's knowledge, that the new system is, overall, a significant improvement when compared

with the previous one. Lastly, this was all possible while the system maintained its low-cost feature (respected the low-cost requirement).

6.2 Future Work

Although the hardware for this iteration was fully developed, there is work to be done in the software part of the system, mainly regarding the main station. Currently, the main station is equipped to receive and read the sensor data, as well as manually send commands. However, the main station needs to also be able to parse the acquired sensor data, and use it to estimate the user's upper body joint angles.

- Regarding the wearable's suit, since the purpose of it is being tightly fitted to the user's body, a standard size can't be applied to different body types. Therefore, different suit sizes need to be explored before this product can widely accessible to the general public. Moreover, from the analyzed usability test results, the biofeedback motors' pockets need to be reformulated, so they can successfully fix these motors. Furthermore, some users reported some wearability limitations regarding the suit. The frontal zipper, in some cases, would scratch the user's skin. A protective textile needs to be integrated on the inside of the zipper. Also, there were reported cases where the user would feel the pressure of the textile around the thumb, which would cause the participant to feel uncomfortable. This is connected to a lack of joint mobility of the shoulder. Although this was addressed during the development stage of the suit, with a strategy of using a lighter mesh to allow more elasticity in the shoulder area, it was perceived that it was not enough. It was identified that the stitching of the textile around the thumb was causing this inconvenience to the users, with the needing to be redesigned.

- In terms of hardware, new cables need to be implemented for the back and upper arms sensor modules, since they could be improved in terms of flexibility. Moreover, although the system's hardware was miniaturized in regard to the previous iteration, further miniaturization can be achieved, since the sensors and low-level processor are embedded in breakout boards. Therefore, custom PCBs can be developed for these modules, in an effort of only preserving the necessary parts, diminishing their dimensions, especially for the processor, which includes a great number of pins which were not used.

- In terms of software, there are some features that need to be added into the system. One of them is a client script that is capable of making the interface between the main station's code and the low-level processing unit. Moreover, the joint angle estimation system should be promptly validated with the current hardware, using human participants. Furthermore, although the implemented fusion filter's accuracy was not validated within the new iteration yet, it was tested with the previous iteration. Moreover, although the ECF is integrated with a threshold-based algorithm to reject non-geomagnetic magnetic values, adaptive-based algorithms should be investigated and implemented onto the framework. These type of measurement reject algorithms are more difficult to implement, but if possible to integrate, they are seen as more accurate in regard to the threshold-based ones.

For the system's validation, this system was validated in a controlled environment, with people not

used to work in an industrial environment. This should be addressed in the current iteration, or a future one.

Lastly, this system is equipped with features such as the ECF fusion filter, the sensors' calibration and sensor-to-segment calibration routine that can be used for the current system. The system should be, in the future, benchmarked against other MoCap systems available on the literature.

Bibliography

[1] J. M. Lourenço. *The NOVAthesis LaTeX Template User's Manual*. NOVA University Lisbon. 2021. url: https://github.com/joaomlourenco/novathesis/raw/master/template.pdf.

[2] C. Altomonte et al. *Remaking Europe: the new manufacturing as an engine for growth*. Ed. by Reinhilde Veugelers. 2017. isbn: 9789078910442. url: https://search.proquest.com/docview/1937673402?accountid=17242%5C%0Ahttp://bruegel.org/2017/09/remaking-europe/.

[3] U.S. Bureau of Labour Statistics. *Fact Sheet | Occupational injuries and illnesses resulting in musculoskeletal disorders (MSDs)*. 2020. url: https://www.bls.gov/iif/oshdef.htm (visited on 2022-05-17).

[4] J. De Kok et al. *Work-related musculoskeletal disorders: prevalence, costs and demographics in the EU*. Tech. rep. 2019, p. 215. doi: 10.2802/66947. url: https://osha.europa.eu/es/publications/msds-facts-and-figures-overview-prevalence-costs-and-demographics-msds-europe/view.

[5] Health and Safety Executive. *Work related musculoskeletal disorders in Great Britain (WRMSDs), 2019*. Tech. rep. November. 2020, pp. 1–10. url: http://www.hse.gov.uk/statistics/causdis/msd.pdf.

[6] S. Bevan. "Economic impact of musculoskeletal disorders (MSDs) on work in Europe". In: *Best Practice Research Clinical Rheumatology* 29.3 (2015-06), pp. 356–373. issn: 15216942. doi: 10.1016/j.berh.2015.08.002. url: https://linkinghub.elsevier.com/retrieve/pii/S1521694215000947.

[7] W. Grzywiński et al. "The prevalence of self-reported musculoskeletal symptoms among loggers in Poland". In: *International Journal of Industrial Ergonomics* 52 (2016-03), pp. 12–17. issn: 01698141. doi: 10.1016/j.ergon.2015.07.003. url: https://linkinghub.elsevier.com/retrieve/pii/S016981411530007X.

[8] EU-OSHA. *Work-related musculoskeletal disorders in the EU — Facts and figures*. Tech. rep. 2010, pp. 1–179.

[9] World Health Organization. *Protecting Workers' Health Series No. 5, Preventing musculoskeletal disorders in the workplace*. Tech. rep. 2015, pp. 1–32. url: http://www.who.int/occupational_health/publications/%5C%5Cnmuscdisorders/en/.

[10] N. Bevan, J. Carter, and S. Harker. "ISO 9241-11 Revised: What Have We Learnt About Usability Since 1998?" In: *Lecture Notes in Computer Science (including subseries Lecture Notes in Artificial Intelligence and Lecture Notes in Bioinformatics)*. Vol. 9169. 2015, pp. 143–151. isbn: 9783319209005. doi: 10.1007/978-3-319-20901-2_13. url: http://link.springer.com/10.1007/978-3-319-20901-2_13.

[11] Health and Safety Executive. *Health and safety at work: Summary statistics for Great Britain 2018*. Tech. rep. 2018.

[12] N. Inyang et al. "Ergonomic Analysis and the Need for Its Integration for Planning and Assessing Construction Tasks". In: *Journal of Construction Engineering and Management* 138.12 (2012-12), pp. 1370–1376. issn: 0733-9364. doi: 10.1061/(ASCE)CO.1943-7862.0000556. url: http://ascelibrary.org/doi/10.1061/%5C%28ASCE%5C%29CO.1943-7862.0000556.

[13] WHO. "The burden of musculoskeletal conditions at the start of the new millennium." In: *World Health Organization technical report series* 919 (2003), i–x, 1–218, back cover. issn: 0512-3054. url: http://www.ncbi.nlm.nih.gov/pubmed/14679827.

[14] U. Siebert. "Demonstration of the healthy worker survivor effect in a cohort of workers in the construction industry". In: *Occupational and Environmental Medicine* 58.12 (2001-12), pp. 774–779. issn: 13510711. doi: 10.1136/oem.58.12.774. url: https://oem.bmj.com/lookup/doi/10.1136/oem.58.12.774.

[15] N. Vignais et al. "Physical risk factors identification based on body sensor network combined to videotaping". In: *Applied Ergonomics* 65 (2017-11), pp. 410–417. issn: 00036870. doi: 10.1016/j.apergo.2017.05.003. url: https://linkinghub.elsevier.com/retrieve/pii/S0003687017301060.

[16] P. Spielholz et al. "Comparison of self-report, video observation and direct measurement methods for upper extremity musculoskeletal disorder physical risk factors". In: *Ergonomics* 44.6 (2001-05), pp. 588–613. issn: 0014-0139. doi: 10.1080/00140130118050. url: https://www.tandfonline.com/doi/full/10.1080/00140130118050.

[17] G. LI and P. BUCKLE. "Current techniques for assessing physical exposure to work-related musculoskeletal risks, with emphasis on posture-based methods". In: *Ergonomics* 42.5 (1999-05), pp. 674–695. issn: 0014-0139. doi: 10.1080/001401399185388. url: https://www.tandfonline.com/doi/full/10.1080/001401399185388.

[18] G. C. David. "Ergonomic methods for assessing exposure to risk factors for work-related musculoskeletal disorders". In: *Occupational Medicine* 55.3 (2005-05), pp. 190–199. issn: 1471-8405. doi: 10.1093/occmed/kqi082. url: http://academic.oup.com/occmed/article/55/3/190/1420798/Ergonomic-methods-for-assessing-exposure-to-risk.

[19] L. McAtamney and E. Nigel Corlett. "RULA: a survey method for the investigation of work-related upper limb disorders". In: *Applied Ergonomics* 24.2 (1993-04), pp. 91–99. issn: 00036870. doi: 10.1016/0003-6870(93)90080-S. url: https://linkinghub.elsevier.com/retrieve/pii/000368709390080S.

[20] F. Caputo et al. "A Human Postures Inertial Tracking System for Ergonomic Assessments". In: *Advances in Intelligent Systems and Computing*. Vol. 825. January. Springer International Publishing, 2019, pp. 173–184. isbn: 9783319960678. doi: 10.1007/978-3-319-96068-5_19. url: http://dx.doi.org/10.1007/978-3-319-96068-5_19%20http://link.springer.com/10.1007/978-3-319-96068-5_19.

[21] P. Giannini et al. "Wearable Sensor Network for Biomechanical Overload Assessment in Manual Material Handling". In: *Sensors* 20.14 (2020-07), p. 3877. issn: 1424-8220. doi: 10.3390/s20143877. url: https://www.mdpi.com/1424-8220/20/14/3877.

[22] S. Santos et al. "Explaining the Ergonomic Assessment of Human Movement in Industrial Contexts". In: *Proceedings of the 13th International Joint Conference on Biomedical Engineering Systems and Technologies*. Biostec. SCITEPRESS - Science and Technology Publications, 2020, pp. 79–88. isbn: 978-989-758-398-8. doi: 10.5220/0008953800790088. url: https://www.scitepress.org/DigitalLibrary/Link.aspx?doi=10.5220/0008953800790088.

[23] B. Vanderborght. *Unlocking the potential of industrial human-robot collaboration*. Tech. rep. 2019. doi: 10.2777/568116.

[24] L. Fortini et al. "A Framework for Real-time and Personalisable Human Ergonomics Monitoring". In: *2020 IEEE/RSJ International Conference on Intelligent Robots and Systems (IROS)*. IEEE, 2020-10, pp. 11101–11107. isbn: 978-1-7281-6212-6. doi: 10.1109/IROS45743.2020.9341560. url: https://ieeexplore.ieee.org/document/9341560/.

[25] E. Matheson et al. "Human–Robot Collaboration in Manufacturing Applications: A Review". In: *Robotics* 8.4 (2019-12), p. 100. issn: 2218-6581. doi: 10.3390/robotics8040100. url: https://www.mdpi.com/2218-6581/8/4/100.

[26] S. Nahavandi. "Industry 5.0—A Human-Centric Solution". In: *Sustainability* 11.16 (2019-08), p. 4371. issn: 2071-1050. doi: 10.3390/su11164371. url: https://www.mdpi.com/2071-1050/11/16/4371.

[27] S. El Zaatari et al. “Cobot programming for collaborative industrial tasks: An overview”. In: *Robotics and Autonomous Systems* 116 (2019-06), pp. 162–180. issn: 09218890. doi: 10.1016/j.robot.2019.03.003. url: https://doi.org/10.1016/j.robot.2019.03.003%20https://linkinghub.elsevier.com/retrieve/pii/S092188901830602X.

[28] C. M. Barnum. *Usability Testing Essentials*. 1st ed. Burlington, MA, USA: Morgan Kaufmann, 2011, p. 408. isbn: 9780123750921. doi: 10.1016/B978-0-12-375092-1.00023-4. url: https://linkinghub.elsevier.com/retrieve/pii/B9780123750921000234.

[29] A. Resende et al. “Ergowear: an ambulatory, non-intrusive, and interoperable system towards a Human-aware Human-robot Collaborative framework”. In: *2021 IEEE International Conference on Autonomous Robot Systems and Competitions (ICARSC)*. IEEE, 2021-04, pp. 56–61. isbn: 978-1-6654-3198-9. doi: 10.1109/ICARSC52212.2021.9429796. url: https://ieeexplore.ieee.org/document/9429796/.

[30] K. Kitano, A. Ito, and N. Tsujiuchi. “Hand Motion Measurement using Inertial Sensor System and Accurate Improvement by Extended Kalman Filter”. In: *2019 41st Annual International Conference of the IEEE Engineering in Medicine and Biology Society (EMBC)*. IEEE, 2019-07, pp. 6405–6408. isbn: 978-1-5386-1311-5. doi: 10.1109/EMBC.2019.8856462. url: https://ieeexplore.ieee.org/document/8856462/.

[31] J. H. Ryu et al. “Motion data based construction worker training support tool: Case study of masonry work”. In: *ISARC 2018 - 35th International Symposium on Automation and Robotics in Construction and International AEC/FM Hackathon: The Future of Building Things* Isarc (2018). doi: 10.22260/isarc2018/0150.

[32] M. G. L. Monaco et al. “Biomechanical Load Evaluation by Means of Wearable Devices in Industrial Environments: An Inertial Motion Capture System and sEMG Based Protocol”. In: *Advances in Intelligent Systems and Computing*. Vol. 795. Springer International Publishing, 2019, pp. 233–242. isbn: 9783319946184. doi: 10.1007/978-3-319-94619-1_23. url: http://dx.doi.org/10.1007/978-3-319-94619-1_23%20http://link.springer.com/10.1007/978-3-319-94619-1_23.

[33] D. Menychtas, A. Glushkova, and S. Manitsaris. “Analyzing the kinematic and kinetic contributions of the human upper body’s joints for ergonomics assessment”. In: *Journal of Ambient Intelligence and Humanized Computing* 11.12 (2020-12), pp. 6093–6105. issn: 1868-5137. doi: 10.1007/s12652-020-01926-y. url: https://link.springer.com/10.1007/s12652-020-01926-y.

[34] B. Daria et al. “Integrating mocap system and immersive reality for efficient human-centred workstation design”. In: *IFAC-PapersOnLine* 51.11 (2018), pp. 188–193. issn: 24058963. doi: 10.1016/j.ifacol.2018.08.256. url: https://linkinghub.elsevier.com/retrieve/pii/S2405896318313806.

[35] D. Álvarez et al. “Upper limb joint angle measurement in occupational health”. In: *Computer Methods in Biomechanics and Biomedical Engineering* 19.2 (2016-01), pp. 159–170. issn: 1025-5842. doi: 10.1080/10255842.2014.997718. url: http://www.tandfonline.com/doi/full/10.1080/10255842.2014.997718.

[36] C. Brents et al. “Low Back Biomechanics of Keg Handling Using Inertial Measurement Units”. In: *Advances in Intelligent Systems and Computing*. Vol. 825. Springer International Publishing, 2019, pp. 71–81. isbn: 9783319960678. doi: 10.1007/978-3-319-96068-5_8. url: http://dx.doi.org/10.1007/978-3-319-96068-5_8%20http://link.springer.com/10.1007/978-3-319-96068-5_8.

[37] A. Humadi et al. “Instrumented Ergonomic Risk Assessment Using Wearable Inertial Measurement Units: Impact of Joint Angle Convention”. In: *IEEE Access* 9 (2021), pp. 7293–7305. issn: 2169-3536. doi: 10.1109/ACCESS.2020.3048645. url: https://ieeexplore.ieee.org/document/9311734/.

[38] Z. Wang et al. “Using Wearable Sensors to Capture Posture of the Human Lumbar Spine in Competitive Swimming”. In: *IEEE Transactions on Human-Machine Systems* 49.2 (2019-04), pp. 194–205. issn: 2168-2291. doi: 10.1109/THMS.2019.2892318. url: https://ieeexplore.ieee.org/document/8624346/.

[39] A. Valade et al. “Embedded Sensors System Applied to Wearable Motion Analysis in Sports”. In: *Proceedings of the 9th International Joint Conference on Biomedical Engineering Systems and Technologies*. Vol. 1. Biostec. SCITEPRESS - Science, 2016, pp. 170–175. isbn: 978-989-758-170-0. doi: 10.5220/0005699001700175. url: http://www.scitepress.org/DigitalLibrary/Link.aspx?doi=10.5220/0005699001700175.

[40] I. Aranda-Valera et al. “Measuring Spinal Mobility Using an Inertial Measurement Unit System: A Validation Study in Axial Spondyloarthritis”. In: *Diagnostics* 10.6 (2020-06), p. 426. issn: 2075-4418. doi: 10.3390/diagnostics10060426. url: https://www.mdpi.com/2075-4418/10/6/426.

[41] H. L. Mjøsund et al. “Clinically acceptable agreement between the ViMove wireless motion sensor system and the Vicon motion capture system when measuring lumbar region inclination motion in the sagittal and coronal planes”. In: *BMC Musculoskeletal Disorders* 18.1 (2017-12), p. 124. issn: 1471-2474. doi: 10.1186/s12891-017-1489-1. url: http://bmcmusculoskeletdisord.biomedcentral.com/articles/10.1186/s12891-017-1489-1.

[42] O. Tsilomitrou et al. “On the development of a wireless motion capture sensor node for upper limb rehabilitation”. In: *2019 6th International Conference on Control, Decision and Information Technologies (CoDIT)*. IEEE, 2019-04, pp. 1568–1573. isbn: 978-1-7281-0521-5. doi: 10.1109/CoDIT.2019.8820559. url: https://ieeexplore.ieee.org/document/8820559/.

[43] S. Memar et al. “Segmentation and detection of physical activities during a sitting task in Parkinson’s disease participants using multiple inertial sensors”. In: *Journal of Applied Biomedicine* 15.4 (2017-11), pp. 282–290. issn: 1214021X. doi: 10.1016/j.jab.2017.05.002. url: http://dx.doi.org/10.1016/j.jab.2017.05.002%20http://jab.zsf.jcu.cz/doi/10.1016/j.jab.2017.05.002.html.

[44] A. V. Ivanov and E. A. Zhilenkova. “Software Environment for Motion Capture System Based on Inertial Sensors”. In: *2019 IEEE Conference of Russian Young Researchers in Electrical and Electronic Engineering (EIConRus)*. IEEE, 2019-01, pp. 230–234. isbn: 978-1-7281-0339-6. doi: 10.1109/EIConRus.2019.8656770. url: https://ieeexplore.ieee.org/document/8656770/.

[45] A. Shintemirov et al. “An Open-Source 7-DOF Wireless Human Arm Motion-Tracking System for Use in Robotics Research”. In: *Sensors* 20.11 (2020-05), p. 3082. issn: 1424-8220. doi: 10.3390/s20113082. url: https://www.mdpi.com/1424-8220/20/11/3082.

[46] G. Zuo, Y. Qiu, and T. Pan. “Attitude Algorithm of Human Motion Capture System for Teleoperation of Humanoid Robots”. In: *2018 Chinese Automation Congress (CAC)*. IEEE, 2018-11, pp. 3890–3895. isbn: 978-1-7281-1312-8. doi: 10.1109/CAC.2018.8623765. url: https://ieeexplore.ieee.org/document/8623765/.

[47] J. K. Lee et al. “Wireless Epidermal Six-Axis Inertial Measurement Units for Real-Time Joint Angle Estimation”. In: *Applied Sciences* 10.7 (2020-03), p. 2240. issn: 2076-3417. doi: 10.3390/app10072240. url: https://www.mdpi.com/2076-3417/10/7/2240.

[48] M. Schepers, M. Giuberti, and G. Bellusci. *Xsens MVN : consistent tracking of human motion using inertial sensing*. Tech. rep. March. 2018, pp. 1–8. doi: 10.13140/RG.2.2.22099.07205.

[49] Xsens Technologies B.V. *MVN Animate*. url: https://www.xsens.com/products/mvn-animate.

[50] Rokoko. *Smartsuit Pro*. url: https://www.rokoko.com/products/smartsuit-pro (visited on 2021-07-01).

[51] NOITOM. *Perception Neuron Systems*. url: https://neuronmocap.com/perception-neuron-series.

[52] NOITOM. *AXIS NEURON User Guide*. Tech. rep. Noitom Ltd., 2016, p. 127. url: https://shopcdn.noitom.com.cn/software/AxisUserGuideFinal0923.pdf.

[53] NANSENSE Inc. *Nansense Suits*. url: https://www.nansense.com/suits/.

[54] AiQ Synertial. *IGS Cobra Suit*. url: https://est-kl.com/it/manufacturer/aiq-synertial/igs-cobra-suit.html#more-information.

[55] Motion Workshop. *Shadow Motion*. url: https://www.motionshadow.com/specs (visited on 2021-08-09).

[56] STT Systems. *iSen system*. url: https://www.stt-systems.com/motion-analysis/inertial-motion-capture/isen/#documentation.

[57] APDM Wearable Technologies Inc. *THE OPAL*. url: https://apdm.com/wearable-sensors/.

[58] Trivisio Prototyping GmbH. *Light Motion Suite*. Tech. rep. 2016, p. 2.

[59] I. Poitras et al. "Validity and Reliability of Wearable Sensors for Joint Angle Estimation: A Systematic Review". In: *Sensors* 19.7 (2019-03), p. 1555. issn: 1424-8220. doi: 10.3390/s19071555. url: https://www.mdpi.com/1424-8220/19/7/1555.

[60] I. Poitras et al. "Validity of Wearable Sensors at the Shoulder Joint: Combining Wireless Electromyography Sensors and Inertial Measurement Units to Perform Physical Workplace Assessments". In: *Sensors* 19.8 (2019-04), p. 1885. issn: 1424-8220. doi: 10.3390/s19081885. url: https://www.mdpi.com/1424-8220/19/8/1885.

[61] R. Sers et al. "Validity of the Perception Neuron inertial motion capture system for upper body motion analysis". In: *Measurement* 149 (2020-01), p. 107024. issn: 02632241. doi: 10.1016/j.measurement.2019.107024. url: https://doi.org/10.1016/j.measurement.2019.107024%20https://linkinghub.elsevier.com/retrieve/pii/S0263224119308905.

[62] X. Robert-Lachaine et al. "Validation of a low-cost inertial motion capture system for whole-body motion analysis". In: *Journal of Biomechanics* 99 (2020-01), p. 109520. issn: 00219290. doi: 10.1016/j.jbiomech.2019.109520. url: https://doi.org/10.1016/j.jbiomech.2019.109520%20https://linkinghub.elsevier.com/retrieve/pii/S0021929019307742.

[63] A. Ancans et al. "Wearable Sensor Clothing for Body Movement Measurement during Physical Activities in Healthcare". In: *Sensors* 21.6 (2021-03), p. 2068. issn: 1424-8220. doi: 10.3390/s21062068. url: https://www.mdpi.com/1424-8220/21/6/2068.

[64] G. Ligorio et al. "A Wearable Magnetometer-Free Motion Capture System: Innovative Solutions for Real-World Applications". In: *IEEE Sensors Journal* 20.15 (2020-08), pp. 8844–8857. issn: 1530-437X. doi: 10.1109/JSEN.2020.2983695. url: https://ieeexplore.ieee.org/document/9049101/.

[65] F. Caputo et al. "A Preventive Ergonomic Approach Based on Virtual and Immersive Reality". In: *Advances in Intelligent Systems and Computing*. Vol. 588. July. 2018, pp. 3–15. isbn: 9783319605814. doi: 10.1007/978-3-319-60582-1_1. url: http://link.springer.com/10.1007/978-3-319-60582-1_1.

[66] M. I. M. Esfahani et al. “Sharif-Human movement instrumentation system (SHARIF-HMIS): Development and validation”. In: *Medical Engineering Physics* 61 (2018-11), pp. 87–94. issn: 13504533. doi: 10.1016/j.medengphy.2018.07.008. url: https://doi.org/10.1016/j.medengphy.2018.07.008%20https://linkinghub.elsevier.com/retrieve/pii/S1350453318301176.

[67] T. V. Marcard. “Design and implementation of an attitude estimation system to control orthopedic components”. In: 2010.

[68] W. Li and J. Wang. “Effective Adaptive Kalman Filter for MEMS-IMU/Magnetometers Integrated Attitude and Heading Reference Systems”. In: *Journal of Navigation* 66.1 (2013-01), pp. 99–113. issn: 0373-4633. doi: 10.1017/S0373463312000331. url: https://www.cambridge.org/core/product/identifier/S0373463312000331/type/journal_article.

[69] S. S. Pastor et al. “A Real-time Motion Tracking Wireless System for Upper Limb Exosuit Based on Inertial Measurement Units and Flex Sensors”. In: *International Journal of Engineering* 32.6 (2019-06), pp. 820–827. issn: 24237167. doi: 10.5829/ije.2019.32.06c.04. url: http://www.ijeir.info/article_89313.html.

[70] P. Pomiersky, K. Karlovic, and T. Maier. “Usability-Optimization of Inertial Motion Capture Systems”. In: *Advances in Intelligent Systems and Computing*. Vol. 824. Springer International Publishing, 2019, pp. 345–355. isbn: 9783319960708. doi: 10.1007/978-3-319-96071-5_37. url: http://dx.doi.org/10.1007/978-3-319-96071-5_37%20http://link.springer.com/10.1007/978-3-319-96071-5_37.

[71] J. A. Barraza Madrigal et al. “Evaluation of suitability of a micro-processing unit of motion analysis for upper limb tracking”. In: *Medical Engineering Physics* 38.8 (2016-08), pp. 793–800. issn: 13504533. doi: 10.1016/j.medengphy.2016.04.011. url: https://linkinghub.elsevier.com/retrieve/pii/S1350453316300674.

[72] J. Marin, T. Blanco, and J. Marin. “Octopus: A Design Methodology for Motion Capture Wearables”. In: *Sensors* 17.8 (2017-08), p. 1875. issn: 1424-8220. doi: 10.3390/s17081875. url: http://www.mdpi.com/1424-8220/17/8/1875.

[73] J. K. Lee, E. J. Park, and S. N. Robinovitch. “Estimation of Attitude and External Acceleration Using Inertial Sensor Measurement During Various Dynamic Conditions”. In: *IEEE Transactions on Instrumentation and Measurement* 61.8 (2012-08), pp. 2262–2273. issn: 0018-9456. doi: 10.1109/TIM.2012.2187245. url: https://ieeexplore.ieee.org/iel5/19/4407674/06172226.pdf%20http://ieeexplore.ieee.org/document/6172226/.

[74] L. Pacher et al. “Sensor-to-Segment Calibration Methodologies for Lower-Body Kinematic Analysis with Inertial Sensors: A Systematic Review”. In: *Sensors* 20.11 (2020-06), p. 3322. issn: 1424-8220. doi: 10.3390/s20113322. url: https://www.mdpi.com/1424-8220/20/11/3322.

[75] B. Bouvier et al. “Upper Limb Kinematics Using Inertial and Magnetic Sensors: Comparison of Sensor-to-Segment Calibrations”. In: *Sensors* 15.8 (2015-07), pp. 18813–18833. issn: 1424-8220. doi: 10.3390/s150818813. url: http://www.mdpi.com/1424-8220/15/8/18813.

[76] Y.-T. Liu, Y.-A. Zhang, and M. Zeng. “Sensor to segment calibration for magnetic and inertial sensor based motion capture systems”. In: *Measurement* 142 (2019-08), pp. 1–9. issn: 02632241. doi: 10.1016/j.measurement.2019.03.048. url: https://doi.org/10.1016/j.measurement.2019.03.048%20https://linkinghub.elsevier.com/retrieve/pii/S026322411930274X.

[77] M. Zabat et al. “IMU-based sensor-to-segment multiple calibration for upper limb joint angle measurement—a proof of concept”. In: *Medical & Biological Engineering & Computing* 57.11 (2019-11), pp. 2449–2460. issn: 0140-0118. doi: 10.1007/s11517-019-02033-7. url: http://link.springer.com/10.1007/s11517-019-02033-7.

[78] P. Picerno et al. “Upper limb joint kinematics using wearable magnetic and inertial measurement units: an anatomical calibration procedure based on bony landmark identification”. In: *Scientific Reports* 9.1 (2019-12), p. 14449. issn: 2045-2322. doi: 10.1038/s41598-019-50759-z. url: http://www.nature.com/articles/s41598-019-50759-z.

[79] W. Kong et al. “Anatomical Calibration through Post-Processing of Standard Motion Tests Data”. In: *Sensors* 16.12 (2016-11), p. 2011. issn: 1424-8220. doi: 10.3390/s16122011. url: http://www.mdpi.com/1424-8220/16/12/2011.

[80] M. Nazarahari and H. Rouhani. “40 years of sensor fusion for orientation tracking via magnetic and inertial measurement units: Methods, lessons learned, and future challenges”. In: *Information Fusion* 68 (2021-04), pp. 67–84. issn: 15662535. doi: 10.1016/j.inffus.2020.10.018. url: https://doi.org/10.1016/j.inffus.2020.10.018%20https://linkinghub.elsevier.com/retrieve/pii/S1566253520303997.

[81] B. Fan, Q. Li, and T. Liu. “How Magnetic Disturbance Influences the Attitude and Heading in Magnetic and Inertial Sensor-Based Orientation Estimation”. In: *Sensors* 18.2 (2017-12), p. 76. issn: 1424-8220. doi: 10.3390/s18010076. url: http://www.mdpi.com/1424-8220/18/1/76.

[82] A. Filippeschi et al. “Survey of Motion Tracking Methods Based on Inertial Sensors: A Focus on Upper Limb Human Motion”. In: *Sensors* 17.6 (2017-06), p. 1257. issn: 1424-8220. doi: 10.3390/s17061257. url: http://www.mdpi.com/1424-8220/17/6/1257.

[83] G. Ligorio and A. M. Sabatini. “A Novel Kalman Filter for Human Motion Tracking With an Inertial-Based Dynamic Inclinometer”. In: *IEEE Transactions on Biomedical Engineering* 62.8 (2015-08), pp. 2033–2043. issn: 0018-9294. doi: 10.1109/TBME.2015.2411431. url: http://ieeexplore.ieee.org/document/7056449/.

[84] S. O. H. Madgwick, A. J. L. Harrison, and R. Vaidyanathan. "Estimation of IMU and MARG orientation using a gradient descent algorithm". In: *2011 IEEE International Conference on Rehabilitation Robotics*. June 2011. IEEE, 2011-06, pp. 1–7. isbn: 978-1-4244-9862-8. doi: 10.1109/ICORR.2011.5975346. url: http://ieeexplore.ieee.org/document/5975346/.

[85] S. O. H. Madgwick et al. "An Extended Complementary Filter for Full-Body MARG Orientation Estimation". In: *IEEE/ASME Transactions on Mechatronics* 25.4 (2020-08), pp. 2054–2064. issn: 1083-4435. doi: 10.1109/TMECH.2020.2992296. url: https://ieeexplore.ieee.org/document/9103115/.

[86] C. Yi et al. "Estimating Three-Dimensional Body Orientation Based on an Improved Complementary Filter for Human Motion Tracking". In: *Sensors* 18.11 (2018-11), p. 3765. issn: 1424-8220. doi: 10.3390/s18113765. url: http://www.mdpi.com/1424-8220/18/11/3765.

[87] R. E. Kalman. "A New Approach to Linear Filtering and Prediction Problems". In: *Journal of Basic Engineering* 82.1 (1960-03), pp. 35–45. issn: 0021-9223. doi: 10.1115/1.3662552. url: https://asmedigitalcollection.asme.org/fluidsengineering/article/82/1/35/397706/A-New-Approach-to-Linear-Filtering-and-Prediction.

[88] A. Atrsaei et al. "Human Arm Motion Tracking by Inertial/Magnetic Sensors Using Unscented Kalman Filter and Relative Motion Constraint". In: *Journal of Intelligent Robotic Systems* 90.1-2 (2018-05), pp. 161–170. issn: 0921-0296. doi: 10.1007/s10846-017-0645-z. url: http://link.springer.com/10.1007/s10846-017-0645-z.

[89] R. Mahony, T. Hamel, and J.-M. Pflimlin. "Nonlinear Complementary Filters on the Special Orthogonal Group". In: *IEEE Transactions on Automatic Control* 53.5 (2008-06), pp. 1203–1218. issn: 0018-9286. doi: 10.1109/TAC.2008.923738. url: http://ieeexplore.ieee.org/document/4608934/.

[90] G. Ligorio and A. Sabatini. "Dealing with Magnetic Disturbances in Human Motion Capture: A Survey of Techniques". In: *Micromachines* 7.3 (2016-03), p. 43. issn: 2072-666X. doi: 10.3390/mi7030043. url: http://www.mdpi.com/2072-666X/7/3/43.

[91] J. K. Lee, T. H. Jeon, and W. C. Jung. "Constraint-augmented Kalman Filter for Magnetometer-free 3D Joint Angle Determination". In: *International Journal of Control, Automation and Systems* 18.11 (2020-11), pp. 2929–2942. issn: 1598-6446. doi: 10.1007/s12555-019-0948-x. url: http://link.springer.com/10.1007/s12555-019-0948-x%20https://link.springer.com/10.1007/s12555-019-0948-x.

[92] T. Lisini Baldi et al. "Upper Body Pose Estimation Using Wearable Inertial Sensors and Multiplicative Kalman Filter". In: *IEEE Sensors Journal* 20.1 (2020-01), pp. 492–500. issn: 1530-437X. doi: 10.1109/JSEN.2019.2940612. arXiv: 1909.10376. url: https://ieeexplore.ieee.org/document/8830389/.

[93] Y. Duan, X. Zhang, and Z. Li. "A New Quaternion-Based Kalman Filter for Human Body Motion Tracking Using the Second Estimator of the Optimal Quaternion Algorithm and the Joint Angle Constraint Method with Inertial and Magnetic Sensors". In: *Sensors* 20.21 (2020-10), p. 6018. issn: 1424-8220. doi: 10.3390/s20216018. url: https://www.mdpi.com/1424-8220/20/21/6018.

[94] G. Ligorio and A. Sabatini. "A linear Kalman Filtering-based approach for 3D orientation estimation from Magnetic/Inertial sensors". In: *2015 IEEE International Conference on Multisensor Fusion and Integration for Intelligent Systems (MFI)*. Vol. 2015-Octob. December. IEEE, 2015-09, pp. 77–82. isbn: 978-1-4799-7772-7. doi: 10.1109/MFI.2015.7295749. url: http://ieeexplore.ieee.org/document/7295749/.

[95] M. D. SHUSTER and S. D. OH. "Three-axis attitude determination from vector observations". In: *Journal of Guidance and Control* 4.1 (1981-01), pp. 70–77. issn: 0162-3192. doi: 10.2514/3.19717. url: https://arc.aiaa.org/doi/10.2514/3.19717.

[96] M. Jin et al. "The adaptive Kalman filter based on fuzzy logic for inertial motion capture system". In: *Measurement* 49.1 (2014-03), pp. 196–204. issn: 02632241. doi: 10.1016/j.measurement.2013.11.022. url: http://dx.doi.org/10.1016/j.measurement.2013.11.022%20https://linkinghub.elsevier.com/retrieve/pii/S0263224113005654.

[97] F. L. Markley. "Attitude Error Representations for Kalman Filtering". In: *Journal of Guidance, Control, and Dynamics* 26.2 (2003-03), pp. 311–317. issn: 0731-5090. doi: 10.2514/2.5048. url: https://arc.aiaa.org/doi/10.2514/2.5048.

[98] J.-H. Zhang et al. "A Novel Adaptive Kalman Filtering Approach to Human Motion Tracking With Magnetic-Inertial Sensors". In: *IEEE Transactions on Industrial Electronics* 67.10 (2020-10), pp. 8659–8669. issn: 0278-0046. doi: 10.1109/TIE.2019.2946557. url: https://ieeexplore.ieee.org/document/8870197/.

[99] L. Peppoloni et al. "A novel 7 degrees of freedom model for upper limb kinematic reconstruction based on wearable sensors". In: *2013 IEEE 11th International Symposium on Intelligent Systems and Informatics (SISY)*. IEEE, 2013-09, pp. 105–110. isbn: 978-1-4799-0305-4. doi: 10.1109/SISY.2013.6662551. url: http://ieeexplore.ieee.org/document/6662551/.

[100] H. J. Luinge and P. H. Veltink. "Measuring orientation of human body segments using miniature gyroscopes and accelerometers". In: *Medical Biological Engineering Computing* 43.2 (2005-04), pp. 273–282. issn: 0140-0118. doi: 10.1007/BF02345966. url: http://link.springer.com/10.1007/BF02345966.

[101] X. Yun and E. R. Bachmann. “Design, Implementation, and Experimental Results of a Quaternion-Based Kalman Filter for Human Body Motion Tracking”. In: *IEEE Transactions on Robotics* 22.6 (2006-12), pp. 1216–1227. issn: 1552-3098. doi: 10.1109/TRO.2006.886270. url: http://ieeexplore.ieee.org/document/4020379/.

[102] A. Young. “Comparison of Orientation Filter Algorithms for Realtime Wireless Inertial Posture Tracking”. In: *2009 Sixth International Workshop on Wearable and Implantable Body Sensor Networks*. IEEE, 2009-06, pp. 59–64. isbn: 978-0-7695-3644-6. doi: 10.1109/BSN.2009.25. url: http://ieeexplore.ieee.org/document/5226917/.

[103] R. Valenti, I. Dryanovski, and J. Xiao. “Keeping a Good Attitude: A Quaternion-Based Orientation Filter for IMUs and MARGs”. In: *Sensors* 15.8 (2015-08), pp. 19302–19330. issn: 1424-8220. doi: 10.3390/s150819302. url: http://www.mdpi.com/1424-8220/15/8/19302.

[104] Fairchild. “AN-5084 XKF 3-Low-Power , Optimal Estimation of 3 D Orientation using Inertial and Magnetic Sensing Summary”. In: 2015.

[105] J. Lee and M. Choi. “Robust Inertial Measurement Unit-Based Attitude Determination Kalman Filter for Kinematically Constrained Links”. In: *Sensors* 19.4 (2019-02), p. 768. issn: 1424-8220. doi: 10.3390/s19040768. url: http://www.mdpi.com/1424-8220/19/4/768.

[106] A. M. Sabatini. “Kalman-Filter-Based Orientation Determination Using Inertial/Magnetic Sensors: Observability Analysis and Performance Evaluation”. In: *Sensors* 11.10 (2011-09), pp. 9182–9206. issn: 1424-8220. doi: 10.3390/s111009182. url: http://www.mdpi.com/1424-8220/11/10/9182.

[107] M. A. Javed, M. Tahir, and K. Ali. “Cascaded Kalman Filtering-Based Attitude and Gyro Bias Estimation With Efficient Compensation of External Accelerations”. In: *IEEE Access* 8 (2020), pp. 50022–50035. issn: 2169-3536. doi: 10.1109/ACCESS.2020.2980016. url: https://ieeexplore.ieee.org/document/9032181/.

[108] Y. Tian, H. Wei, and J. Tan. “An Adaptive-Gain Complementary Filter for Real-Time Human Motion Tracking With MARG Sensors in Free-Living Environments”. In: *IEEE Transactions on Neural Systems and Rehabilitation Engineering* 21.2 (2013-03), pp. 254–264. issn: 1534-4320. doi: 10.1109/TNSRE.2012.2205706. url: https://ieeexplore.ieee.org/document/6237648/.

[109] X. Ji and D. Piovesan. “Validation of inertial-magnetic wearable sensors for full-body motion tracking of automotive manufacturing operations”. In: *International Journal of Industrial Ergonomics* 79.May (2020-09), p. 103005. issn: 01698141. doi: 10.1016/j.ergon.2020.103005. url: https://linkinghub.elsevier.com/retrieve/pii/S0169814120300068.

[110] M. A. Wirth et al. “Comparison of a New Inertial Sensor Based System with an Optoelectronic Motion Capture System for Motion Analysis of Healthy Human Wrist Joints”. In: *Sensors* 19.23 (2019-12), p. 5297. issn: 1424-8220. doi: 10.3390/s19235297. url: https://www.mdpi.com/1424-8220/19/23/5297.

[111] S. Santos et al. “Explaining the Ergonomic Assessment of Human Movement in Industrial Contexts”. PhD thesis. Universidade Nova de Lisboa, 2020. isbn: 978-989-758-398-8. doi: 10.5220/0008953800790088. url: https://www.scitepress.org/DigitalLibrary/Link.aspx?doi=10.5220/0008953800790088.

[112] M. M. Morrow et al. “Validation of Inertial Measurement Units for Upper Body Kinematics”. In: *Journal of Applied Biomechanics* 33.3 (2017-06), pp. 227–232. issn: 1065-8483. doi: 10.1123/jab.2016-0120. url: https://journals.humankinetics.com/view/journals/jab/33/3/article-p227.xml.

[113] P. A. C. Widagdo, H.-H. Lee, and C.-H. Kuo. “Limb motion tracking with inertial measurement units”. In: *2017 IEEE International Conference on Systems, Man, and Cybernetics (SMC)*. Vol. 2017-Janua. IEEE, 2017-10, pp. 582–587. isbn: 978-1-5386-1645-1. doi: 10.1109/SMC.2017.8122669. url: http://ieeexplore.ieee.org/document/8122669/.

[114] Z.-B. Wang et al. “Human motion tracking based on complementary Kalman filter”. In: *2017 IEEE 14th International Conference on Wearable and Implantable Body Sensor Networks (BSN)*. IEEE, 2017-05, pp. 55–58. isbn: 978-1-5090-6244-7. doi: 10.1109/BSN.2017.7936006. url: http://ieeexplore.ieee.org/document/7936006/.

[115] C. M. N. Brigante et al. “Towards Miniaturization of a MEMS-Based Wearable Motion Capture System”. In: *IEEE Transactions on Industrial Electronics* 58.8 (2011-08), pp. 3234–3241. issn: 0278-0046. doi: 10.1109/TIE.2011.2148671. url: http://ieeexplore.ieee.org/document/5759076/.

[116] H. Ren and P. Kazanzides. “Investigation of Attitude Tracking Using an Integrated Inertial and Magnetic Navigation System for Hand-Held Surgical Instruments”. In: *IEEE/ASME Transactions on Mechatronics* 17.2 (2012-04), pp. 210–217. issn: 1083-4435. doi: 10.1109/TMECH.2010.2095504. url: http://ieeexplore.ieee.org/document/6988005/%20http://ieeexplore.ieee.org/document/5677500/.

[117] F. Caputo et al. “IMU-Based Motion Capture Wearable System for Ergonomic Assessment in Industrial Environment”. In: *Advances in Intelligent Systems and Computing*. Vol. 795. Springer International Publishing, 2019, pp. 215–225. isbn: 9783319946184. doi: 10.1007/978-3-319-94619-1_21. url: http://dx.doi.org/10.1007/978-3-319-94619-1_21%20http://link.springer.com/10.1007/978-3-319-94619-1_21.

[118] M. Guidolin et al. “On the Accuracy of IMUs for Human Motion Tracking: a Comparative Evaluation”. In: *2021 IEEE International Conference on Mechatronics (ICM)*. IEEE, 2021-03, pp. 1–6. isbn: 978-1-7281-4442-9. doi: 10.1109/ICM46511.2021.9385684. url: https://ieeexplore.ieee.org/document/9385684/.

[119] MBIENTLAB INC. *MMR – MetaMotionR*. url: https://mbientlab.com/store/metamotionr/.

[120] A. Szczsna et al. “Inertial Motion Capture Costume Design Study”. In: *Sensors* 17.3 (2017-03), p. 612. issn: 1424-8220. doi: 10.3390/s17030612. url: http://www.mdpi.com/1424-8220/17/3/612.

[121] Xsens Technologies B.V. *MTi 1-series Datasheet*. Tech. rep. 2019, pp. 1–40.

[122] K. Jedrasiak, K. Daniec, and A. Nawrat. “The low cost micro inertial measurement unit”. In: *2013 IEEE 8th Conference on Industrial Electronics and Applications (ICIEA)*. IEEE, 2013-06, pp. 403–408. isbn: 978-1-4673-6322-8. doi: 10.1109/ICIEA.2013.6566403. url: http://ieeexplore.ieee.org/document/6566403/.

[123] Xsens Technologies B.V. *MVN User Manual*. Tech. rep. April. Xsens, 2021, p. 162. url: https://www.cleancss.com/user-manuals/QIL/MTW2-3A7G6.

[124] Jianliang Zheng and M. Lee. “Will IEEE 802.15.4 make ubiquitous networking a reality?: a discussion on a potential low power, low bit rate standard”. In: *IEEE Communications Magazine* 42.6 (2004-06), pp. 140–146. issn: 0163-6804. doi: 10.1109/MCOM.2004.1304251. url: http://ieeexplore.ieee.org/document/1304251/.

[125] P. G. Luan, N. T. Tan, and N. T. Thinh. “Estimation and Recognition of Motion Segmentation and Pose IMU-Based Human Motion Capture”. In: *Advances in Intelligent Systems and Computing*. Vol. 751. Springer International Publishing, 2019, pp. 383–391. isbn: 9783319784519. doi: 10.1007/978-3-319-78452-6_32. url: http://dx.doi.org/10.1007/978-3-319-78452-6_32%20http://link.springer.com/10.1007/978-3-319-78452-6_32.

[126] S. M. Cerqueira, A. F. D. Silva, and C. P. Santos. “Smart Vest for Real-Time Postural Biofeedback and Ergonomic Risk Assessment”. In: *IEEE Access* 8 (2020), pp. 107583–107592. issn: 2169-3536. doi: 10.1109/ACCESS.2020.3000673. url: https://ieeexplore.ieee.org/document/9113724/.

[127] V. Igelmo et al. “Aiding observational ergonomic evaluation methods using MOCAP systems supported by AI-based posture recognition”. In: *Advances in Transdisciplinary Engineering* 11.September (2020), pp. 419–429. doi: 10.3233/ATDE200050.

[128] F. Wouda et al. “Estimation of Full-Body Poses Using Only Five Inertial Sensors: An Eager or Lazy Learning Approach?” In: *Sensors* 16.12 (2016-12), p. 2138. issn: 1424-8220. doi: 10.3390/s16122138. url: http://www.mdpi.com/1424-8220/16/12/2138.

[129] R. Liu et al. “The Design of Wearable Wireless Inertial Measurement Unit for Body motion Capture System”. In: *2018 IEEE International Conference on Intelligence and Safety for Robotics (ISR)*. IEEE, 2018-08, pp. 557–562. isbn: 978-1-5386-5547-4. doi: 10.1109/IISR.2018.8535742. url: https://ieeexplore.ieee.org/document/8535742/.

[130] Y. Tian et al. “Inertial-based real-time human upper limb tracking using twists and exponential maps in free-living environments”. In: *2017 2nd International Conference on Advanced Robotics and Mechatronics (ICARM)*. Vol. 2018-Janua. IEEE, 2017-08, pp. 552–557. isbn: 978-1-5386-3260-4. doi: 10.1109/ICARM.2017.8273222. url: http://ieeexplore.ieee.org/document/8273222/.

[131] Y.-J. Lu et al. “Accuracy Comparisons in IMU sensor and Motion Analysis Software”. In: *Proceedings of the 2018 2nd International Conference on Mechatronics Systems and Control Engineering - ICMSCE 2018*. Vol. 2018-Febru. 155. New York, New York, USA: ACM Press, 2018, pp. 13–16. isbn: 9781450363792. doi: 10.1145/3185066.3185082. url: http://dl.acm.org/citation.cfm?doid=3185066.3185082.

[132] D. Laidig, P. Müller, and T. Seel. “Automatic anatomical calibration for IMU-based elbow angle measurement in disturbed magnetic fields”. In: *Current Directions in Biomedical Engineering* 3.2 (2017-09), pp. 167–170. issn: 2364-5504. doi: 10.1515/cdbme-2017-0035. url: https://www.degruyter.com/document/doi/10.1515/cdbme-2017-0035/html.

[133] L. Taylor, E. Miller, and K. R. Kaufman. “Static and dynamic validation of inertial measurement units”. In: *Gait Posture* 57.February (2017-09), pp. 80–84. issn: 09666362. doi: 10.1016/j.gaitpost.2017.05.026. url: http://dx.doi.org/10.1016/j.gaitpost.2017.05.026%20https://linkinghub.elsevier.com/retrieve/pii/S0966636217302084.

[134] X. Lai et al. “Design of Motion Capture System Based on MEMS”. In: *2016 IEEE International Conference on Internet of Things (iThings) and IEEE Green Computing and Communications (GreenCom) and IEEE Cyber, Physical and Social Computing (CPSCom) and IEEE Smart Data (SmartData)*. IEEE, 2016-12, pp. 604–608. isbn: 978-1-5090-5880-8. doi: 10.1109/iThings-GreenCom-CPSCom-SmartData.2016.134. url: https://ieeexplore.ieee.org/document/7917162/.

[135] M. Delrobaei et al. “Characterization of multi-joint upper limb movements in a single task to assess bradykinesia”. In: *Journal of the Neurological Sciences* 368 (2016-09), pp. 337–342. issn: 0022510X. doi: 10.1016/j.jns.2016.07.056. url: http://dx.doi.org/10.1016/j.jns.2016.07.056%20https://linkinghub.elsevier.com/retrieve/pii/S0022510X16304695.

[136] S. Lim, A. Case, and C. D'Souza. "Comparative Analysis of Inertial Sensor to Optical Motion Capture System Performance in Push-Pull Exertion Postures". In: *Proceedings of the Human Factors and Ergonomics Society Annual Meeting* 60.1 (2016-09), pp. 970–974. issn: 2169-5067. doi: 10.1177/1541931213601224. url: http://journals.sagepub.com/doi/10.1177/1541931213601224.

[137] A. G. Cutti et al. "Ambulatory measurement of shoulder and elbow kinematics through inertial and magnetic sensors". In: *Medical Biological Engineering Computing* 46.2 (2008-02), pp. 169–178. issn: 0140-0118. doi: 10.1007/s11517-007-0296-5. url: http://link.springer.com/10.1007/s11517-007-0296-5.

[138] W. de Vries et al. "Functionally interpretable local coordinate systems for the upper extremity using inertial magnetic measurement systems". In: *Journal of Biomechanics* 43.10 (2010-07), pp. 1983–1988. issn: 00219290. doi: 10.1016/j.jbiomech.2010.03.007. url: http://dx.doi.org/10.1016/j.jbiomech.2010.03.007%20https://linkinghub.elsevier.com/retrieve/pii/S002192901000151X.

[139] L. Fradet et al. "Which functional movements for sensor-to-segment calibration for lower-limb movement analysis with inertial sensors?" In: *Computer Methods in Biomechanics and Biomedical Engineering* 20.sup1 (2017-10), S77–S78. issn: 1025-5842. doi: 10.1080/10255842.2017.1382869. url: https://doi.org/10.1080/10255842.2017.1382869%20https://www.tandfonline.com/doi/full/10.1080/10255842.2017.1382869.

[140] ISO. *ISO 9241-210:2019 Ergonomics of human-system interaction — Part 210: Human-centred design for interactive systems*. Tech. rep. 2019, p. 33.

[141] J. Nielsen. *Usability Engineering*. 1st ed. Burlington, MA, USA: Elsevier, 1993, p. 362. isbn: 9780125184069. doi: 10.1016/C2009-0-21512-1. arXiv: arXiv:1011.1669v3. url: http://www.elsevier.com/locate/scp%20https://linkinghub.elsevier.com/retrieve/pii/C20090215121.

[142] Q. Wang et al. "Interactive wearable systems for upper body rehabilitation: a systematic review". In: *Journal of NeuroEngineering and Rehabilitation* 14.1 (2017-12), p. 20. issn: 1743-0003. doi: 10.1186/s12984-017-0229-y. url: http://jneuroengrehab.biomedcentral.com/articles/10.1186/s12984-017-0229-y.

[143] F. Gemperle et al. "Design for wearability". In: *Digest of Papers. Second International Symposium on Wearable Computers (Cat. No.98EX215)*. Vol. 1998-Octob. November 1998. IEEE Comput. Soc, 1998, pp. 116–122. isbn: 0-8186-9074-7. doi: 10.1109/ISWC.1998.729537. url: http://ieeexplore.ieee.org/document/729537/.

[144] J. Knight et al. “Assessing the Wearability of Wearable Computers”. In: *2006 10th IEEE International Symposium on Wearable Computers*. January 2015. IEEE, 2006-10, pp. 75–82. isbn: 1-4244-0597-1. doi: 10.1109/ISWC.2006.286347. url: http://ieeexplore.ieee.org/document/4067730/.

[145] STMicroelectronics N.V. *Lsm6Dsox Datasheet*. Tech. rep. January. 2019, pp. 1–199.

[146] STMicroelectronics N.V. *LIS3MDL Datasheet*. Tech. rep. May. 2017, pp. 1–33. url: www.st.com.

[147] TDK Invensense. *MPU-9250 Product Specification*. Tech. rep. 2016, pp. 1–42.

[148] AsahiKasei. *AK 8963 3-axis Electronic Compass Datasheet*. Tech. rep. 2013, pp. 1–38.

[149] Precision Microdrives ™. “Product Data Sheet Model No. 310-122”. In: (), pp. 1–6.

[150] STMicroelectronics N.V. “Arm® Cortex®-M7 32-bit 550 MHz MCU, up to 1 MB Flash, 564 KB RAM, Ethernet, USB, 3x FD-CAN, Graphics, 2x 16-bit ADCs”. In: December (2021), p. 234.

[151] STMicroelectronics N.V. “STM32H7 Nucleo-144 boards (MB1364)”. In: June (2020), pp. 1–50.

[152] Raspberry Pi. *Raspberry Pi Documentation*. url: https://www.raspberrypi.com/documentation/computers/raspberry-pi.html.

[153] Microchip. *ATWINC15x0 Datasheet*. Tech. rep. 2021, pp. 1–58.

[154] ON Semiconductor. *AN-5083: FIS1100 AttitudeEngine™ Low Power Motion Co- Processor for High Accuracy Tracking Applications*. Tech. rep. 2015, p. 11.

[155] STMicroelectronics N.V. *STM32H723/733, STM32H725/735 and STM32H730 Value line advanced Arm®-based 32-bit MCUs*. Tech. rep. December. 2021, pp. 1–3357.

[156] D. Gebre-Egziabher et al. “A non-linear, two-step estimation algorithm for calibrating solid-state strapdown magnetometers.” In: *8th International Conference on Integrated Navigation Systems* (2001), pp. 290–297. url: http://gps.stanford.edu/papers/demozins201.pdf.

[157] Adafruit. *Calibration and Programming*. url: https://learn.adafruit.com/adafruit-analog-accelerometer-breakouts/calibration-and-programming.

[158] Portuguese Institute for Sea and Atmosphere. *Geomagnetism*. 2022. url: https://www.ipma.pt/en/enciclopedia/geofisica/geomagnetismo/index.html.